

Università degli Studi di Bologna

---

---

FACOLTÀ DI SCIENZE MATEMATICHE FISICHE E NATURALI

Dottorato di Ricerca in Fisica

Settore scientifico disciplinare: Fisica Nucleare e Subnucleare (FIS/04)

(XIX ciclo)

CARBON NANOTUBES  
AND  
NANOPOROUS ALUMINA  
IN THE DEVELOPMENT OF A HIGH  
RESOLUTION POSITION DETECTOR

Tesi di Dottorato  
di  
Giulio Paolo Veronese

Coordinatore:

**Prof. Fabio Ortolani**

Tutore:

**Prof. Antonio Maria Rossi**

Correlatori:

**Prof. Marco Cuffiani**

**Dott. Rita Rizzoli**

Bologna, Marzo 2007



# Contents

|  |            |
|--|------------|
| <b>INTRODUCTION</b>  | <b>3</b>   |
| <b>CHAPTER 1 THE NANOCHANT PROJECT</b>                             | <b>7</b>   |
| 1.1 POSITION PARTICLE DETECTORS                                    | 7          |
| 1.1.1 <i>Energy loss mechanisms</i>                                | 8          |
| 1.1.2 <i>Tracking silicon detectors</i>                            | 14         |
| 1.2 THE NANOCHANT PROJECT  | 18         |
| <b>CHAPTER 2 NANOTECHNOLOGIES INVOLVED IN THE PROJECT</b>          | <b>25</b>  |
| 2.1 CARBON NANOTUBES   | 26         |
| 2.1.1 <i>Structures and properties</i>                             | 27         |
| 2.1.2 <i>Synthesis of carbon nanotubes</i>                         | 32         |
| 2.1.3 <i>Field emission from carbon nanotubes</i>                  | 38         |
| 2.2 ANODIC ALUMINIUM OXIDE   | 45         |
| 2.2.1 <i>General properties</i>                                    | 45         |
| 2.2.2 <i>Porous growth</i>   | 47         |
| 2.2.3 <i>Process parameters</i>                                    | 51         |
| 2.2.4 <i>Templated synthesis of nanowires</i>                      | 55         |
| <b>CHAPTER 3 SYNTHESIS OF FREE STANDING CARBON NANOTUBES</b>       | <b>57</b>  |
| 3.1 DEPOSITION SYSTEM AND CHARACTERIZATION FACILITIES              | 58         |
| 3.1.1 <i>Chemical Vapour Deposition system</i>                     | 58         |
| 3.1.2 <i>Characterization facilities</i>                           | 60         |
| 3.2 SYNTHESIS ON INSULATING SUBSTRATES                             | 64         |
| 3.3 SYNTHESIS ON CONDUCTIVE SUBSTRATES                             | 82         |
| 3.4 FIELD EMISSION CHARACTERIZATION                                | 89         |
| 3.4.1 <i>Field emission system</i>                                 | 89         |
| 3.4.2 <i>Field emission measurements</i>                           | 91         |
| <b>CHAPTER 4 TEMPLATED SYNTHESIS OF CARBON NANOTUBES</b>           | <b>105</b> |
| 4.1 ANODIC ALUMINIUM OXIDE   | 105        |
| 4.1.1 <i>Experimental setups</i>                                   | 105        |
| 4.1.2 <i>Syntheses and characterizations</i>                       | 107        |
| 4.1.3 <i>Catalyst seeds deposition</i>                             | 121        |
| 4.2 CARBON NANOTUBES SYNTHESIS IN ANODIC ALUMINIUM OXIDE TEMPLATES | 123        |
| <b>CONCLUSIONS</b>   | <b>137</b> |
| <b>BIBLIOGRAPHY</b>  | <b>141</b> |



## Introduction

Position particle detectors with high spatial resolution are fundamental in many scientific fields. Tracking and particle identification are essential in High Energy Physics and Astrophysics experiments, but high resolutions are also required by medical imaging applications and commercial digital video cameras.

The NanoChanT (“Nano Channel Template”) project proposes to develop a nanotechnology based radiation detector, able to improve the present limit in the spatial resolution of the silicon detectors (microstrip, CCDs and APSs detectors). The novel type of device is envisaged to exploit nanotechnologies at the frontier of knowledge, specifically for the realization of large-area nanostructures. This is very challenging since it involves many nanotechnological steps that must be compatible with the silicon technology. The final goal is to build a prototypal radiation detector with submicron spatial resolution.

The basic idea of the detector is to use a thin silicon diode as the sensing layer of the device. Reducing the thickness, with respect to the current silicon detectors, limits the effects that degrade the spatial resolution, namely the spreading of the charges produced by the incident radiation and the probability of high energy secondary electrons, which can push off the centroid of the produced charge. The silicon active layer is segmented into a regular array of submicrometric pixels, while the signal charges are brought to the read-out electronics through nanometric charge collectors, in order to preserve the spatial resolution.

As nanometric charge collectors, Carbon Nanotubes (CNTs) have been produced. They are obtained within an insulating template of nanoporous Anodic Aluminium Oxide (AAO), made of a highly regular array of vertically aligned nanochannels. In order to achieve a high signal-to-noise ratio, the electrical interface between CNTs and the silicon layer, which is a key-point of the design, is deeply studied.

The research work of this thesis focussed on two main topics: the synthesis of a highly regular nanochannels template of Anodic Aluminium Oxide (AAO) and the synthesis of Carbon Nanotubes (CNTs). The growth of CNTs has been investigated both in a free standing and in a confined configuration. The confined synthesis has been studied aiming at a uniform growth of CNTs inside the nanopores of the AAO template.

In order to examine the electrical interface between CNTs and a silicon substrate, a field emission characterization of the CNTs-silicon system has been performed on the free standing CNTs configuration. The field emission behaviour of CNTs is interesting in itself, since devices based on this phenomenon can be employed as cold electron sources. For instance, such structures are investigated as electron sources for electron cyclotron resonance ion sources to be used as injectors into linear accelerators, Van de Graaff generators or cyclotrons in nuclear and elementary particle physics.

The thesis is organized as follows:

- In Chapter 1 the basics of radiation detection in silicon devices and, in particular, the limitations to the spatial resolution are discussed. A detector with a thin active layer would improve the spatial resolution. This approach has been adopted in the design of the NanoChanT detector, whose basic idea is described.
- In Chapter 2 the nanotechnologies involved in the fabrication of the NanoChanT detector are reviewed. The synthesis methods and the structural properties of both CNTs and nanoporous AAO are described. The electrical properties of CNTs, and in particular their field emission characteristics, are discussed.
- In Chapter 3 the growth of free standing CNTs by means of the Catalyst-assisted Chemical Vapour Deposition (C-CVD) method is investigated, both on insulating and conductive substrates. The optimization of the CNT quality is studied by varying the parameters of the C-CVD process. The proper interface between CNTs and the silicon, as used in the final design of the detector, is studied by means of field emission characterization of the CNTs.
- In Chapter 4 both the fabrication of the nanoporous AAO and the synthesis of confined CNTs within alumina nanopores are studied. The C-CVD process is investigated aiming at a highly uniform filling of the template nanopores with CNTs and at the optimization of their structural quality.

The work has been developed within a collaboration among the Department of Physics of the University of Bologna, the INFN (Istituto Nazionale di Fisica Nucleare) Institute, Section of Bologna, and the IMM (Istituto per la Microelettronica e i Microsistemi) Institute of CNR (Consiglio Nazionale delle Ricerche), Section of Bologna.



# Chapter 1     The NanoChanT Project

## 1.1     Position particle detectors

The general working principle is common to all the different kind of position particle detectors. The incident radiation interacts with the active part of the detector, involving an energy transfer. This energy has thus to be revealed by the read-out electronics of the detector. The energy deposit can be located within a specific volume of the detector by segmenting the geometry and the read-out electronics of the device, allowing to determine the position of the impinging particle with a spatial resolution that scales with the segmentation density.

Up to now, silicon is the preferred material for high precision tracking detectors. Different reasons support this choice. Firstly, a vast IC technology has been developed for silicon, mainly boosted by the mass market industry, with billions of dollars annually invested. It is possible to grow high quality crystal of silicon, to perform n- and p-type doping, to selectively grow highly insulating layers ( $\text{SiO}_2$  and  $\text{Si}_3\text{N}_4$ ). Moreover, all these processes can be performed using micro-lithographic techniques, allowing feature sizes below  $1 \mu\text{m}$ . Secondly, a condensed medium is essential if point measurements precision below  $10 \mu\text{m}$  is required. Gaseous tracking detectors are limited by diffusive spreading of the released electron cloud to precision of typically some tens of microns. The problems related to liquid detectors stay in the difficulty in maintaining purity in their composition. On the contrary, condensed media of high purity level can be exposed to the atmosphere and assembled in complex geometries with no degradation of their bulk electron lifetime characteristics.

Among the other solid state detection media, silicon has a band gap (1.1 eV) low enough to ensure copious production of free charge from a minimum-ionizing particle, about 80 electron-hole pairs per micron of track length, but high enough to avoid very large leakage current generation at room temperature ( $kT = 26 \text{ meV}$ ). Moreover, having a low atomic number ( $Z = 14$ ) it is less exposed to multiple scattering. The energy loss processes in a silicon medium allow in principle a precision (much better than  $1 \mu\text{m}$ ) that is

definitely better even with respect to the one achievable in a nuclear emulsion (which typically requires a 400 eV single electron to blacken a grain).

The active layer of a silicon detector consists of a depleted p-n junction. Indeed, intrinsic silicon would have a too low resistivity, i.e. a too large amount of free charges, except at extremely low temperatures. This would bring to a large leakage current, due to thermal or optical excitation, which in detectors leads to a high signal noise.

Applying a reversal polarization at a diode, it is possible to generate a region depleted of free charge carriers, both electrons and holes, thus reducing the leakage current. An internal electrical field exists also in this region induced by the fixed ions of the silicon lattice. Electron-hole pairs generated inside depleted region are promptly swept to the surface where they are collected [1].

### *1.1.1 Energy loss mechanisms*

In High Energy Physics, the measurement of the ionization by charged particles in a medium is fundamental since, together with the measurement of their momentum or energy, it allows particles identification and tracking. The understanding of the energy loss mechanisms of a radiation inside a medium is thus essential and it has been deeply investigated. A brief description of the basic principles is given here restricted to the silicon medium case. More detailed reviews can be found in the literature [2].

While traversing a crystalline silicon layer, high-energy charged particles lose energy by means of two main mechanisms. The first and principal one is the ionization of atomic electrons. The second one (the so-called non-ionizing energy loss or NIEL) consists of displacement of silicon atoms from the crystal lattice, mostly by the process of Coulomb nuclear scattering. This latter phenomenon is active only if the energy transfer to the nucleus exceeds approximately 25 eV. For instance, for an incident electrons radiation, the effective threshold energy for displacement damage is around 250 keV. Below that, the energy is dissipated by harmless lattice vibrations, causing thermal heating. Displacement of silicon atoms to interstitial positions, and the consequent creation of a vacancy in the lattice, is one of the main radiation damage mechanisms. For a high-energy particle, the fraction of energy loss involved in the NIEL mechanism is relatively small, but the cumulative effects on the detector performance can be severe.

Ionization of atomic electrons by means of an incident radiation mainly occurs by means of Coulomb scattering collisions. The ionization energy loss and the number of ionizing collisions per unit path length can be evaluated from the differential cross-section  $\frac{d\sigma}{dE}$  that is related to the energy of the incident radiation and to the properties of the detector medium. Generally, distant collisions, which involve small energy transfer, are the most probable, whereas close collisions are quite rare but result in large energy transfers.

The greater probability of the former collisions arises from the greater volume of material available for collisions with a given impact parameter range.

The simplest treatment of this Coulomb interaction is described by Rutherford cross-section, which defines the probability of collision imparting an energy  $E$  to unbound atomic electrons [3]. That is,

$$\frac{d\sigma_R}{dE} = \frac{2\pi q_e^4}{m_e c^2 \beta^2 E^2} \quad (1.1)$$

where  $m_e$  and  $q_e$  are the mass and the charge of the electrons, respectively. The same formula holds also for the interaction between the radiation and the silicon nuclei. Being the mass of the medium atoms at the denominator, the energy loss due to these interactions can be neglected. On the contrary, these particle–silicon nuclei collisions determine an angular deviation of the incident particle trajectory, by means of multiple nuclear Coulomb scattering. Also, for sufficiently large momentum transfers, these collisions contribute to the NIEL mechanism.

In a first simplified approach, the energy loss of a radiation in a given thickness detector, can be determined by integrating over all energies the Rutherford formula, taking into account some cautions. In fact, the integral can not be from 0 to infinite, but some cut-offs have to be imposed (also for keeping the integral convergent). An upper limit is set by the maximum transferable energy in a collision process by the relativistic kinematics. If the mass of the incident radiation particle is much greater than the electron one, then  $E_{MAX} = 2m_e c^2 \beta^2 \gamma^2$ . The lower limit is imposed by the fact that electrons are bound in atoms, and thus they require a minimum energy to be freed. A semi-empirical cut-off  $E_{MIN}$ , which depends on the atomic number  $Z$  of the material, is then established. The Rutherford formula is especially useful as regards the close collisions, which are important in defining the fluctuations in energy loss in thick samples, where “thick” means approximately thicker than 50  $\mu\text{m}$  of silicon. In fact, for these high energy collisions, all atomic electrons can be considered as free and the above approximations hold.

Another mechanism is associated at these close collisions, when energy transfers approximately above 10 keV are involved. They generate high energy secondary electrons of significant range, named  $\delta$ -electrons. These high energy electrons are particularly important in tracking detector because they may have a degradation effect on the precision, being themselves able to induce a further ionization, locally on the track of the incident radiation, or distributed, in the case of significant  $\delta$ -electron range.

Keeping into account the effect of the Poisson statistics on energy transfers in the energy range where the Rutherford cross-section is significantly different from zero, the final form of the energy loss distribution, or straggling distribution, results to be described by the Landau distribution. This consists of an approximately Gaussian core and a high

tail, populated by the large energy transfer events in which a few close collisions occurred. In silicon, the energy loss for more than 90 % of all collisions is below 200 eV, almost independent on the  $\beta\gamma$  value of the incident radiation.

Since the ultimate products of the ionization are electrons promoted into the conduction band of the material and vacancies in the valence band (or holes), the energy loss can be also described by means of the energy required for the generation of each electron-hole pair. The mean value for such creation, named ionization rate, is approximately 3.6 eV. Since the silicon band gap is around 1.1 eV, it results that about two thirds of the energy transferred from the primary electrons give rise to phonon generation, eventually appearing as heating in the detector.

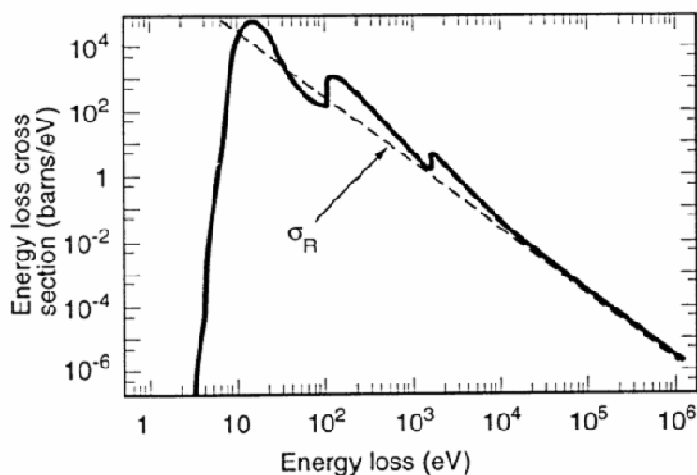


**Figure 1.1.** Energy loss cross-section for minimum ionizing particles in silicon versus energy loss in primary collision. Rutherford cross-section  $\sigma_R$  is also plotted [5].

The previous discussion on the energy loss cross-section holds for thick silicon layers, but it is no more valid for thin silicon samples. Indeed, in the latter the main contribution at the energy loss arises from low energy transfer collisions. In this energy range, the binding energy of the atomic electrons has to be considered in detail and the actual energy loss cross-section has to be modified.

More detailed theoretical models with respect to the Rutherford approach have been traced using the Fermi virtual photon (FVP) and the Bethe-Fano (B-F) methods. A precise determination of the minimum ionizing particle energy loss cross-section for silicon has been experimentally obtained by means of combining photo-adsorption and EELS (electron energy loss spectroscopy) data [4]. A detail presentation of these methods can be found in [2]. Qualitatively, it turns out that resonance-like enhancements in the energy loss cross-section are generated. Three peaks arise at energies of about 17, 150 and 1840 eV,

corresponding at the M-, L- and K-shells of silicon. The related energy loss cross-section for a minimum ionizing particle ( $\beta\gamma = 5$ ) is shown in Figure 1.1. It exceeds the Rutherford cross-section in the range 10 eV – 5 keV. Above 10 keV the difference is quite small.

The larger effect is related to the M-shell electrons, which produces electron-hole pairs. These electrons behave as a dense electron plasma embedded in a fixed positive charge distribution. The real or virtual photons couple to this plasma by generating longitudinal density oscillations, whose quantum is called a plasmon, and has a mean energy of 17 eV. These plasmons de-excite almost entirely by electron-hole pair creation, enhancing the cross-section in the UV region.

By integrating the different components of the cross-section, the total mean collision rate is determined to be 3.8 collisions per micron, being mainly due to interaction with M-shell electrons, about 3.2, and then L-shell, 0.63. The probability per micron of interactions with the K-shell electron is quite lower ( $8.8 \cdot 10^{-3}$ ).

In conclusion, although on average a 1  $\mu\text{m}$  thick silicon layer yields 80 electron-hole pairs, the Poisson statistics on the primary process (3.8 collisions per micron) implies a broad distribution and, in particular, a not-negligible probability of zero collisions, which means no signal at all. It is thus clear that the energy loss fluctuations associated with the primary process variability can not be properly modelled by the Landau distribution, since their shapes are strongly dependent on the sample thickness.

Despite these considerations, for tracking detector, it is clear that keeping the active layer of the silicon detector as thin as possible results in highly enhancing the precision. Firstly, the multiple scattering would be limited. Moreover, a minimum thickness should be optimal as regards point measurement precision, for two reasons.

The first one involves tracks incident normally to the active layer. The concern arises because  $\delta$ -electrons pull the centroid of the charge deposited significantly off the track. Figure 1.2 depicts an integral distribution of the number of primary electrons per micron of energy above a certain value (a) and the range of electrons of the corresponding energy in silicon (b). The range becomes significant for high precision tracking detectors for energies above 10 keV, for which the generation probability is less than 0.1 % per micron. For energies above 100 keV the range becomes comparable with typical detectors thickness of few hundreds microns. Consequently, the thinner is the detector thickness, the smaller is the probability of obtaining a shifted coordinate. If the detector allows the measurement of the released energy, some of these bad coordinates can be identified by abnormally large associated energy. Imposing a cut on the energy deposit, it generally results in unacceptable inefficiency and thus it is rarely implemented. Figure 1.3 summarizes the situation, depicting the probability of the charge centroid associated with a track being pulled by more than a given value as a function of a detector thickness.

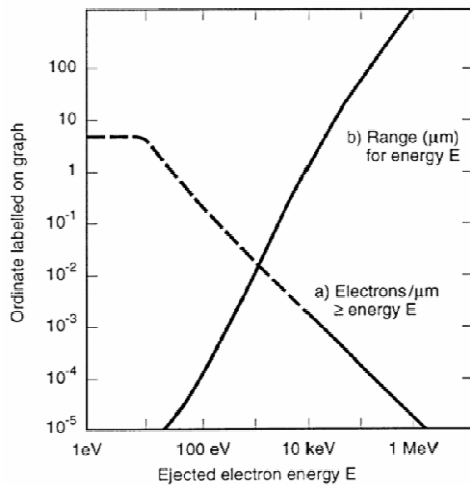


**Figure 1.2.** The number of electrons per micron of MIP track above a given energy (a), and the range in silicon corresponding to the same energy (b) are shown as a function of the ejected electron energy [5].

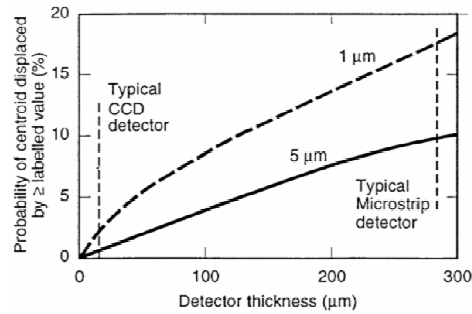


**Figure 1.3.** The limits of the detector precision due to  $\delta$ -electrons for normal incident tracks, as function of detector thickness [5].

The second reason for preferring thinner detectors concerns angled tracks. The normally adopted approach to determine the position of the track traversing is to measure the centroid of the elongated charge distribution and to assign this position at the active layer mid-plane. In this case, large fluctuations in the energy loss (due to ejection of K- and L-shell electrons and especially of  $\delta$ -electrons) may be sufficient to seriously bias the centroid (Figure 1.4). Again in a thin detector, the smaller probability of generation of high energy primary electrons limits this bias.

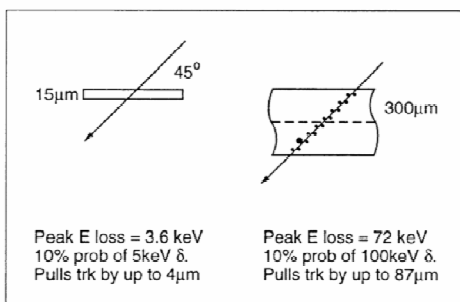


**Figure 1.4.** Effect of energy loss fluctuations on detector precision for angled tracks [5].

Naturally, the thickness of the active layer can not be reduced indefinitely. A minimum thickness exists determined by the achievement of a sufficiently high efficiency per layer. For very thin silicon detectors the distribution of the probability of losing an energy  $E$  is completely different from the theoretical Landau distribution. As already discussed, this can be expected in thin detectors, because the shape of the energy loss spectra, or straggling functions, are dominated by the Poisson distribution of the small number of collisions. The actual energy loss distribution turns out to be strongly affected

by plasmons excitations. Even at 10  $\mu\text{m}$  silicon thickness the true distribution is much broader than the Landau and has a dangerous low tail (Figure 1.5).

Consequently, to fully exploit the superior possibilities in tracking precision provided by thin detectors, it is necessary to achieve a sufficiently low threshold energy level and hence the detector has to assure a low system noise.

Another factor that can affect the resolution limit of the detector is related to the diffusive spreading of the charges created by the ionizing radiation. While the charges are driven by the internal field in the detector towards the electrode, the process of diffusion spreads out the original charge cloud, which diffuses radially. The RMS radius of the charge distribution increases with time  $t_D$ , with standard deviation  $\sigma = \sqrt{2Dt_D}$ . Thus, half of the total charge is contained within a radius of  $0.95\sqrt{Dt_D}$ . For a typical 1 kV/cm drift field in depleted silicon, if the drift time is 10 ns the drift distance will be 135  $\mu\text{m}$  and the charge radius 6  $\mu\text{m}$ . This diffusive spreading can be used to improve spatial precision beyond the limit of the detector granularity by finding the centroid of the charge collected in the different elements. An analogic read-out electronic is then required. On the contrary, if a binary logic read-out electronic is used, i.e. only the information whether the channel has been hit or missed is stored, the charge spreading can contribute to reduce the detector spatial precision.

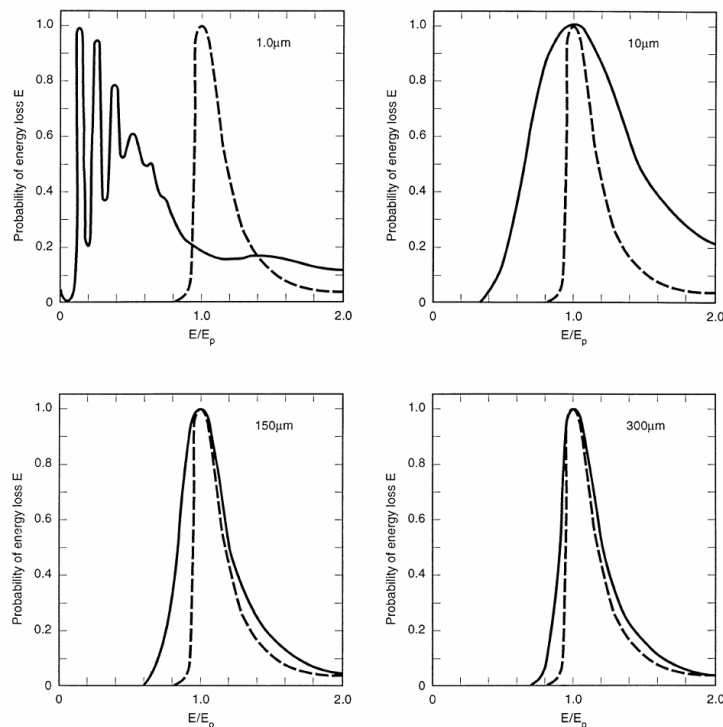


**Figure 1.5.** Energy loss distributions for various silicon detector thicknesses. A Landau distribution is reported on each graph for comparison. The peaks corresponding to plasmon excitation merge for thicknesses larger than 10  $\mu\text{m}$  [6].

1.1.2 Tracking silicon detectors

Tracking silicon detectors can assume different configurations. Microstrip and pixel segmentations are the most commonly employed arrangements in High Energy Physics detectors until now. New structures have been proposed in the last years, but are still in development.

Microstrip detectors have essentially a  $p^+n-n^+$  structure. They are generally composed by an n-type substrate, 300  $\mu\text{m}$  thick, with high resistivity (3 – 5  $\text{k}\Omega\cdot\text{cm}$ ) and of some  $\text{cm}^2$  size. On one side,  $p^+$ -strips are implanted with aluminium back contact to provide low resistance path and connected to read-out electronics. On the other side, an  $n^+$  layer is implanted (Figure 1.6). Commonly also this layer is segmented in strips, perpendicular to the  $p^+$  ones. In this way, a double-sided microstrip detector can be obtained, which provides two coordinates of the track. The diode is depleted by applying a positive voltage to the  $n^+$  strips and grounding the  $p^+$  ones. Depletion voltages between 50 and 150 V are commonly used.

Both AC and DC coupled microstrip detectors can be realized. In the former configuration the metal read-out strips are isolated from the implanted strips by a thin dioxide layer. The amplifier inputs sense the fast signal without being affected by the DC leakage current, which can degrade in applications where radiation levels are high. When this is not the case, the DC coupling is surely simpler. The strips widths are between 5 and 200  $\mu\text{m}$ , and are isolated from each other by a thin layer of silicon dioxide. These layers of silicon dioxide inevitably collect positive charges which are compensated by a thin accumulation layer of mobile electrons in the bulk material. On the  $n^+$  side, they create a low resistance inter-strip leakage path, causing shorts between the strips. For this reason  $p^+$  strips are implanted between the  $n^+$  strips and biased negatively relative to these. The final result is that a negatively charged depletion layer is created which blocks the leakage path.

The spatial precision in microstrip detector is constrained by the read-out pitch of all the existing front-end electronics, namely 50  $\mu\text{m}$ . A reduction of a factor of two can be achieved by attaching read-out ICs at each end of a module. Spatial resolution of approximately  $\frac{25}{\sqrt{12}} \mu\text{m} = 7.2 \mu\text{m}$  is thus a common value for microstrip detector when read out with standard electronics is used.

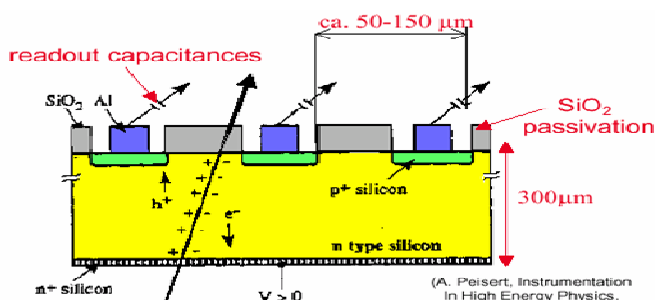


Figure 1.6. Scheme of a microstrip detector.

For a typical arrangement in a double-side detector, a read-out of every strip on a pitch of  $50\ \mu\text{m}$  has been reported to allow a measured maximum precision, for a normal incident track, of  $8.8\ \mu\text{m}$ . If not all the strips are read and a charge centroid calculation is used, the precision limit can be enhanced further on. For normal incident tracks, the spatial precision may be considered typical in the range  $5 - 10\ \mu\text{m}$  for strip pitch less than  $50\ \mu\text{m}$  and read-out pitch less than  $150\ \mu\text{m}$ . For angled tracks the precision deteriorates rapidly [5].

It has to be noted that because of their thickness, microstrip detectors are particularly affected by  $\delta$ -electrons, which, as already discussed, can cause a loss of precision. A cut-off on the maximum energy is usually imposed to exclude these events, but this is a big disadvantage, especially for tracking detector with a limited number of points per track. Thinner detectors are not commonly used since the loss of signal charge, enhanced by the reduction in the voltage signal due to the increased capacitance from strip to substrate, results in a poor signal-to-noise performance.

The other segmentation scheme that has been implemented is the one related with pixel-based detectors. The most common ones are the charge-coupled devices (CCDs) (Figure 1.7) [6]. They have experienced a large development mainly because pushed by commercial applications such as high definition cameras.

In this configuration a square matrix of potential wells is produced by creating a MOS structure, where the semiconductor part consists of a reverse diode. The final arrangement results to be Metal – Oxide – n-type silicon – p-type silicon.

The pixel matrix is created by two perpendicular structures. In one direction,  $p^+$  strips are implanted on the n-type silicon and are depleted in order to act as stop channels for the ionization charge. These strips can have a pitch of  $20\ \mu\text{m}$ , which determines the pixel granularity. In the other direction, a conductive poly-silicon gate structure, consisting in a series of parallel bars, is made.

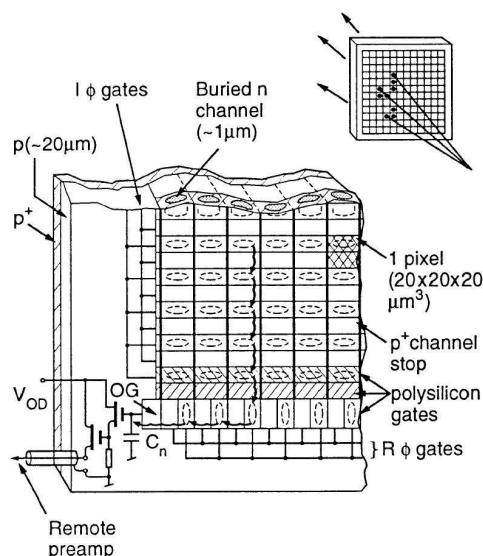


**Figure 1.7.** Scheme of a CCD detector. On the upper right corner the principle of charge storage in a CCD detector traversed by ionizing particles. On the left, the corner region of CCD [6].

In scientific applications the “buried channel” architecture is generally adopted. It involves the creation in the n-channel of a “buried channel”, correspondent to a minimum potential energy for electrons. This potential shape is achieved by means of two contributions. The first comes from the reversal polarization of the diode. The second contribution arises from a negative polarization applied between the gate voltage and the n-channel, which brings to an increasing positive space-charge in the silicon. Both the effects result in a depletion of the n-channel, the former starting from the p–n interface and the latter from the silicon–silicon dioxide one. These depletion regions meet and a minimum potential energy for electrons is created below the surface, distant from the interface states that can trap the signal charge. Generally, this buried channel is placed at 1  $\mu\text{m}$  depth. The ionization produced by an incident radiation is thus collected in this channel. Since the trapping sites are avoided, tiny charge can be safely stored and transported along the silicon bulk. To measure the charge accumulated in the pixels, an arrangement of the gates in triplets (3-phase structure) is required in order to shift the collected charge in parallel from a row to the next. The pixel width results from the sum of the three gates pitch. For a typical pitch value of 7  $\mu\text{m}$ , the pixel width turns out to be  $3 \times 7 \mu\text{m} = 21 \mu\text{m}$ . At the bottom row, the charge is transferred into an output node consisting of a sensing amplifier that sequentially reads each pixel charge. The 2-D pattern is thus converted in a serial train of impulses.

A CCDs detector has many advantages in tracking devices. First of all, the 2-D point measurement allows reducing the number of possible combination in the reconstruction of the tracks with respect to the 1-D microstrip detector. The high granularity is also enhanced, and hence a higher tolerability in the hit element density can be achieved. Further, most of the forms of pixel-based detectors show a third advantage. They have extremely low capacitance nodes for charge collection, and thus a smaller signal is sufficient for achieving a satisfactory signal-to-noise ratio. This allows a thickness reduction with respect to microstrip configuration, down to approximately 15  $\mu\text{m}$ . The measured precision for a minimum ionizing particle under typical readout conditions (RMS noise approximately of 50  $e^-$ ) is about 3.5  $\mu\text{m}$ , even if values down to 0.9  $\mu\text{m}$  have been reported [5]. CCDs detectors have also some drawbacks, which make them impractical in some situations. In particular they have a slow read-out, and thus a long dead time results associated. Furthermore, they are particularly exposed to radiation damages, and hence they can not be employed, as in hadron colliders, or have to be exchanged frequently.

A new configuration for pixel-based detectors has been proposed in the active pixel sensors (APSs) detectors. The charge collection is, as usual, to one electrode of a reverse biased diode, but in APSs these diodes form a physically fixed matrix over the device area and each one is connected to its own signal processing circuits within the pixel. This structure has been approached by means of two solutions. The first is a hybrid approach,

which involves the bonding of a single sided microstrip detector, with the strips cut into pads, and a CMOS readout chip. The second one plans to work on a single monolith. The advantages of APSs are a high speed gating, the possibility to transfer the hit information into a pipeline memory and an enhanced radiation hardness.

As already stated, silicon pixel and microstrip detectors are widely used in the currently working High Energy Physics experiments. For instance, the CMS experiment at the Large Hadron Collider (LHC) of Geneva employs a tracker system formed of three main sub-detectors, two of which are based on silicon vertex detector, the third being a microstrip gas sensor [7]. A pixel detector system is placed in the innermost region. Pixels are 250  $\mu\text{m}$  thick and have a size of  $150 \times 150 \mu\text{m}^2$ . Without charge sharing, this allows a spatial resolution of 45  $\mu\text{m}$ . The actual configuration of the pixels and an analogue read-out system permits to calculate the charge centroid and to improve the precision up to 10 – 20  $\mu\text{m}$ , depending on the geometrical allocation in the detector. A second shell consists of a silicon microstrip detector. AC-coupled single-side  $p^+$  strips have been used, with a thickness of 300  $\mu\text{m}$  and the pitch between 60  $\mu\text{m}$  and 270  $\mu\text{m}$ . The maximum spatial resolution achievable is about 15  $\mu\text{m}$ . It has to be noted that these precisions also depend on configuration requirements for sustaining a high radiation environment.

The same choice of silicon pixel and microstrip detectors has been made for the ATLAS experiment, with also similar spatial precisions [8]. The track detector system of the Babar detector at SLAC PEP-II experiment is based on a silicon vertex tracker and a drift chamber. The former detector is placed in the innermost shell, because it allows the most precise track reconstruction, and it consists of double-sides silicon  $p^+$  strips 300  $\mu\text{m}$  thick. The related spatial resolution achieves a limit of 10 – 15  $\mu\text{m}$  [9]. Also space experiments, such as AMS, employ 300  $\mu\text{m}$  thick silicon microstrip detectors for high resolution tracking, achieving a 10  $\mu\text{m}$  spatial resolution [10].

Also other applications, different from High Energy Physics ones, employ silicon based detectors. For instance, high precision medical imaging utilizes silicon microstrip detectors for achieving high resolutions [11].

### 1.2 The NanoChanT project

In 2001, the NanoChanT project has proposed to develop a novel type of position particle detector, based on nanotechnologies, which achieves a submicron spatial resolution.

The NanoChanT (“Nano Channel Template”) project is an INFN (Istituto Nazionale di Fisica Nucleare) project, which has been accepted in the INFN Group V section, which is devoted to the development of new technologies, application devices and software. It involves the collaboration of different partners, namely the INFN, Section of Bologna, the Department of Physics of the University of Bologna and the IMM (Istituto di Microelettronica e Microsistemi), Section of Bologna, of the CNR Institute (Consiglio Nazionale delle Ricerche).

The basic idea of the NanoChanT detector consists of integrating the well known silicon IC technology with some innovative nanotechnologies in order to improve the actual spatial resolution limit of silicon-based radiation detectors [12]. The central idea for achieving this goal is related with the possibility to adopt a thin silicon diode as the active layer of the detector. As already discussed, reducing the thickness results in a smaller charge spreading and in a minor sensibility to  $\delta$ -electrons. Due to the reduced thickness, the small amount of produced charge must be picked up by an appropriate system. This task is done by using nanostructured conductors that work as charge collectors and allow to place the read-out electronics at a proper distance from the detector, thus reducing the total capacitance of the device.

The goals of the NanoChanT project are to develop the technologies required to implement the proposed position particle detector and to verify the feasibility of device. The realization of a prototype of such a detector is the final scope.

The proposed configuration is schematically composed by a three layer structure (Figure 1.8). An ordered array of nanoconductors is placed between an active medium and the read-out electronics. The enhanced spatial precision is related to the employment of a thin active layer, which is thought to be realized with a reverse polarized silicon diode. When an ionizing particle traverses the active layer, the produced charge is driven, via the nanoconductors, to the read-out electronics.

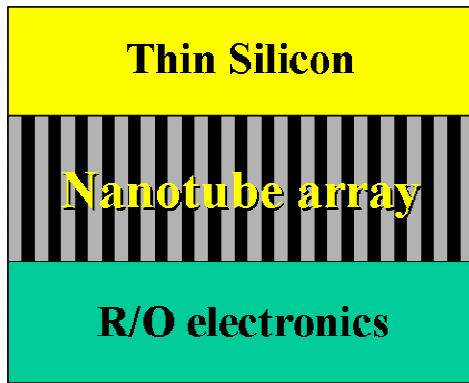


**Figure 1.8.** Basic idea for the novel detector proposed by the NanoChanT project.

For optimizing the charge collection, nanoconductors have to be highly uniform in size and spacing, and electrically insulated from each other. Nanoconductors having diameter in the range 10 – 100 nm and metal electrical properties are required.

A layer of porous Anodic Aluminium Oxide (AAO), 50 – 100  $\mu\text{m}$  thick, will act as mechanical framework, with suitable dielectric properties, for the separation of such 1-D structures. These thicknesses are required in order to allow the handling of the AAO, or alumina, layer. Highly ordered arrays of parallel nanochannels in alumina can be obtained, with size and pitch in the range 10 – 200 nm and 40 – 400 nm, respectively. The mechanical stiffness of the device is guaranteed by the AAO template and the read-out silicon substrate. The active layer may be kept thin so that the space resolution of the detector can, in principle, scale as the pitch of the nanopores.

Inside the pores, nanoconductors have to be grown. They could be either Carbon Nanotubes (CNTs) or metal nanowires. They both show the conductive electrical properties that are required for the realization of the device. However, CNTs exhibit some particularly intriguing properties that make them more appealing, especially for possible further developments of the detector. Indeed, the possibility of doping CNTs has been reported [13-15]. They could so be used as diodes of nanometric size, acting themselves as the active material of the detector. Moreover, they could be used in future as charge amplifiers, given their application as field effect transistors. In particular, CNT-based field effect transistors in a vertical configuration and with high density have been realized employing the synthesis of CNTs inside the pores of an anodic aluminium oxide template [16]. Mainly, for this reason the research has been principally directed toward the employment of CNTs rather than metal nanowires.

For growing CNTs inside the alumina template, small amounts of cobalt have been electrodeposited at the bottom of the alumina nanochannels to act as a catalyst for the synthesis of CNTs. Finally, CNTs synthesis is obtained via Catalyst-assisted Chemical Vapour Deposition (C-CVD) of hydrocarbons.

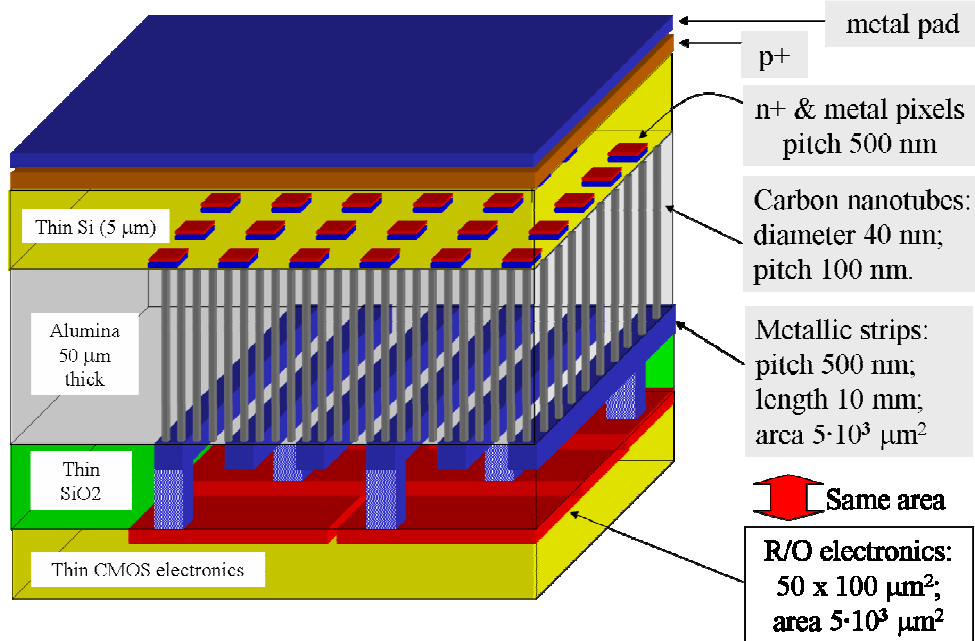


**Figure 1.9.** Possible geometry for the detector proposed by the NanoChanT project.

A possible 3-D design of the detector is shown in Figure 1.9. The sensing layer, which extends over an area of  $1 \times 1 \text{ cm}^2$  size, is a thin reverse biased silicon diode with  $n^+$  implantations segmented in form of pixels with submicron pitch. Pitches down to 500 nm can be obtained by means of the currently available lithographic technology. Electrons collected at the pixels are driven by groups of CNTs to metallic strips having the same pitch of the pixels and length of 1 cm. These strips are connected to the read-out electronics through a thin insulating silicon dioxide layer by short vias. The read-out layer is made of CMOS electronics embedded in a silicon substrate, with each channel covering an area of  $5 \cdot 10^3 \text{ μm}^2$ . The present scale of integration of CMOS electronics limits the read-out to only one spatial coordinate and the granularity to values much larger than the expected alumina and nanoconductor pitch. Future developments in the CMOS electronics might fully benefit of this nanometric scale.

Several milestones have to be overcome for the realization of the device:

- The fabrication of anodic aluminium oxide templates with an ordered structure of nanopores having suitable diameter and pitch;
- A uniform deposition of metal catalyst for the carbon nanotubes synthesis at the bottom of the aluminium oxide pores;
- A uniform synthesis of the carbon nanotubes inside the template;
- The bonding of the aluminium oxide template and the silicon layers;

- A reliable low ohmic resistance electrical bonding between the carbon nanotubes matrix and the metal pixels on the silicon diode electrode;
- The verification of the working principle of a prototypal detector with ionizing particles.

Each step represents the state of the art of the relative research field, and hence to be successfully applied in a unique device they require a deep and dedicated investigation.

The current design plans to use binary read-out logic for every channel. A hit or miss signal is produced by the front-end electronics. The minimal design is planned to consist of a CMOS charge-sensitive preamplifier and a threshold comparator, in order to detect the gathering of a charge above a given threshold.

The thickness of the reversely-biased silicon diode has not been determined so far. Its value will be tuned by imposing the condition that a minimum ionizing particle produces a signal detectable by the read-out electronics. An efficient charge transport through the interfaces and along the CNTs must be optimized in order to achieve high charge collection efficiency. To measure and optimize this efficiency, some intermediate structures are foreseen to be tested by means of the passage of ionizing particles with known energy through the active layer. Preliminarily, not confined but free-standing configurations of CNTs films will be used for testing the quality of the electrical bondings.

For obtaining a large efficiency in the detection, it is necessary to achieve high signal-to-noise ratios. The noise of a signal is typically expressed as Equivalent Noise Charge (ENC) and, among other parameters, depends on the detector capacitance and the input gate capacitance of the front-end electronics [17]. Also the leakage current of the detector, which depends on the volume of the sensing layer and on the working temperature, contributes to the signal noise.

In the proposed configuration, a CMOS preamplifier circuit will process the signal directly on the detector before transmitting it to higher level circuitry. Keeping as short as possible the connections between the active layer and the preamplifier contributes at reducing the total capacitance. Recent advances in CMOS technology reported that low gate capacitance of charge-sensitive preamplifiers can be achieved, approximately down to 15 – 40 fF [18]. In order to maximize the signal-to-noise ratio the condition of matching the sum of the detector capacitance and the feedback capacitance of the preamplifier with the capacitance of the CMOS gate must be fulfilled [19]. On a side, the feedback capacitance is a parameter that can be easily varied with the geometry design of the feedback element. On the other side, the detector capacitance consists of different contributes, that can not be reliably evaluated at the moment, since they depend also on the properties of the interfaces between the different layers. As an example, if active layer thicknesses of 5 – 10  $\mu\text{m}$  are used in the configuration proposed in Figure 1.9, the

capacitance seen by a single strip can be approximately evaluated as 15 – 25 fF for a fully depleted diode. In similar conditions, where the capacitance of the detector and of the input gate of the front-end electronics have values of 15 – 40 fF, the Equivalent Noise Charge (ENC) has been reported to be approximately as low as 20 – 40  $e^-$  [18]. For the supposed thicknesses of 5 – 10  $\mu\text{m}$ , being the average generation rate of electron-hole pairs in silicon approximately 80 pairs per micron, 400 – 800 pairs will be produced. The leakage current is very low already at room temperature for these thicknesses and, for typical sampling frequencies, its contribution in terms of ENC can be neglected [20].

The signal-to-noise ratio turns out to be between 10 and 40. It is clear that this is only an indicative value and that a more realistic calculation of the signal-to-noise ratio will have to be done on prototypal devices.

Since a binary read-out CMOS electronics will be used, it is necessary to limit the charge spreading in the silicon layer. The charge spreading depends on the depletion voltage applied at the p-n junction. In fact, as already discussed, half the charge is contained within a radius

$$\sigma_{50\%} = 0.95\sqrt{Dt_D} = 0.95\sqrt{\frac{D}{\mu} \times \frac{s^2}{V}} = 0.95s\sqrt{\frac{KT}{e} \times \frac{1}{V}} \quad (1.2)$$

where  $\mu$  is the carrier mobility,  $D$  the diffusion constant,  $s$  the drift length,  $\frac{KT}{e} = 0.026 \text{ V}$  and  $V$  is the applied voltage.

Generally, high resistivity (1 – 20  $\text{k}\Omega\cdot\text{cm}$ ) silicon substrates are employed for the fabrication of silicon detectors. However, such high purity may be degraded by the high temperatures of the technological steps required for the NanoChanT detector. A lower resistivity has thus been foreseen for the application. For a 500  $\Omega\cdot\text{cm}$  silicon resistivity, the minimum voltage to deplete the junction is approximately 1 V and 0.20 V for a junction thickness of 10 and 5  $\mu\text{m}$  respectively.

In order to contain as much as possible the charge spreading, higher depletion fields can be applied, provided that the breakdown limit voltage of the device is not exceeded. Generally, voltages up to 500 – 800 V can be applied at detector thicknesses of 250 – 300  $\mu\text{m}$  before the junction undergoes a breakdown event. For thicknesses of 5  $\mu\text{m}$  and 10  $\mu\text{m}$ , depletion voltages of 2.5 V and 10 V are respectively enough to gather half the charge cloud inside the 500 nm pitch of the read-out electronics.

The overall precision of the detector will thus be  $\sigma = \frac{pitch}{\sqrt{12}}$ . For the supposed pitch value of 500 nm, this finally turns out to be 150 nm, approximately an order of magnitude lower than the precisions achievable in the commonly used detectors. The high signal-to-noise ratio evaluated, between 10 and 40, for the analyzed configuration is largely satisfactory, so to justify the investigation on the proposed novel detector.



## Chapter 2 Nanotechnologies involved in the project

Nanotechnology is the topic that deals with physics and devices in the nanometric scale. Nanostructures are defined as having at least one dimension between 1 and 100 nm. They can have three, two or only one dimension in such a scale, being referred as 0-dimensional, 1-dimensional or 2-dimensional nanostructures, respectively. Quantum dots and quantum wells are other adopted names for the 0- and 2-D nanostructures. Nanowires, nanotubes and many other objects populate the 1-D nanostructure family.

In the last decades they have gathered growing interest because of their peculiar properties, which can be largely different from their bulk counterparts. This has opened new technological possibilities and new physical phenomena to be developed and investigated. The number of publications related to the Nano-World followed an almost exponential growth since the mid-80s (Figure 2.1). In particular, the miniaturization trend of microelectronics leads the group of all the fields where nanostructures promise to create new opportunities. The properties of such objects result to be ruled by a “new” physics, as quantized (or ballistic) conductance, Coulomb blockade (or SET, Single Electron Tunnelling), size-dependent excitation or emission and metal-insulator transition [21]. The high surface-to-volume ratio and the quantum confinement of electrons by the potential wells of nanometre-sized structures are the causes of this deviation from the well-known bulk material properties.

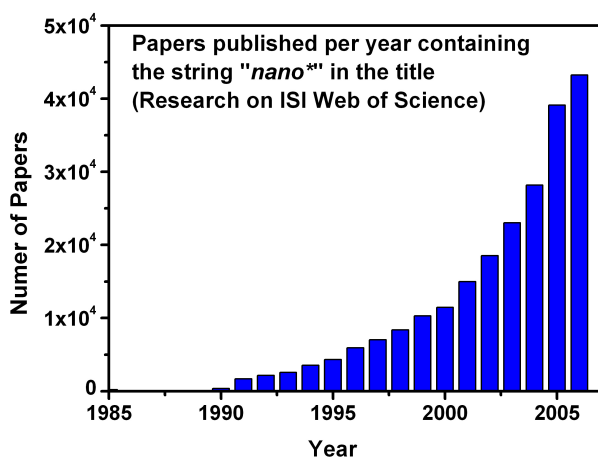


**Figure 2.1.** The explosion of the Nano-World as measured by the number of publications per year.

Controlling the size of these nanostructures may provide a powerful and versatile method to control the electrical, optical, magnetic and thermoelectric properties of a solid-state functional material. Nanostructures are consequently expected to play a crucial role as both interconnects and functional units in the fabrication of nanodevices, following a “bottom-up” approach. The applications of such nano-sized objects (nanodots or nanowires), are investigated for a variety of electronics, optoelectronics, thermal and mechanical devices [21, 22]. To make this scenario actual, some problems have still to be overcome. That is, synthesis and fabrication of nanostructures with well-controlled dimensions, morphology, phase purity and chemical composition are far to be successfully achieved. In particular, for synthesizing 1-D nanostructures different methods have been developed, all based on an anisotropic growth, imposed either by external constraints, like in catalyst-driven synthesis or in templated one, or by intrinsically anisotropic crystallographic structure of the solid.

The NanoChanT project idea rests on three nanostructures in particular, that is anodic aluminium oxide, metal nanowires and carbon nanotubes. As discussed before, the feasibility of the carbon nanotubes solution has been investigated in this thesis.

### 2.1 Carbon nanotubes

Carbon Nanotubes (CNTs) were firstly observed by Endo in the mid-1970s [23], but only in 1991 Iijima reported clearly about their existence [24]. Because of their peculiar electronic and mechanical properties, they have gathered a wide interest in materials science research and many other fields are currently looking at them for new intriguing applications. An almost exponential growth of the number of publications on CNTs per year has thus been established (Figure 2.2), and many reviews refer about their properties and possible applications [25-28]. A not all-embracing list includes robust and lightweight composites, gas storage devices, gas sensors, vacuum microelectronic and electronic devices.

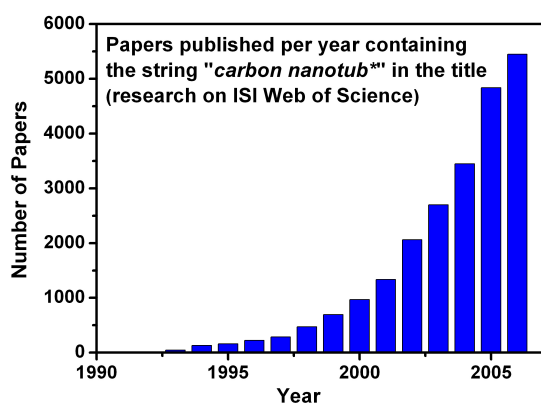


**Figure 2.2.** Carbon Nanotubes largely contribute to the research on the Nano-World, as indicated in the Figure.

CNT-based composites are investigated mainly because the high aspect ratio (length to radius ratio) and high conductivity make these materials excellent for conducting applications. Electrostatic applications of such composites have been used in car painting. Furthermore, CNTs are used to strength the mechanical and thermal properties of composite materials and are especially intriguing for low weight structural composites. Carbon nanotubes are also employed as template for creating composite nanowires structures, for instance, by means of direct vapour evaporation of other metals on the tubes surface [21]. If open CNTs are used, also metal or gas filling can be achieved by means of capillarity or high pressure injection. The former arrangement is again utilized to synthesize 1-D structures, whereas the latter can be used for gas storage, of H<sub>2</sub> for example. Because of their mechanical stiffness and nanometric dimensions they have been investigated as alternative tips in scanning probe microscope. These applications are already on the market. CNTs are efficient sensors for many gases, such as NO<sub>2</sub>, NH<sub>3</sub>, H<sub>2</sub>O, CO and CO<sub>2</sub>. The basic mechanism involves modifications in electric transport features along the tubes, when exposed even at low concentrations of the external gas. The presence of gases can be revealed by monitoring changes of resistance or capacitance [27, 29]. Other promising or already developed fields of applications for CNTs are electrochemistry (Li<sup>+</sup> batteries, supercapacitors, fuel cells and actuators) [27, 28], and bio-medicine [30].

Generally speaking, it is worth noting that the quality of the carbon structure can be tuned depending on demands of the final application. Not always a defect-free CNT is indeed necessary. An optimum control of the structural properties is required in electronic applications, where CNT chirality, location and presence of defects strongly affect the electronic properties. For composites or thermal conductor applications, such a structural perfection is not needed. Also constraints on the dimension change in a similar way.

In the following, a brief description of the CNT structural and electrical properties is given, and some electronic applications are shortly described. Then, the different CNT synthesis techniques are discussed. Finally, among the other possible applications, CNT-based field emission applications are discussed.

### *2.1.1 Structures and properties*

Carbon belongs to the IVA group of the element table, having four electrons in its outer valence shell; the ground state configuration is  $2s^2 2p^2$ . Due to the similar energies of these electrons, hybridization normally occurs. Three possible hybridizations exist for carbon, that is  $sp$ ,  $sp^2$ , and  $sp^3$ . The first one gives rise to chain structures, second one to planar structures and the third to tetrahedral structures. In diamond, carbon atoms exhibit  $sp^3$  hybridization, in which four bonds are directed toward the corners of a regular tetrahedron, with a bond length between  $sp^3$  carbons of 1.56 Å. The resulting 3-dimensional network is extremely rigid, which is one reason for diamond hardness. Since all electrons are localized in the bonds, diamond behaves as an insulator. In graphite  $sp^2$

hybridization occurs. Each atom is connected to three carbons (bond angle =  $120^\circ$ ) in the XY plane, and a weak  $\pi$  bond is present in the Z axis. The C–C  $sp^2$  bond length is 1.42 Å. A hexagonal (honeycomb) lattice, typical of a sheet of graphite, results from the  $sp^2$  framework. The spacing between the carbon layers is 3.35 Å. Electrons of the  $p_z$  orbital are weakly bound, namely by a Van der Waals bond, and thus they result delocalized. That is, electrons of the  $p_z$  orbital are free to move within this cloud and are no longer local to a single carbon atom. This phenomenon explains why graphite can conduct electricity.

Carbon nanotubes (CNTs), considered as a new form of pure carbon, can be visualized as rolled hexagonal carbon networks that are capped by pentagonal carbon rings. There are two types of carbon tubes: single-wall (SWNTs) and multi-walls (MWNTs). Ideally, the former structure results by the rolling of a single carbon network, whereas the latter consists of many nested coaxial array of single-wall CNTs. Both  $sp^2$  and  $sp^3$  hybridizations exist in the CNT structure, the latter induced by the curvature of the graphene sheets.

The structure of a single-wall CNT can be described in terms of its 1-D cell, defined by the chiral vector  $\mathbf{C}_h$  and the translational vector  $\mathbf{T}$  (Figure 2.3). The former determines the direction of rolling a graphene sheet and the tube diameter. It is defined as the vector that connects two crystallographically equivalent sites in the starting graphene sheet. Named  $\mathbf{a}_1$  and  $\mathbf{a}_2$  the unit vectors of the hexagonal honeycomb lattice of the graphene plane, it can be expressed as  $\mathbf{C}_h = n \mathbf{a}_1 + m \mathbf{a}_2$ , where (n, m) are the coordinates of the lattice point superimposed with the origin, defined as (0, 0). The vector  $\mathbf{T}$  is defined by the first intersection of the direction perpendicular to  $\mathbf{C}_h$  with the graphene lattice.

Consequently, the diameter of the tube results to be  $d = \frac{a\sqrt{m^2 + mn + n^2}}{\pi}$ , where  $a$ , equal to  $1.42 \times \sqrt{3}$  Å, corresponds to the lattice constant in the graphene sheet. A typical SWNT diameter can be approximately 1.4 nm, whereas MWNTs can achieve also a hundred of nanometres.

Three different types of SWNT can be generated depending on the different chiral angle  $\theta$ , defined as the angle between the (0, m) direction and  $\mathbf{C}_h$  (or equivalently (n, m)).

Armchair tubes are defined by chiral vector as (p, p), zigzag one by (p, 0), and the remaining are called chiral. The respective electronic properties changed from metallic to semiconductor. Theoretical studies indicate that all armchair tubules, i.e. (p, p), are metallic, as well as zigzag ones for which  $\frac{2m+n}{3}$  is an integer. All the others are semiconductors, with band gaps that depend on the tube chirality and diameter. It is worth noting that this difference does not come from different chemical bonding between carbon atoms. The exceptional electronic properties of CNTs are caused by the quantum confinement of electrons normal to the nanotube axis. In the radial direction electrons are confined on the graphene sheet and thus electrons can propagate only along the nanotube

axis. The resulting density of the states (DOS) function depends on the standing waves that are thus allowed (Figure 2.3).

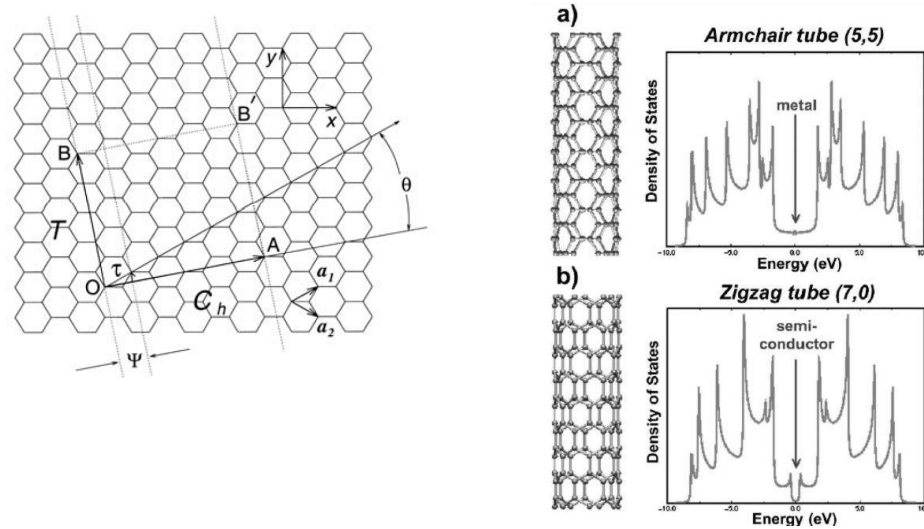


**Figure 2.3.** On the left, the definition of the 1-D cell of a SWNT by means of its chiral vector  $C_h = na_1 + ma_2$  ( $a_1$  and  $a_2$  are the unit vectors on the honeycomb lattice of carbon atoms) and its chiral angle  $\theta$  (measured with respect to the zigzag axis). The translation vector  $T$  is also depicted [25]. On the right, density of states (DOS) for a metallic armchair SWNT (a) and for a semiconductor zigzag SWNT (b). Spikes in the DOS result from the 1-D quantum confinement of the structures [27].

The resulting properties of single-wall and multi-walls CNTs have been widely investigated, ranging from electronic to mechanical and thermal ones [25-28]. Generally, it is worth noting that the CNT properties depend on the actual geometrical structure (defects, chirality, diameter, etc) of the tubes and on degree of crystallinity. Therefore, CNT physical properties are determined by the experimentally measured tubes or bundles and thus they also depend on the utilized synthesis technique.

The ability of synthesize CNTs with a given chirality is fundamental in electronic applications since the electrical properties of the tubes depend on their chirality. Furthermore, it is highly desirable to be able to grow CNTs in a particular location and in a specified direction on a substrate. The latter issue seems to have been achieved so far, even if partially. The former is still a challenging field in the CNT researches.

If low ohmic contact resistance between the tube and the metal leads is achieved, the intrinsic electrical properties of the CNTs can be studied. MWNT conductivity measurements have demonstrated both metallic and semiconducting behaviours. At 300 K resistivity has been measured between  $1.2 \cdot 10^{-4}$  and  $5.1 - 5.8 \cdot 10^{-6} \Omega \cdot \text{cm}$ . Band gap for semiconductor SWNTs varies between 10 and 500 meV, even if they have similar diameters. For same-chirality semiconductor nanotubes, the band gap is inversely proportional to the diameter.

At room temperature, both SWNTs and MWNTs exhibit diffusive transport behaviour, if metallic. Resistances on the order of tens to hundreds of k $\Omega$  have been measured in metallic SWNTs with several microns length. At low temperatures SWNTs can behave as quantum wires. Electron conduction in a single perfect CNT occurs through discrete electron states over large distances, namely many hundreds of nanometres. This behaviour is referred to as ballistic transport, and involves a conduction mechanism without electron scattering. It has been experimentally revealed, since the conductivity approaches the theoretical quantum conductance limit of  $2G_0 = 4\frac{e^2}{h}$ , i.e. 6.45 k $\Omega$  in resistance. For metallic SWNTs the coherence length is extremely long and the presence of defects does not alter the situation. For semiconductor ones, the coherence length is considerably shorter.

On the other side, MWNTs show a similar behaviour, in spite of their larger diameter and multiple shells. In fact, it has been in fact reported that the current transport is dominated by the outer metallic shell [31]. Only slightly differences occur because of additional coupling between nested shells. There are thus some evidences that, under certain circumstances, the transport in MWNTs can be ballistic too [25, 26].

Quantum phenomena as single electron charging (or Coulomb blockade) occur on CNTs that are poorly contacted with the metal leads. This phenomenon occurs if two conditions are met by a small metallic dot (here a tube) connected to two electrodes. The first condition is that the contact resistance is larger than the resistance quantum  $R_Q = \frac{h}{2e^2}$ . The second is that the dot is sufficiently small, hence the capacitance small, so that the energy needed for adding an electron to the system, i.e.  $\frac{e^2}{C}$ , is larger than the thermal energy  $K_B T$ . The capacitance of a CNT scales linearly with the inverse of its length. For a micron long CNT, the single electron energy is high enough for the Coulomb blockade to be observed at about 4 K. Electron transport occurs thus via individual electrons.

Besides to allow investigating the intrinsic electronic properties of CNTs, to establish reliable low ohmic contacts is one of the milestones in the integration of CNTs in the IC technology. Generally, contact resistances between CNTs and leads can be of the order of several decades of k $\Omega$  up to M $\Omega$ . Titanium-based contacts seem to allow the achievement of the best results [32].

Carbon nanotubes can carry extremely high current density before failing as a result of electromigration. The maximum achievable current densities,  $10^9 - 10^{10}$  A/cm<sup>2</sup> [28] are largely higher with respect to the one of any metal. It is three orders of magnitude larger than the Cu one. Consequently, CNT-based vertical interconnects, or vias, seem to

represent an optimum solution in replacing metal vias in silicon ICs, where the reducing of the features sizes forces interconnects to withstand larger current densities [33].

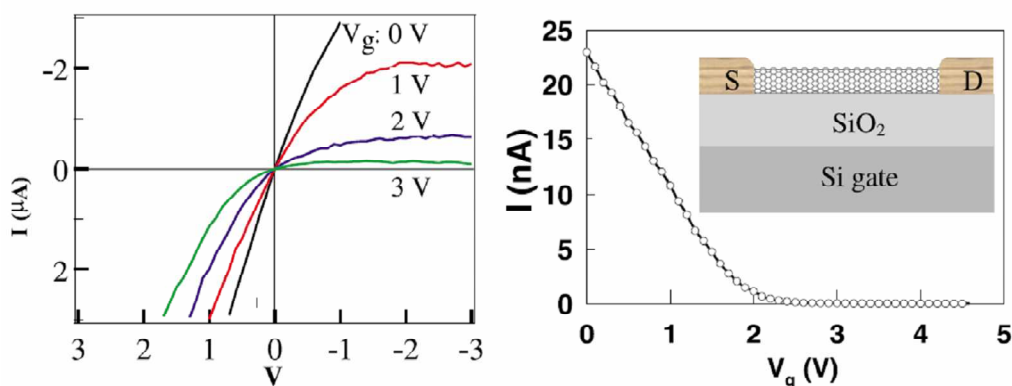


**Figure 2.4.** Field effect transistor behaviour for an individual SWNT. On the left, I–V curves for a semiconducting SWNT under various gate voltages  $V_g$ . The gate voltage is applied to the sample substrate illustrated on the right part. On the right, the I vs.  $V_g$  characteristic for the nanotube is also shown [29].

Semiconducting SWNTs exhibit Field Effect Transistor (FET) behaviour (Figure 2.4) at room temperature [29]. That is, their conductance can be changed dramatically (by orders of magnitude) by gate voltages. As-grown semiconducting SWNTs have been proved to be hole-doped p-type FETs, with holes depletion and diminished conductance (from typically 100 k $\Omega$  to 1 M $\Omega$ ) by positive gate voltages. The natural-occurring of the p-type has been associated with molecular oxygen adsorption by the SWNTs. Removal of  $\text{O}_2$  leads to recover nearly intrinsic semiconducting behaviour. Furthermore, it is also possible to dope CNTs with the intention of creating a p–n junction [13]. In analogy with bulk semiconductors as Si, N and B dopants can be used to change the majority carrier from p-type to n-type in a CNT. MWNTs have been used as n- and p-type material so that novel p–n junctions and transistors can be created. It has been shown that N-doped CNTs behave as n-type nanowires [14], whereas B-doped tubes act as p-type conductors [15]. Other species have been used for CNTs doping, such as  $\text{Br}_2$ ,  $\text{I}_2$  as hole-dopants and K and Cs as electron-dopants. A progressive K-doping has been reported to make a semiconductor SWNT evolve from p-type to intrinsic and then to n-type semiconducting states [34].

Additionally, the existence of SWNT metal–semiconductor junctions, created by the presence of a defective pair heptagon–pentagon in the tube, has been revealed. This structure behaves like a rectifying diode.

Semiconducting CNTs have thus been intensively explored in recent years for nanoelectronics devices, including transistors, and logic devices. Large on-off ratio, high gain ( $> 10$ ) and room temperature operation has been proved in real CNT-based FET devices. Many digital logic devices have thus been produced, namely an inverter, a logic

NOR, a static random-access memory and an AC ring oscillator. Also OR, AND, NOR and NAND logic-gate structures have been developed by employing crossed nanotubes p-n junctions and junctions arrays [13, 35].

Besides horizontal configurations with respect to the substrate, CNT-based field effect transistors have been proposed also in a vertical arrangement, in order to achieve a higher integration density in real devices [16, 33]. In particular, a high CNT-based FET density have been reached employing the synthesis of CNTs inside the pores of an anodic aluminium oxide template [16].

### 2.1.2 *Synthesis of carbon nanotubes*

Many groups are focused on the definition of a reliable synthesis model for describing the CNT growth and many mechanisms have been proposed. However, it is very difficult to control actual experimental conditions and to monitor the CNT nucleation. In-situ characterizations seem to be needed for verifying theoretical models and thus advancing in this field.

Hence, a unique synthesis model has not been established so far. Some models had been developed for accounting the growth of carbon filaments by means of pyrolytic approaches. Namely they involve carbon diffusion through the catalyst nanoparticles or carbon diffusion on the catalyst nanoparticles. Besides, the former situation is separated in two sub-cases depending on the position of the catalyst during the growth, at the top of the carbon filament (“tip-growth”) or at the bottom (“base-growth”). These models have been considered also to describe, under some adaptations, the growth of CNTs [36, 37]. It has to be stressed that they all agree in predicting that the dimension of the synthesized CNT is strongly correlated to the dimension of the catalyst nanoparticle. Hence, metal nanoparticles of controlled size can be used to grow CNTs of controlled diameter, determining the formation of SWNTs or MWNTs [38, 39]. Broadly speaking, when the particle size is a few nanometres, SWNTs form, whereas a few tens of nanometres wide particles favour MWNTs formation. Thin films of catalyst coated onto various substrates have also proved successful in achieving uniform CNT deposits [40].

The bulk carbon diffusion models involve the decomposition of the carbon feedstock gas on the top surfaces of the metal catalyst and the creation of  $H_2$  and  $C_n$  species. The carbon fragments then diffuse through the catalyst nanoparticle and precipitate at the other side of the filament, at the colder zone of the particle, thereby allowing the filament to grow. This process continues until the catalytic activity of the nanoparticles is neutralized or the carbon species stop reacting with the exposed end. This model, known as Vapour – Liquid – Solid (VLS) model, was firstly developed by Wagner first [41] and then Baker [42] and it involves the creation of a liquid metal carbide compound which, when a super-saturation is reached, precipitates out in the solid form of a fullerene cap extending into a carbon cylinder, with no dangling bonds and, hence,

minimum energy. The achievement of conditions under which the carbon-containing metal nanoparticles is melted results favoured by the nanometric size of the clusters and by the presence of a carbide solution [43, 44].

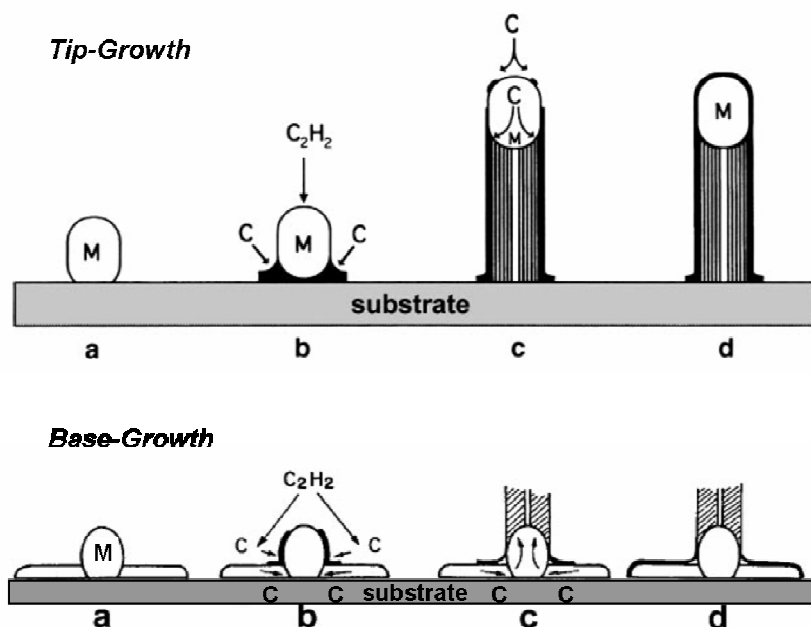


**Figure 2.5.** Bulk diffusion growth model. The metal particle (M) catalyzes the pyrolysis of the carbon-containing gas (here  $C_2H_2$ ). Carbon diffuses through the metal and then precipitates at the other end in the form of graphite. Above, the metal particle remains at the top of the tubule (“tip-growth”). Below, it remains attached at the substrate (“base-growth”) [27]. The process continues until the catalytic activity of the particle is deactivated.

Depending on the adhesion of the catalyst at the substrate, the nanoparticle can be lifted up during the CNT growth, and hence a “tip-growth” occurs, or it can stay rooted at the substrates, having a “base-growth” (Figure 2.5). It is not rare to find as results of the same synthesis process, both the kinds of growth on the same sample. Moreover, the graphene sheets tensile strength can split part of the liquid particle, which is thus included inside the tube length.

A different model involves the diffusion of carbon on the catalyst nanoparticle surfaces rather than in its bulk, and hence the carbon precipitation at the other end of the particle (Figure 2.6) [23, 45].

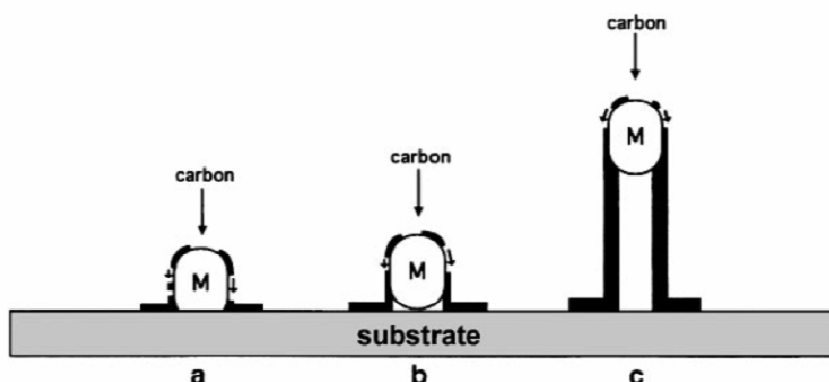


**Figure 2.6.** Surface diffusion growth model. Differently from the previous case, after the pyrolysis of the carbon feedstock gas, carbon diffuses on the surface of the particle and then precipitates in the form of graphitic domains [27].

Other different mechanisms have been proposed, involving solid state of the nanoparticles during growth [37] or preferential growth at mono-atomic step edge in catalyst clusters [46]. The issue is still far to be resolved. It has to be noted that there may be not a unique mechanism for the production of carbon filaments and nanotubes using the hydrocarbon decomposition at elevated temperatures. By changing parameters such as type of hydrocarbon, metal catalysts, nanoparticles size, carrier gases and temperature, different filaments having various morphologies and degrees of graphitization can result.

CNTs (single- or multi-walls) can be produced using different methods, which mainly involve gas phase processes. The main techniques are nowadays the electric arc-discharge, the laser ablation and the chemical vapour deposition (CVD) ones [25, 47].

The optimal conditions for CNT generation using the electric arc-discharge technique involve the passage of a direct current (80–100 A) through two high-purity graphite electrodes separated by ~1–2 mm, in He atmosphere (500 Torr) (Figure 2.7, left). Also  $\text{CH}_4$  and  $\text{H}_2$  have been successfully employed in the production of high quality CNTs.

During arcing, a deposit forms on the cathode, whereas the anode is consumed. The deposit consists of curved and dense graphene layers and of bundle-like structures, which exhibit randomly arranged MWNTs and graphitic particles. In addition to MWNTs, SWNTs can also be produced if a metal catalyst is added in the graphite anode rod. The arc method usually involves high purity graphite electrodes, metal powders (for producing SWNTs), and high purity He and Ar gases; thus the costs associated with the production of SWNTs and MWNTs are high. Although the crystallinity of the material is high and the yield per unit time is also larger than the other methods, due to the higher growth temperature involved in the arc-discharge method, there is no control over dimensions (length and diameter) and alignment of the tubes. Moreover, by-products such as

polyhedral graphite particles (in case of MWNTs), encapsulated metal particles (for SWNTs) and amorphous carbon are also formed.

A different method of producing MWNTs is a high-power laser vaporization of pure graphite targets, inside a furnace at 1200 °C, in Ar atmosphere. The laser furnace consists of a furnace, a quartz tube with a window, a target carbon composite (doped with catalytic metals if SWNTs have to be produced), a water cooled trap, a flow systems for the buffer gas to maintain constant pressures and flow rates (Figure 2.7, right). A laser beam (typically a YAG or a CO<sub>2</sub> laser) is introduced through the window and focused onto the target located inside the furnace. The Ar flow rate and pressure are typically 1 cm/s and 500 Torr, respectively. The produced CNTs are conveyed by the buffer gas to the trap, where they are collected.

High crystallinity has been reported to originate in high-power laser vaporization and homogenous annealing conditions, but also with this technique a purification process is necessary to remove low quality by-products. Moreover, a better control in the CNT morphology is achievable. Actually, it was noticed that the diameter of the tubes depends upon the laser power. Increasing the laser pulse power, the diameter of the tubes becomes narrower. Also furnace temperature, catalytic metal type and flow rates affect the SWNT diameter. However, the laser technique is not economically advantageous because it involves high-purity graphite rods and high laser powers are required.

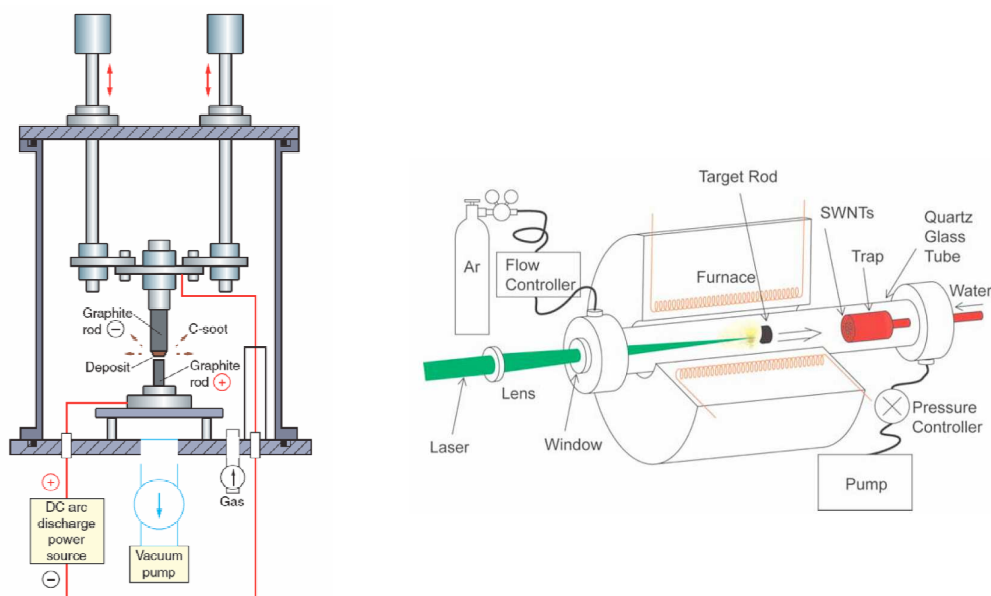


**Figure 2.7.** Schematic diagrams of the arc-discharge (left) and the laser ablation (right) apparatus for the CNT synthesis [47].

Catalyst-assisted Chemical Vapour Deposition (C-CVD) is one of the most promising methods for producing CNTs. It involves a thermal decomposition of a carbon-containing vapour (generally a hydrocarbon) in the presence of a metal catalyst.

Compared with arc-discharge and laser methods, CVD is a simple and economic technique for synthesizing CNTs at low temperature and ambient pressure. This is fundamental for the integration of CNTs synthesis process in the IC technology, even if a price to pay for this integrability is a lower crystallinity of the CNTs. Another advantage of this technique is the versatility. It can use a variety of hydrocarbons in any state (solid, liquid or gas), it is ideally suited for growing aligned CNTs on desired substrates for specific applications, which is not feasible by arc and laser methods, and it allows CNT growing also in desired architectures of nanotubes at predefined sites on a patterned substrate. Finally, it also offers better control over growth parameters.

A diagram of the setup of a basic CVD system for CNT growth is displayed in Figure 2.8. The process involves passing a hydrocarbon vapour (typically for 15–60 minutes) through a tube furnace in which a catalyst material is placed at sufficiently high temperature (600–1200 °C) to decompose the hydrocarbon. CNTs grow over the catalyst and are collected upon cooling the system to room temperature. In case of a liquid (benzene, alcohol, etc.) or solid hydrocarbon (camphor, naphthalene, etc.), a vaporization of the carbon-containing precursor is performed in another furnace at lower temperature, and after an inert gas purged through it, to carry the vapour into the reaction furnace. The catalyst material may also be solid, liquid or gas and can be placed inside the furnace or fed in from outside. Pyrolysis of the catalyst vapour at a suitable temperature liberates metal nanoparticles *in situ*. Alternatively, catalyst-plated substrates can be placed in the hot zone of the furnace to catalyze CNT growth.

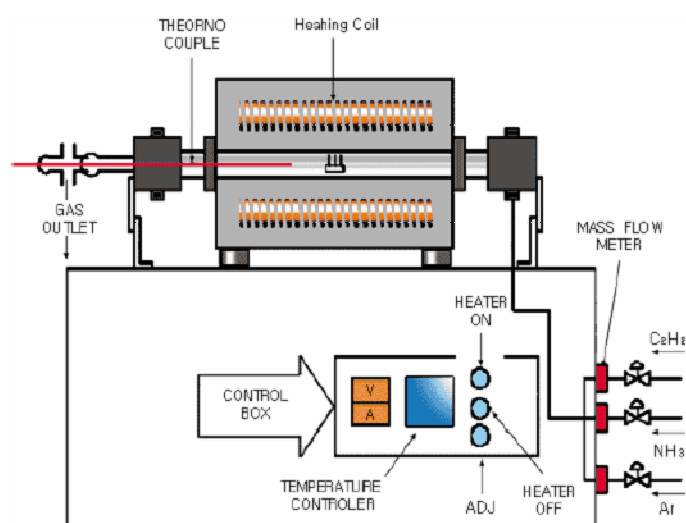


**Figure 2.8.** Schematic diagrams of the CVD apparatus for the CNT synthesis.

In addition, the material, morphology, and textural properties of the substrate greatly affect the yield and quality of the resulting CNTs. Strong metal-support interactions allow high metal dispersion and, thus, a high density of catalytic sites and prevent metal species from aggregating and forming unwanted large clusters that lead to graphite particles or defective MWNTs [48]. Silicon, silicon dioxide, graphite are commonly employed substrates. Alumina materials are reported to be good catalyst supports because of their strong metal-support interaction.

The three main parameters for CNT growth in CVD are the carbon feedstock and catalyst type and the growth temperature. MWNTs are generally produced by CVD at low-temperature (600 – 900 °C), whereas higher temperatures (900 – 1200 °C) are required for SWNT growth. This indicates that SWNTs have a higher energy of formation, owing to their small diameter, which results in high curvature and high strain energy. Consequently, MWNTs are more easily grown from most hydrocarbons.

For obtaining high yields of pure CNTs it is fundamental to achieve hydrocarbon decomposition on catalyst sites alone, avoiding spontaneous pyrolysis, which can result in the deposition of amorphous carbon or defective structures. Common efficient precursors of MWNTs (e.g.  $C_2H_2$ ,  $C_6H_6$ , etc.) are unstable at higher temperatures and thus lead to the deposition of carbonaceous by-products. On the contrary, SWNTs can only be grown from selected hydrocarbons (e.g. CO,  $CH_4$ , etc.) that have a reasonable stability in the temperature range of 900 – 1200 °C.

Transition metals (Fe, Co, Ni) are the most commonly used catalysts for CNT growth [36, 49], since phase diagrams suggest finite solubility of carbon in these transition metals at high temperatures. The fact that these metals are efficiently used also in arc-discharge and laser methods indicates that the different methods might have common growth mechanisms for CNTs, which are not yet clear. They exhibit similar catalytic behaviour, but the relative CNT syntheses slightly differ in terms of graphitization and dimension of the products and the growth rate [49]. Also bi-metallic catalysts, such as Fe-Mo, have been recently triggered new interest for yielding high purity CNT growth. A detailed overview over the catalyst role in the CVD synthesis can be found in [36].

Microwave plasma-enhanced chemical vapour deposition (PE-CVD) systems have been widely used to grow continuous carpets of aligned carbon MWNTs, using different substrates, carbon sources and metal catalysts at lower temperatures with respect to the ones employed in a standard CVD process [50]. This approach is also advantageous for depositing vertically aligned CNTs and it allows the synthesis at temperatures more compatible with the ones commonly adopted in the IC silicon technology. However, it has been reported that the quality of the PE-CVD synthesized CNTs is considerably lower with respect to that of the CNTs produced by means of the CVD process [51].

Another technique is based on template growth [16, 52]. Usually a highly ordered nanoporous alumina is adopted as a template. Cobalt catalyst is electro-deposited inside the template channels. Large arrays of parallel and insulated CNTs can be produced at 650 °C, with geometrical features (diameters, length and density) tuneable by varying the pore dimensions. High periodicity and uniformity can be achieved, but the structural quality of the CNTs is not satisfactory so far (Figure 2.9) [52, 53].

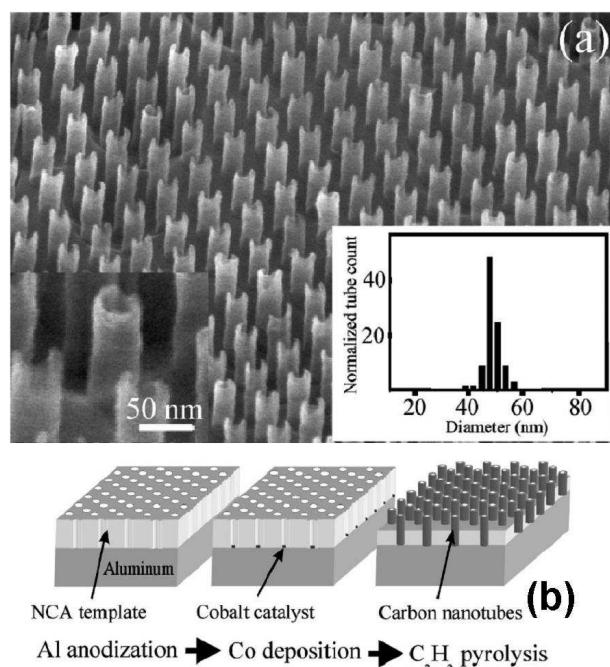


**Figure 2.9.** (a) SEM image showing tilted view of a highly ordered carbon nanotubes array grown in a nanoporous alumina template. The inset at the left is an enlarged view of the tubes. The inset at the right is a histogram of the nanotube diameter showing a narrow size distribution around 47 nm. (b) Schematic of fabrication process [52].

### 2.1.3 Field emission from carbon nanotubes

The interest in field emission and field emission devices has largely grown in the last decade due to prospects of the introduction of field emission electronics (i.e. displays and microwave tubes) and the development of new field emission materials, among which carbon nanotubes collected wide interest for their peculiar features. The covalent bonds between carbon atoms result in an activation energy for surface migration much larger than the one of the usual metallic emitter materials (W and Mo tips, for example). Electromigration is indeed the main reason of the fast degradation of the conventional metal sources. On the contrary, the CNT tip can withstand the extremely strong fields (several V/nm) required for field emission. CNTs can sustain large current density and exhibit a large aspect ratio and a good conductance [28]. They are also chemically inert and react only under extreme conditions or at high temperature with oxygen or hydrogen. Therefore, they are promising for working at relative low vacuum, allowing a wider usage in commercial applications. Displays (Figure 2.10) [54] and lighting elements [55]

employing CNT-based field emitters were firstly presented. Cathode-ray lamps [56], X-ray-tube sources [57], electron sources for high-resolution electron-beam instruments such as electron-beam lithography machines and electron microscopes [58] are currently investigated.

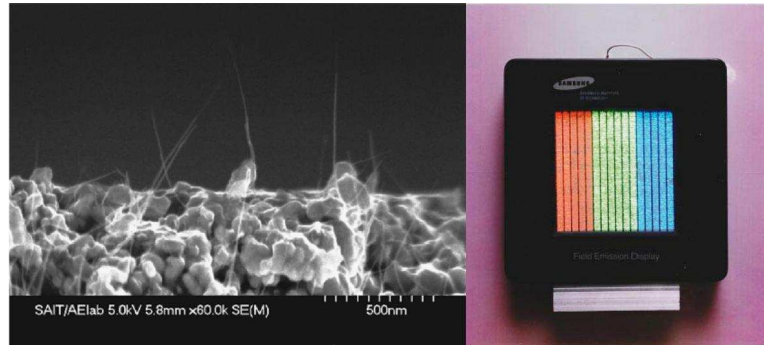


**Figure 2.10.** Carbon nanotubes field emitters display, developed by Samsung (right). SEM cross-section of the carbon nanotubes, grown by means of the arc-discharge method and then dispersed on the metal electrode (left) [54].

Electron sources can be fabricated by means of CNT-based devices in two different configurations. The first one employs a single CNT emitter and it is used in applications where a highly coherent electron beam is required, for example in electron microscopy. It generally involves the mounting on a metal support of a single CNT, synthesized by arc-discharge or laser ablation methods [58].

The second setup utilizes a CNTs emitters array. It is generally employed in flat-panel displays and it needs post-growth techniques, such as the dispersion of CNT-containing suspensions or the application of CNT-containing epoxy matrix on a support [54, 56]. A common drawback of this simple technique is that the obtained cathode morphology can not be controlled. On the contrary in an ideal field emission device all emitters should have exactly the same dimensions (height, diameter and spacing). For this reason, a direct synthesis of CNTs on patterned supports by means of the CVD method is deeply investigated. The density of the emitters and their diameters can be controlled by tuning the amount of the catalyst delivered to the substrate and the catalyst nanoparticles dimension respectively [59]. Obviously, the interpretation of the field emission experimental data is largely more problematic for a CNT-based emitter array with respect to a single CNT emitter device.

Field emission consists of a tunnelling current through a potential barrier between a metal surface and vacuum. It is theoretically described by the Fowler–Nordheim (FN) equation [58, 60] which relates locally defined quantities such as the electric field  $E$  applied to the emitter and the emitted current density  $J$ . That is,

$$J(E) = \frac{AE^2}{\phi} e^{-\frac{B\phi^{3/2}}{E}} \quad (2.1)$$

where  $A = 1.54 \cdot 10^{-6} \text{ A eV V}^{-2}$ ,  $B = 6.83 \cdot 10^9 \text{ eV}^{-3/2} \text{ V m}^{-1}$  and  $\phi$  is the work function of the emitter. It has to be noted that the equation holds exactly only for 0 K, but it was demonstrated to be also valid up to several hundred degrees Celsius. At higher temperature (above 1000 K) other mechanisms are also involved in electron emission, that is to say Schottky emission and thermionic emission [58]. In a so-called Fowler-Nordheim plot, where  $\ln\left(\frac{J}{E^2}\right)$  is plotted against  $\frac{1}{E}$ , the field emission behaviour is represented by a straight line.

The local electric field  $E$  at the emitter surface has to be around 2 – 3 kV/ $\mu\text{m}$  for activating the field emission phenomenon. On a tip surface, the local field  $E$  results larger than the applied macroscopic external field  $E_{EXT}$ . For emitters supported on a flat surface their relationship can be expressed as

$$E = \beta E_{EXT} = \beta \frac{V}{d} \quad (2.2)$$

where  $d$  is the inter-electrodes distance,  $V$  the applied voltage and  $\beta$  the field enhancement factor. Different expressions are reported for the field enhancement factor, which is a function of the geometrical features of the emitter. Approximately,  $\beta$  can be evaluated as  $\beta \approx \frac{h}{r}$  [59], where  $h$  and  $r$  are the height and radius of the emitter, respectively. More complex formulas exist that take into account also the influence of the counter electrode, particularly of the inter-electrodes distance  $d$  [61]. These theoretical models hold for a hemisphere on a cylinder, but in actual emitters this configuration is commonly missed. For CNTs in particular, the tip can be tapered, flat, opened or can also have some protrusions. These differences can produce an increase in the  $\beta$  value up to a factor two, which can easily lead to a factor of 10 increasing in the emitted current. For emitter arrays, another effect that has been proved to alter the theoretical value of the field enhancement factor is the emitter density. An electrostatic screening effect occurs if the emitters are too closely packed, resulting in a decrease of  $\beta$ . Since for field emission device a high total current is usually required, the emitter density can not be too low. The optimum density corresponds to a spacing between emitters twice the emitters height (Figure 2.11) [59, 62]. It is worth noting that the effective number of emitting site is lower than the film density. Typically, the CNTs density in a film is approximately  $10^8$ – $10^9 \text{ cm}^{-2}$ , whereas emitter densities of  $10^3$ – $10^4 \text{ cm}^{-2}$  have been reported. However, other measurements resulted in the

higher value of  $10^7$ – $10^8$   $\text{cm}^{-2}$  [63]. Together with density, also CNT orientation on the film affects the emission.

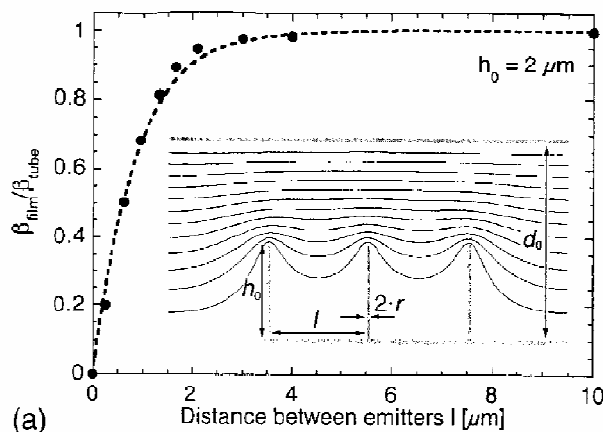


**Figure 2.11.** The field enhancement factor of a film of emitters is reduced by the reciprocal screening effect of the emitters. The optimum solution is achieved for a distance between the emitters,  $l$ , twice the height of the single emitter,  $h_0$  [59].

In order to characterize different field emission devices the commonly adopted figure-of-merit is the macroscopic electric field required for extracting some reference current densities. A “threshold field” is defined as the applied field required for extracting  $10 \text{ mA/cm}^2$ , which is the current density necessary to activate a phosphor pixel. A “turn-on field” is achieved when the current density is  $10 \mu\text{A/cm}^2$ . This figure-of-merit has some drawbacks, but is nevertheless the most commonly used in comparing different devices. Indeed, it has to be stressed that such an approach forces to interpret the field enhancement factor  $\beta$  as a parameter which characterizes the entire device, being a mean value if many tips compose the cathode.

Threshold and turn-on fields as low as  $1 \text{ V}/\mu\text{m}$  and  $5 \text{ V}/\mu\text{m}$  respectively have been reported for CNT films [63]. As a reference, hot cathode field emitters, based on Mo or W tips in gated configuration, commonly work at  $50$ – $100 \text{ V}/\mu\text{m}$  (Table 2.1). Nanotube films are able of emitting current densities up to a few  $\text{A/cm}^2$  at field below  $10 \text{ V}/\mu\text{m}$ . Single CNT can withstand an emission current up to  $0.2 \text{ mA}$ . Another relevant feature of the CNT emitters is the narrow energy spread of  $0.2$ – $0.3 \text{ eV}$  of the emitted electron beam. This is particularly critical in applications to electron sources where the beam has to be focused in a fine spot, as in electron microscopes and electron beam lithography machines, since this limits chromatic aberrations [58].

| <b>Table 2.1</b>              |   |
|-------------------------------|---|
| <i>Material</i>               | <i>Threshold electrical field (V/<math>\mu</math>m)</i> |
| Mo-W tips                     | 50 – 100  |
| Si tips                       | 50 – 100  |
| Undoped, defective diamond    | 30 – 120  |
| Amorphous diamond             | 20 – 40   |
| Graphite powder (< 1 mm size) | 17  |
| Nanostructured diamond        | 3 – 5   |
| Carbon Nanotubes (SWNT films) | 1 – 3 (stable at 1 A/cm <sup>2</sup> )                  |

**Table 2.1.** Comparison between different materials as field emitters. The threshold electrical field is defined as the electrical field required for the extraction of a 10 mA/cm<sup>2</sup> current density [25].

The exponential dependence of the emitted current by the electric field makes the field emission phenomenon much unstable, being characterized by step-like fluctuations, especially at low emitted currents [64]. In fact, even small variations in the field result in huge difference in the emitted current. A variability of less than 2.5 % in the electric field distribution can cause current fluctuations of 80 %. Possible causes of such variations can be the presence on the CNT surface of adsorbated molecules (probably water) that enhance the emission [65], but that can be desorbed when the CNT temperature grows above a threshold due to Joule effect. The presence of such adsorbates can also affect the actual emitter work function. Another drawback of this exponential relationship exists. The emission current is dominated by few CNTs, whose geometrical features give them a larger field enhancement factor. Most of the current passes through few CNTs, whose lifetime results shortened. This gives rise to fluctuations in the emitted current, consisting in large current jumps. Several ways have been proposed to reduce current fluctuations. An initial cleaning of the CNT emitter by means of a thermal heating up to 1000 K in ultra-high vacuum [65], to remove adsorbates and impurities, has been reported. The stability results largely increased if the temperature is maintained at 600–900 K during the emission, so that the molecules desorption continues. Another method involves a thermal heating, induced by Joule effect obtained forcing a current emission of over 1  $\mu$ A for several minutes [66]. This approach requires long CNTs and a good electrical contact of the CNTs with the substrate.

The interpretation of the field emission phenomenon is further complicated by the different experimental setup (i.e. planar or spherical tip anodes, different inter-electrodes distances...). Moreover, some incompatibilities in experimental results arise from different experimental objectives. Some authors are interested in physical insights of field emission, some others in practical applications. Zhirnov and colleagues [67] clearly stressed the

necessity of a “standardization” of the field emission measurements. This is a general necessity for field emission devices of every kind, not only for CNT-based ones.

The main cause of problems with the interpretation of field emission results comes from a misleading application of the Fowler–Nordheim (FN) equation (2.1). This equation links physical quantities that are locally defined. Nevertheless, an adapted equation which involves the physical quantities experimentally measurable, that is to say the total collected current  $I$  and the externally applied voltage  $V$ , is commonly adopted. That is,

$$I(V) = aV^2 e^{\frac{b}{V}} \quad (2.3)$$

These quantities are the ones technologically interesting, but they are not suitable for directly verifying if the current emission is controlled by the field emission mechanism rather than by other mechanisms such as thermo-ionic emission or internal secondary emission [58].

Experimental results are commonly interpreted by using equation (2.3) and a link to the FN equation (2.1) is established by converting  $I$  to  $J$  and  $V$  to  $E$  by linear factors:

$$J = \frac{I}{S} \quad (2.4)$$

$$E = \beta \frac{V}{d} \quad (2.5)$$

where  $S$  is the emission area,  $d$  is the “planar” anode to planar cathode distance.

The current density is the main physical quantity involved in comparing different devices, and so the evaluation of the parameter  $S$  is very important. As illustrated in Figure 2.12, which refers to the case of a single emitter device, different definitions of the “emission area”  $S$  can be given, which strongly affect the derived value of  $J$ .

A first approach consists in extracting the emission area from the intercept of the FN plot. Typically, this method gives a value for the effective area size of  $S_{FN}$  (the subscript refers to the FN plot, which is used for the estimation) about 1 – 10 % of the physical tip radius in the range 10 – 100 nm [67]. The relation between  $S_{FN}$  and the actual emission site is still debated, but it is clear that such small values always result in large current density. Another possibility is to use the physical area of the emitting tip, which also results in high current density. Since such approach can be hardly useful to characterize actual devices, better definitions are linked to the cathode geometry. The emission areas practically useful are the emission site area (and the emission site density) and the total cathode area (independent of the number of emission sites). The figure-of-

merit for device applications is the integral current density, i.e. the total current emitted divided by the entire cathode area. It is worth noting that these problems exist both for single-tip and for multi-tips devices, if one scales the problem to the number of emitters.

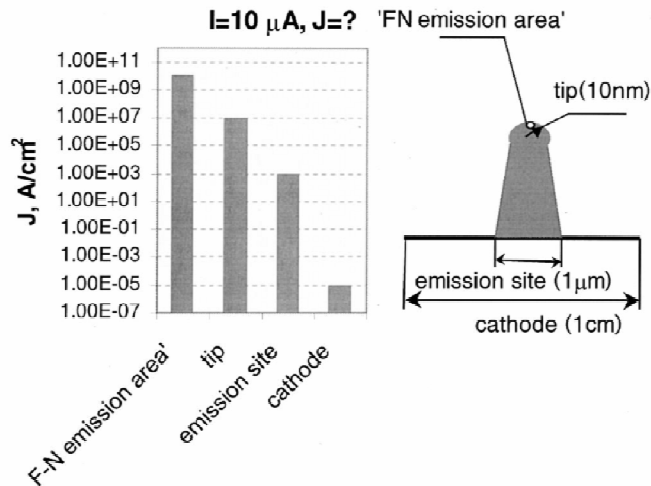


**Figure 2.12.** For the same emitted current, the evaluation of the current density of the field emitter strongly depends on the adopted definition of the emitting area [67].

These considerations have to be applied to the different experimental setups. A plane-to-plane capacitor is a common configuration, where both the electrodes are macroscopic with respect to the emitter sites and the inter-electrodes separation. The main disadvantage of this setup comes from the possible misalignment between the two electrodes, resulting in electric field non-uniformity. Another experimental setup is the sphere-to-plane configuration, where the anode is described as a macroscopic spherical electrode. Misalignments here do not reflect in inaccuracy in the gap distance evaluation. However, it is not simple to estimate the effective emission area because it depends on the anode-to-cathode distance. Other configurations have also been used in literature.

With regards to the stability of the CNT field emitters, the lifetime of individual CNT is long, up to several hundred hours. An emission current of  $10 \text{ mA/cm}^2$  was maintained for 8000 hours requiring only an 11 % increase of the applied field [56]. The failure mechanisms are not fully understood so far. High currents are mainly supposed to limit the CNT emitter lifetime. A gradual decrease in field enhancement factor has been observed due to field evaporation of a SWNT beyond  $300 \text{ nA}$ – $1 \mu A$ , and to damaging of the tube walls of a MWNT. MWNTs can sustain current up to  $10 \mu A$ , but above  $1 \mu A$  the emission is unstable and the lifetime reduced [58]. Abrupt failures have been also reported, supposedly due to mechanical failure caused by resistive heating at the contact or by tensile loading of the emitter under the applied electric field [58, 68]. A sudden failure

mechanism is also arcing, i.e. an arc between the anode and the cathode that is initiated by field emission [69]. Such events can be caused by high field emission current, anode out-gassing or local evaporation of cathode material that create a conducting channel between the electrodes.

## 2.2 Anodic aluminium oxide

One of the key nanotechnologies for the detector development is the fabrication of an insulating template that has a high regularity and submicron porous structure. The template has also to allow the growth, inside its nanochannels, of 1-D nanoconductors, being carbon nanotubes or metal nanowires. Template synthesis of nanostructures, such as nanodots or nanowires, has been widely investigated since it is a simple, high-throughput and cheap alternative to the electron beam lithography technique. Moreover, template driven synthesis allows a highly uniform growth of structures with similar dimensions. Its main drawback is that the produced nanostructures are often polycrystalline.

Many template materials exist. For instance, polymer films containing track-etched channels can be used. This technique involves a polymer film which is irradiated by means of heavy-ions to generate damaged spots in the surface of the film. A subsequent chemical etching amplifies these spots generating uniform and cylindrical pores through the film [71]. However, pores obtained with this method are often randomly distributed over the surface. On another side, mesoporous materials, which contains channels much smaller (1.5 – 30 nm in diameter), are not suitable for the growth of high aspect ratio 1-dimensional nanostructures, such the one required in the NanoChanT project.

Anodic Aluminium Oxide (AAO), or alumina, presents a self organized structure which can achieve, under particular synthesis conditions, a high level of regularity that makes it a proper choice for many applications. Alumina presents also insulating properties [70]. Many materials have been employed in the alumina template driven synthesis, such as metals, semiconductors, ceramics and organic polymers [21]. Also the synthesis of CNTs has been reported inside the alumina nanochannels [16, 52]. Therefore, the anodic aluminium oxide fulfils all constraints imposed by the project.

### 2.2.1 *General properties*

Oxidation is the reaction of a material with oxygen, with subsequent formation of an oxygen-compound, or oxide. The way in which a metal oxidizes can be influenced by changing the reaction environment. Normally, at air exposure a thin layer of oxide forms. This layer separates the deeper metal from the environment and prevents the oxidation from continuing. A thicker oxide layer can be obtained by using different processes, as the anodic oxidation.

Anodic oxidation, or anodization, of aluminium consists in submerging the aluminium in a solution containing ionic oxygen-compounds, i.e. an acid, and applying a voltage between the aluminium and a counter electrode. The aluminium is used as anode,

hence the name anodization. The resulting product is called Anodic Aluminium Oxide (AAO), or alumina.

Anodic aluminium oxide coatings can be classified according to whether or not the electrolyte applies appreciable solvent action on the oxide. Three situations can be distinguished [72].

When acids with weak etching activity are used, the formed oxides will be dissolved very slowly. Initially, high current flows in the system and oxide is formed rapidly, but after a relatively short time, current flow decreases to a relatively low steady value, and the coating is completely formed. The oxide layer will be a thin non-porous layer, whose thickness depends linearly on the applied voltage, with a rate of approximately 1.4 nm/V. The formed oxide layer acts as a protective wall between the acid and the remaining aluminium. Boric acid is a possible electrolyte for this kind of anodic oxidation.

The reverse situation will occur when a highly-aggressive acid is used. In this case the acid etches the oxide away about as fast as it is created by the oxidation reaction. The final product will be a very thin layer of oxide. Such a procedure tends to even out the irregularities of the starting aluminium surface and thus produces a bright highly reflective surface. This polishing of the surface, usually referred as electropolishing, is commonly carried out as a pre-treatment of the aluminium samples before the anodization process. Fluoboric acid can be used in this case.

The third situation is the one of interest for template applications. Making use of moderately strong acids, as oxalic, phosphoric or sulphuric acid, a porous oxide growth occurs.

Submitting aluminium to porous oxidation results in a layer of aluminium oxide whose geometry can be schematically represented as a honeycomb structure, characterized by a close-packed array of columnar hexagonal cells, each containing a central pore normal to the surface (Figure 2.13). These pores propagate downwards as long as the anodization is continued. Between the pores and the remaining aluminium a “barrier layer” of non-porous aluminium oxide exists. The thickness of this layer is thin enough to let current pass and let the process continue. Meanwhile, the layer is also etched away from the above so that the pores can grow deeper and deeper into the aluminium. Eventually all the aluminium can be oxidized. The resulting array of pores can achieve high aspect ratio: typical values are 50 nm for the diameter and 50  $\mu\text{m}$  for the length (but thicknesses up to 100 – 200  $\mu\text{m}$  have been produced [73]), which yield an aspect ratio of  $10^3$ . Densities from  $10^9$  to  $10^{11}$  pores/ $\text{cm}^2$  can be controllably achieved varying the anodization conditions. Often the pattern consists of several areas of high regularity separated by borders, where the pattern direction changes abruptly. The sizes of these areas are of the order of magnitude of microns. The pores are cylindrical in shape with a scalloped bottom. The barrier layer follows this spherical shape too, having a scalloped base also at the side of the aluminium.

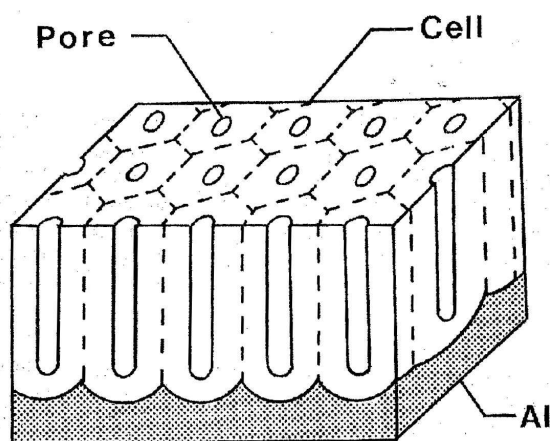


**Figure 2.13.** Schematic model of ideal porous structure of anodic alumina [81].

### 2.2.2 Porous growth

The growth process of the porous aluminium can be divided in four stages, which can be followed monitoring the time evolution of current (or voltage) in a potentiostatic condition (or respectively, galvanostatic) [74]. These stages, referred to a condition of constant applied voltage, are schematically presented in Figure 2.14.

During the first stage a barrier oxide layer starts to grow, exactly as in the non-porous anodization with low potency acids. The current starts at a high value, because it passes easily through the metallic aluminium, but soon after it falls rapidly because of the oxide layer growth (stage I).

The second stage begins with the initiation of the pores. Many small pores start growing due to the etching action of the acid, randomly spread over the surface. The cracks into the oxide give the current the possibility of finding lower resistance paths and thus not falling to zero. The current density will be the highest through the pores, and consequently the oxidation and etching reactions are highest at the pore bottom, propagating the pores further into aluminium. This growth has been demonstrated to preferentially occur at metal grain boundaries or at the defects inside each crystalline grain [72, 75]. For obtaining pore regularity it is very important to have a high crystalline order of the starting aluminium layer, i.e. large grain sizes and as few defects as possible inside the grains (stage II).

The third stage consists of the pore selection process. Only some of the starting pores continue to grow through the oxide, assuming a pear-like shape, whereas the others remain small and are engulfed by their stronger neighbours. The pore density at the bottom of the aluminium oxide has been reported to be about 20 % lower than at the upper surface [76]. The pear-like shape can be explained by this pore engulfing, thus becoming broader on their way down, and secondly because of the local current increase along the lower resistance paths opened by the cracks in the oxide layer. During this pores selection process, the current raises because of the formation of a thin oxide layer (stage III).

Eventually, a steady state pore structure is reached. All the pores present in this stage grow downwards as long as the anodization process is continued. This honeycomb array achieves better regularity as the pore growth goes deeper [76]. The current remains stable, having reached a balance between the oxide creation and oxide dissolution (stage IV).

The four stages are not distinctly divided but gradually flow into each other. The timescale of the process depends on the anodizing conditions; generally speaking, the first phase takes just one or two seconds, the pore initiation and selection about fifteen minutes to half an hour and the steady state can be continued as long as desired.

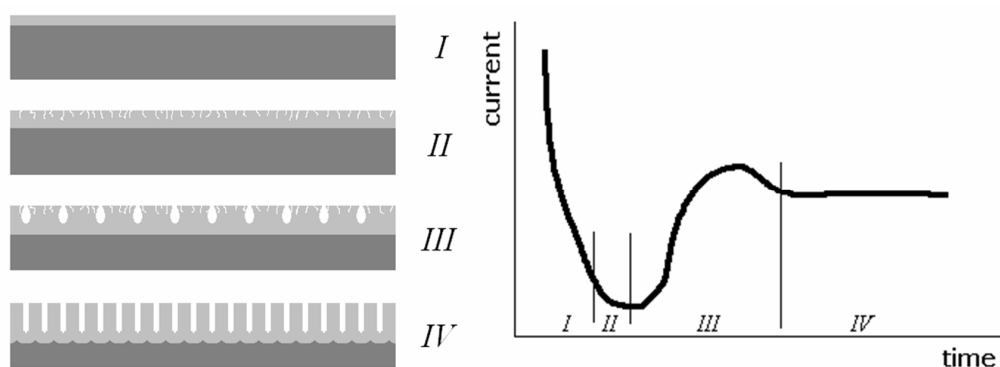


**Figure 2.14.** The evolution of the process of anodic oxidation followed on the sample (left) and on the current evolution (right). The four stages are described in the text.

The porous growth of aluminium oxide is therefore the result of two main reactions, one being the oxidation of aluminium and the other being the oxide dissolution. The complication of a porous structure formation results from particular initial conditions. These and the other reactions involved in the growth process are analysed in the following.

The oxidation of aluminium occurs by the reaction of  $\text{Al}^{3+}$  ions with  $\text{OH}^-$  ions, but also other reactions involving  $\text{O}^{2-}$  or acid oxyanions (for example  $\text{SO}_4^{2-}$  in the case of sulphuric acid) are possible. The  $\text{O}^{2-}$  and  $\text{OH}^-$  ions come from the water of the anodizing solution. Traces of water have been reported as necessary for anodizing in non-aqueous solution. The relative occurrence of the different reactions depends on the relative ease of discharge of ions under local conditions and upon the charge and size of the ions [75].

Because of the applied voltage, these anions can migrate through the oxide layer to the aluminium where they meet  $\text{Al}^{3+}$  ions to create the  $\text{Al}_2\text{O}_3$ . Meanwhile,  $\text{Al}^{3+}$  ions drift from the metal to the solution. The oxide layer thickness is proportional to the applied voltage, with a rate limited by the value corresponding to the non-porous growth, i.e. about 1.4 nm/V. That is because higher voltages result in ions with higher energies, which can

cross greater distances through the oxide [72]. The oxidation will be stronger at the places where the resistance is lower and the current density higher.

Generally speaking, it could be possible to have oxide growth at both the electrolyte-oxide interface and the oxide-metal one. This situation normally occurs in the case of a non-porous growth. However, it has been shown that a mandatory condition for the porous growth is that the oxide growth at the electrolyte interface does not occur. Actually, during the porous anodization process  $\text{Al}^{3+}$  ions are directly ejected into the solution under the action of the electric field. This direct loss of  $\text{Al}^{3+}$  ions is related to a non-uniform thickening of the initial oxide barrier layer, which eventually results in pore initiation. Because of the cations loss, the volume of the oxide formed at the metal-oxide interface results to be smaller than the volume of the metal consumed. This forces the oxide barrier layer to thicken under tensile stresses and to be unstable with respect to perturbations. Local cracking of the film consequently occurs during the first stages of the oxide growth, preferentially located at surface defects or pre-existing metal ridges [77]. Also the effect of field-enhanced chemical dissolution is strongly considered as a cause of the initial local cracks. Actually, when a moderately strong acid is used, the solvent action of the acid solution is not active over the entire surface, but it is preferentially located at aluminium grain boundaries or at defects inside the grain of the pure metal [72].

Whichever the mechanism these local cracks are formed by, they act as “nuclei” for the pore formation, since a healing mechanism results in local thickening of the damaged oxide, according to the oxide kinetic growth. The barrier layer is forced to be of uniform thickness in a direction perpendicular to the local film surface, where the current for film formation flows. This local film surface results to be the oxide-electrolyte interface, as no oxide is formed there. The local geometries of the metal-oxide interface are consequently determined by those of the corresponding oxide-electrolyte interface [77].

After the pore initiation, the dissolution of the oxide is preferentially located at the pore bottom, resulting in the pore formation and steady state growth. Initially the dissolution was supposed to be mainly due to chemical etching. The self promoting pore growth was explained by a higher temperature at the pore bottom which promotes higher etching rates [72]. Following experiments proved that local Joule heating can not be the major factor in pore formation. On the contrary, dissolution, like oxidation, is strongly dependent on the electric field, being stronger in those places where the electric field is stronger, i.e. the pores [75, 74]. This hypothesis is confirmed by the fact that changing the voltage critically influences the speed of oxide etching and that the pore walls are hardly attacked by the acid, since practically all the current flows through the pore bottoms. The contribution of the pure chemical etching at the dissolution process is therefore negligible. The steady growth of the pores is therefore largely determined by an equilibrium between film growth and film dissolution under the field at the pore base.

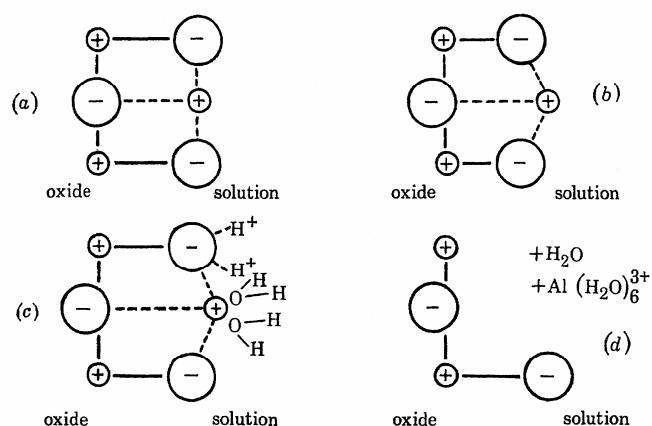


**Figure 2.15.** Model for the field-enhanced dissolution. For sake of simplicity the oxide has been represented as a simple cubic type. a) Normal situation of  $\text{Al}_2\text{O}_3$ . b) The applied electric field polarizes the oxide and weakens the electrical bonds between the atoms c) dissolution of  $\text{Al}^{3+}$  by water molecules through the activated complex and removal of  $\text{O}^{2-}$  by  $\text{H}_3\text{O}^+$  ions d) Remaining oxide and resulting solution.

A model for the  $\text{Al}_2\text{O}_3$  dissolution is presented in Figure 2.15, where the oxide is schematically represented with a simple cubic structure. The model involves the breaking of the Al–O bonds in the lattice, with the production of  $\text{Al}(\text{H}_2\text{O})_6^{3+}$  ions and probably  $\text{H}_2\text{O}$ . Any process that can weaken the Al–O bonds in the oxide promotes the dissolution at the kink sites by lowering the effective activation energy for this process. In this, two processes are acting: hydrogen bonding at the outer region of barrier layer and, much more important, polarization by electric field [75]. The Al–O bonds increase in length at the barrier layer surface because of the field, which pulls the  $\text{O}^{2-}$  ions into the oxide and pushes the  $\text{Al}^{3+}$  ions into solution. Solvation of  $\text{Al}^{3+}$  ions by water molecules, via the activated complex, and the removal of  $\text{O}^{2-}$  ions by  $\text{H}_3\text{O}^+$  ions, producing water, are thus greatly facilitated. The oxide dissolution is therefore stronger where the electric field is stronger. The model explains also the already mentioned necessity of, at least, traces of water in the electrolyte solution for the dissolution process.

Another important reaction active during oxide formation is the incorporation of some anionic impurities, which can deeply influence the structural and electrical properties of the resulting oxide [78, 75]. The oxide consists mainly of microcrystalline material, but all around the pores is amorphous and contains higher concentrations of water, hydroxyl groups and acid anions. It has been reported that anions incorporation inside the film depends on the type of acid used in the anodization process.

The reason why the self-organized growth of nanoporous oxide results in a honeycomb structure of hexagonal patterns is still not completely understood. A model by Keller et al. [72] proposes a geometrical explanation, based on arguments of symmetry. The growth of an individual pore is a cylindrically symmetrical process. The pore is

surrounded by an oxide layer of a certain thickness depending, as already stated, on the applied voltage. Both the barrier layer and the side walls can not be thicker than this limit. The aluminium surface will be filled with many pores, at such a distance that all aluminium will be oxidized. Pores at a greater distance from each other than the possible oxide thickness, would still have some aluminium left between them. But this cannot be the case since new pores will develop in the layer of oxide on top of the aluminium between the pores. Thus the entire aluminium surface will be oxidized and filled with pores, while the structure evolves to reach the ideal cylindrical symmetry of the individual pore. The resulting hexagonal pattern is the regular pattern closest to the ideal structure.

### 2.2.3 *Process parameters*

Besides the general growth process, the actual characteristics of the anodic aluminium oxide are dependent on the parameters under which the anodization occurs. Pore diameter, cell size and array regularity are properties to be optimized on the base of the final application requirements.

The duration of the anodization process affects both the thickness and the regularity of the aluminium oxide. Indeed, the latter improves with a deeper growth. The oxide growth rate depends on different process parameters, but will normally be of the order of magnitude of microns per hour. The initial pore nucleation is random over the surface, and only when the pores grow downward a better regularity, more similar to the ideal hexagonal distribution, is reached [76]. A perfect order cannot be achieved: the structure consists of “defect-free” neighbouring domains, few microns in size and with different lattice orientation, separated by grain boundaries [72, 79]. However, the size of these areas grows with time [80] to a certain order.

The voltage is the most influent parameter on the anodization process: cell size, pore diameter, barrier layer thickness and also regularity of the array depend on it. Thicker oxide barrier layer can be created at higher voltage because of higher ions energies. This thickness is directly related to the other geometrical parameters, such as the wall thickness. The dependence of oxide thickness on voltage for the barrier layer is about 1 nm/V, while for the pore wall is a bit less, about 0.7 nm/V, since the electric field is stronger at the pore bottom due to the curvature radius [75, 72]. These proportionality factors slightly depend also on other anodizing parameters, such as electrolyte composition and process temperature. It has been found that also the pore diameter is directly proportional to the applied voltage, but the factor of proportionality, reported to be 1.29 nm/V, is not well established since many other parameters, such as oxide etching conditions, have to be taken into account [75]. The cell size is the sum of pore diameter and of the oxide thickness between two pores, i.e. the total thickness of two pore walls, so it is itself linearly dependent on voltage.

As a result, the oxide porosity is a characteristic independent on the voltage. As both the amount of oxide and the amount of pores per  $\text{cm}^2$  linearly depend on the voltage, their relative values will not change [75]. Porosity values of about 10% are usually reported [73].

Voltage has a deep influence on the pore array regularity, related to the kind of acid used. Ordered porous growth occurs only in particular voltage conditions, strongly dependent on the type of electrolyte used, i.e. on the type of acid. Only certain acids result in porous growth of the oxide. Oxalic, sulphuric and phosphoric acids are often used, but experiments with chromic, glycolic, tartaric and others are also reported in literature. Depending on the kind of electrolyte, a specific anodization voltage range exists for optimizing the self-ordering process (Table 2.2). Little or no ordering is observed without fulfilling this condition [79-82]. The choice of different acid type has consequently a large influence on both the cell size and the pore diameter. As a particular acid requires a certain anodizing voltage, the geometrical features of the porous oxide are also fixed. In fact, the changing in chemical properties causes different etching of the oxide at the electrolyte interface, so changing the barrier layer thickness and the pore diameters. Cell size results larger for milder electrolyte. Between the most commonly used acids, the larger pores and cell sizes are created with phosphoric acid, followed by chromic, oxalic and sulphuric acid [72, 79]. No differences in pattern regularity have been reported with respect to different acids, when working at the proper voltage. A clear explanation of the relation between the type of acid and the applied voltage needed for a regular pattern formation is still missing in the literature, even if the ions migration mechanism inside the oxide is generally thought to be related to the issue.

| <b>Table 2.2</b>          |                      |   |                       |                  |
|---------------------------|----------------------|---|-----------------------|------------------|
| <i>Electrolyte (acid)</i> | <i>Concentration</i> | <i>Voltage range per regularity (V)</i> | <i>Cell size (nm)</i> | <i>Reference</i> |
| Sulphuric                 | 0.3 M                | 20 – 25                                 | 60                    | [79]             |
| Oxalic                    | 0.3 M                | 40 – 50                                 | 90 – 100              | [79]             |
| Phosphoric                | 0.3 M                | 160 – 195                               | 420 - 500             | [79, 82]         |

**Table 2.2.** Condition on the anodization voltage for obtaining a highly regular alumina template, using different electrolyte solution. Values are only indicative, as many other parameters (temperature, pre-processing steps...) affect the anodization process.

Related to the different acids is also the oxide formation speed. The different rate of spread of pores depends on the dissolving ability of the electrolyte under the field [75]. The composition of the oxide seems to be strongly dependent on the formation speed. The oxide consists of microcrystalline, pure oxide areas and more amorphous, contaminated areas. Anion contamination has been reported to be larger when the formation rate is faster. The fastest and consequently most contaminated growth results when using sulphuric acid, and then the growth rate and contamination decrease for oxalic, phosphoric and chromic acid [78].

Other parameters such as temperature and concentration of the acid in the solution seem to have only minor influence on the process, with respect to the previous ones [75, 81]. Lower pH values produce thinner barrier layer and have only little influence on the pore diameters. Higher temperatures result in stronger chemical etching of the acid and thus in thinner barrier layer and larger pore diameters [75]. A more evident effect of the temperature increase can be found at the aluminium oxide surface, where the oxide dissolution is only a chemical process and not a field-enhanced one.

The porous anodization is very much affected by perturbations in the process, so lower growth rates, i.e. long interaction times for self organizing process, are preferable for achieving a better structure regularity. Furthermore, experimental conditions favourable for the self ordering process should be maintained over long anodization times. Therefore, parameters which lead to strongly time-dependent etching conditions are not suitable for the formation of ordered structures. Low process temperatures and proper voltages are thus usually chosen to avoid high etching rates [76, 81].

The regularity of the honeycomb structure is related with the existence of a smooth etching front and with the absence of defects over the surface. For this reason proper preliminary treatments of the aluminium are mandatory.

For increasing the aluminium grain size, and thus enlarging the areas of lattice regularity, an annealing is often performed for some hours at about 500 °C in nitrogen atmosphere to smooth aluminium foils and obtain grain sizes in the 100 µm range. However, the ordered domains in the hexagonal pattern are also related to the dislocation defects distributed over the surface inside the grain boundaries [76], so that ordered areas larger than 5 µm are not achievable without taking different approaches.

A more effective treatment is the electropolishing of the aluminium sample. Pores tend to be created more easily at irregularities, as already seen. The surface roughness is reduced to some tens of nanometres by polishing, resulting in a different evolution of the anodization process with respect to the non-polished sample. The high surface roughness leads to a faster formation of the barrier oxide and pores at depressions of the surface than at other locations. The pores that nucleated at the early stage will grow in front of the others, so that the surface roughness is transferred to the etching front at the metal-oxide interface, preventing self organization in a regular honeycomb structure [76].

Moreover, stirring of the solution during the anodization is mandatory for obtaining ordered structures. It is necessary to keep a spatially constant temperature throughout the liquid, preventing localized temperature increases and bubbles formation that can alter the stability of the process and consequently the structure regularity [76, 82]. Stirring is also important in maintaining stable the electrolyte concentration at pore bottom. The hydrated aluminium ions, product of the dissolution reaction of the oxide at the pore bottom, move through the solution by diffusion, so their concentration results to be high at the pore mouth if the solution is not stirred. The concentration gradient inside the pore is thus lower and a higher equilibrium concentration at the pore bottom results with respect to the stirred solution case [76].

An interesting observation has been recently made about a condition for obtaining an ordered pore pattern in different anodization processes. Although the oxidation parameters, such as voltage, temperature, electrolyte and concentration, can be quite different, the volume expansion ratio, i.e. the ratio between the volume of the final aluminium oxide and the volume of the starting metallic aluminium, has to be very close to 1.4 in order to obtain ordered pore arrangements. On the contrary, with volume contraction or very strong expansion, no ordered structures can be formed [79]. When aluminium is oxidized, the volume expands roughly of a factor of 2, since the atomic density of aluminium in aluminium oxide is a factor of 2 lower than in metallic aluminium. A volume expansion ratio of 1.4 corresponds to a moderate expansion of aluminium during oxide growth, which is related to a particular condition on the loss of  $\text{Al}^{3+}$  ions in solution during the anodization. It is thus suggested that the mechanical stress associated to a moderate volume expansion during oxide growth is the cause of the repulsive forces between neighbour pores that lead to the self organized formation of hexagonal pore arrays [73].

Two modifications at the process have been developed by Masuda with the intention of enhancing the template regularity. A first method consists in employing a mechanical molding process [83]. A master of hexagonally arranged array of SiC convex shapes is fabricated by means of electron beam lithography. The master, when pressed on the aluminium layer, creates a concave shapes texture on the surface that acts as initiation points during the subsequent anodization. The final pore pattern regularity result strongly enhanced. The second method is more viable as it does not require the availability of the expensive electron beam lithography facility. It consists of a two-step anodization process [84]. The basic idea is the same than the previous one, but now the indentation on the aluminium surface is produced by means of an anodization and an aluminium oxide removal. The first anodization generally produces a pore pattern that is strongly affected by the regularity of the starting surface. Higher order levels are achieved as the pores grow deeper. A complete removal of the alumina layer produced by the first anodization thus results in a textured surface with an improved regularity with respect to the starting situation (Figure 2.16).

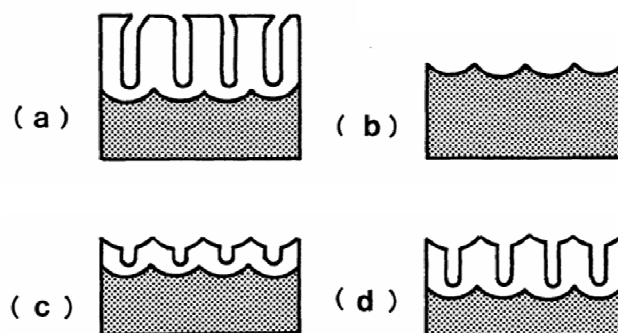


**Figure 2.16.** Schematic for the fabrication of an alumina sample by means of the two-step anodization process: (a) porous alumina after first anodization; (b) removal of the porous alumina layer; (c) initiation of hole formation in second anodizing; (d) porous alumina after second anodization [84].

#### 2.2.4 Templated synthesis of nanowires

Nanowires have been widely investigated over the last decades since their nanometric dimension gives them peculiar properties considerably different with respect to those of the corresponding bulk materials. Many reviews report on the peculiar features of such structures and their potential and present applications, especially in nanoelectronic and optoelectronic devices [21, 22]. Many materials have been successfully synthesized with nanowires shape. Metal, oxides and semiconductor 1-dimensional objects have been created by means of different methods, from catalyst-driven syntheses to templated ones. In particular, the latter method allows producing nanowires with similar dimensions. Porous anodic alumina is one of the most commonly employed templates for such a fabrication.

Different methods are reported in the literature to deposit a material inside the pores of aluminium oxide template [21]. The electrochemical deposition, both at direct and alternate current, is by far the most popular method [85, 86]. It consists in applying a voltage between the sample back-contact and a counter electrode, while the liquid electrolyte contains the ions of the metal to be deposited. Both direct and alternate voltage can be used, depending on the presence of a direct contact between the metal back-contact and the electrolyte (Figure 2.17). During deposition, the positive ions will travel to the negatively charged back contact and precipitate. If an isolating barrier layer exists, an AC deposition is needed. The barrier layer acts as a capacitor which allows a current to pass if a sufficiently high frequency is applied.

The voltage has to be high enough to enable the electrons needed for recombination to overcome the barrier layer. A proper voltage has to be at least 0.4 times the voltage employed during anodization [86]. Because anodic aluminium oxide conducts

preferentially in only one direction, the cathodic one (i.e. from the anode to the cathode), metal ions are reduced without being re-oxidized [87].

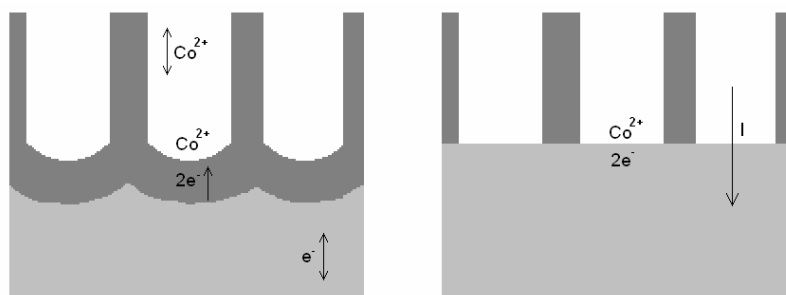


**Figure 2.17.** Electrochemical deposition with AC (left) and DC (right) processes. The DC process allows standard recombination at the cathodic interface. With the AC process all electrons and ions will change direction continually. Some electrons are able to overcome the oxide barrier layer and recombine with cobalt ions.

The electrolyte solution is generally composed by sulphates of the respective metals to be deposited:  $\text{NiSO}_4 \cdot 6 \text{H}_2\text{O}$ ,  $\text{FeSO}_4 \cdot 7 \text{H}_2\text{O}$ ,  $\text{CoSO}_4 \cdot 7 \text{H}_2\text{O}$ . Boric acid can be added to control the solution pH [88]. It is reported that metal deposition is easier for lower pH values [89]. Other components can be added depending on the different specific functions of the desired metal nanowires. In particular, for AC depositions also magnesium or aluminium ions have to be added in the solution in order to prevent the breakdown of the alumina barrier layer, thus allowing a longer deposition [85, 89]. The presence of  $\text{Mg}^{2+}$  ions is considered to strongly inhibit hydrogen evolution at the metal-oxide interface, which damages the barrier layer [90].

## **Chapter 3      Synthesis of free standing carbon nanotubes**

Carbon Nanotubes (CNTs) are the main topic of this thesis. Their peculiar characteristics have had a breakthrough impact over a wide area of applications. In particular they are able to sustain large current densities without being degraded. In fact, since their structure is very stable, they do not suffer electromigration, which conversely affects commonly used metal wires, bringing about their failure. In this sense, CNTs have catalyzed a large interest also for applications in nuclear and subnuclear physics.

In the NanoChanT project, they are employed as charge collectors between the active layer of the detector and the read-out electronics. They have to be electrically insulated from each other, in order to avoid any degradation in the spatial resolution gained by reducing the thickness of the silicon diode. They have been investigated together with metal nanowires for filling the nanoporous alumina because they seemed promising in a further development of the detector. CNTs could become themselves the active layer of the detector, since CNTs doping has already been reported in literature [13-15]. Their employment as nanometric diodes could enhance the detector spatial resolution as the charge produced by the ionizing radiation could be directly created in nano-sized areas. Furthermore, some researches indicated that CNTs can be used as transistor, allowing signal amplification extremely near to the charge creation [16].

Carbon nanotubes can be successfully employed also in other devices suitable for applications in High Energy Physics and electronics. In particular, they are very appealing due to their 1-dimensional shape and their chemical stability, which make them suitable for applications in field emission devices as stable cold electron sources.

In this chapter, the research on the catalytic assisted chemical vapour deposition (CVD) synthesis of CNTs in a free-standing configuration is reported. This investigation has been developed in order to achieve a better comprehension on some aspects related to the final accomplishment of the project. In Chapter 4, the investigation on CNTs confined structures is discussed.

Insulating substrates have been initially employed to gain some insights on the growth process. Furthermore, the CNT film on insulating substrates ( $\text{SiO}_2$  or  $\text{Si}_3\text{N}_4$ ) is also interesting for the development of a CNT-based gas sensor device. After the most appropriate parameters for the CVD process on these substrates have been inferred, the research has been focused on the synthesis of CNT films on conductive substrates. This step has been needed for defining the proper substrate, among those used in microelectronic technology and deliverable with the facilities of the IMM – CNR Institute, to allow electrical characterization of the synthesized CNTs. A simplified version of the detector, consisting of an unconfined CNT charge collector layer, has been designed and is under construction. This simplified arrangement will permit to test the collection through CNTs of the charge produced by a test radiation beam (such as  $\alpha$  particles) in the active layer, and thus to determine the actual thickness of the active silicon diode layer.

The definition of the most appropriate conductive layer has involved field emission characterizations of the free-standing CNT samples. These investigations not only allowed us to determine the actual conductive substrate but they also paved the way to some applications of the CNT samples as electron sources.

### 3.1 Deposition system and characterization facilities

#### 3.1.1 Chemical Vapour Deposition system

Carbon Nanotubes (CNTs) have been produced by means of a catalyst-assisted chemical vapour deposition (C-CVD) technique. The reaction system is located inside a class 100.000 (FED-STD-209D classification) clean room environment of the IMM – CNR Institute in Bologna.

The system consists of a hot wall tubular CVD chamber. A synoptic representation is shown in Figure 3.1. A quartz tube chamber, with a diameter of 4 cm, is inserted in a resistively heated furnace, which guarantees a uniform heating over a 6 cm long section. The maximum temperature achievable by the system is 1200 °C. A K-type thermocouple supervises the actual temperature in the hot zone of the furnace. The heater is controlled by means of a PID driver. The samples are located over a quartz sample holder to be inserted in the furnace. A maximum of four samples, with size  $2 \times 1 \text{ cm}^2$ , can be simultaneously loaded in the uniformly heated zone. Generally, the loading occurs at room temperature by means of a quartz bar. Consequently, substrates undergo not only the desired annealing step but also the heating ramp process. Different heating profiles can be designed, fixing up to 4 intermediate temperatures, the relative durations of the heating ramp and of the set temperature plateau. This solution permits to limit thermal overshoots, but it involves a long heating procedure, namely of 100 minutes. Otherwise, if a short heating process is

required, an uncontrolled ramp can be performed, but with larger thermal overshoots. For temperatures set in the range 700 – 900 °C, overshoots have a typical value of 100 °C and are usually recovered within 10 – 15 minutes. The total duration of this kind of heating ramp is 50 – 70 minutes, depending on the final temperature. For some applications, the heating process has to be kept as short and controlled as possible. In these cases, a different loading approach has been followed, which allows the movement of the sample holder also during the process. A short quartz bar is linked at the sample holder on one side and includes two ferromagnetic rods on the other side. Before starting the process, at room temperature, they are both inserted in the region of the quartz tube outside the heated zone. The quartz bar can be moved inside the tube driven by a magnet. In this way, the samples can be kept in the cold zone during the heating ramp and inserted in the hot zone of the tube once the deposition temperature has been reached. Usually, 5 minutes are required for the insertion and for the temperature stabilization.

A computer controlled gas system manages the flowing of the gases inside the tube. Available gases are carbon-containing ( $C_2H_2$  and  $CH_4$ ), reactive ( $H_2$  and  $NH_3$ ) and inert ( $N_2$  and Ar). Each gas line is driven by a dedicated mass flow controller. The gases are directly injected in the reaction chamber. The pressure in the chamber is usually maintained at 750 Torr. The system is also equipped with a pumping system, based on a rotary pump, that allows reaching a moderate vacuum (approximately  $10^{-2}$  Torr) to purge the chamber. By means of a needle valve regulation it is also possible to maintain a reduced intermediate range pressure during the CNT synthesis process.

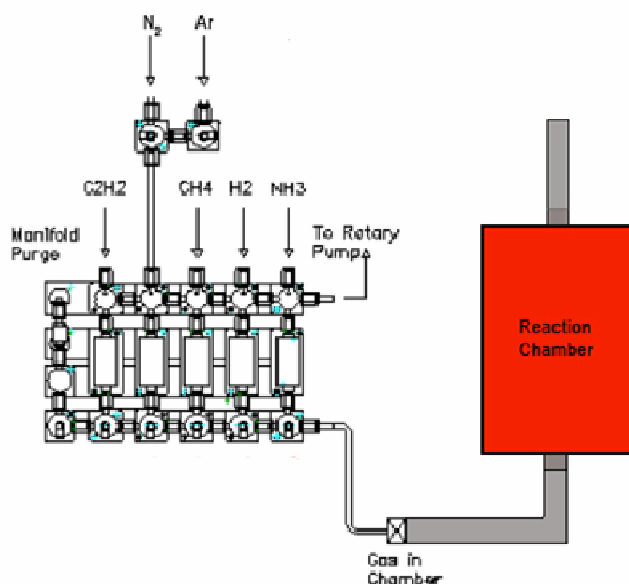


**Figure 3.1.** Synoptic representation of the CVD system of the IMM-CNR institute. On the left, the gas system is depicted, on the right the reaction chamber.

### 3.1.2 Characterization facilities

The quality and morphological features of CNT deposits have been characterized by means of Scanning Electron Microscopy (SEM), High-Resolution Transmission Electron Microscopy (HR-TEM) and Raman spectroscopy techniques. SEM observations have also been used for the investigations on the alumina template.

Electron microscopy techniques, as SEM and TEM, are based on the interaction of a high energy electron beam ( $> \text{keV}$ ) with a specimen. Many secondary signals are produced which can be analyzed and provide interesting information about the sample (Figure 3.2). In a scanning electron microscopy (SEM) the signals that usually can be analyzed are the secondary electrons (SE or InLens), backscattered electrons (BSE or RBSD) and characteristic X-rays (EDX). If the sample is thin enough the elastically scattered electrons can be investigated in a transmission electron microscopy (TEM).

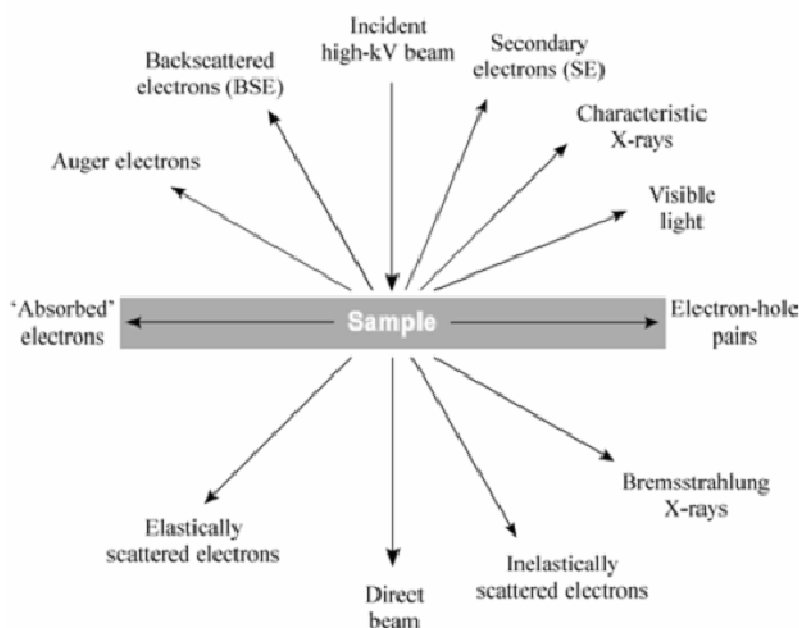


**Figure 3.2.** Signal generated in the interaction between a high-energy electron beam and a thin sample. Most signals can be detected by a SEM or a TEM.

In a SEM, the electron beam is scanned over the specimen. The electron beam can be generated by a field- or thermo emission.

Part of the incident electrons are scattered inelastically at the electrons of the target material, and lose their energy through these interactions. The energy loss per unit distance can be described by the Bethe-Bloch equation. A useful formulation of it can be

$$-\frac{dE}{dx} \cong \frac{e^4}{8\pi\epsilon_0^2} \frac{NZ}{E} \ln\left(\sqrt{\frac{e}{2}} \frac{E}{J}\right) \quad (3.1)$$

where  $N$  is the number of atoms,  $Z$  is the atomic number of the target material,  $J$  the ionization energy of the target and  $E$  the energy of the incident beam [91].

Through these scattering events, the primary electron beam effectively spreads and fills a teardrop-shaped volume, known as the interaction volume, extending from less than 100 nm to around 5  $\mu\text{m}$  into the surface, depending by the beam energy. The spatial resolution of the SEM depends on the size of the interaction volume or, equivalently, on the extent to which the material interacts with the electron beam.

The excited secondary electrons gain an energy that allows them to escape the outermost layer of the specimen. Only secondary electrons generated within a few nanometers from the surface can indeed be detected.

Other incident electrons are backscattered elastically on the target nuclei. Considering the screening effect of the nuclear charge by the electron shells, the angular scattering of electrons by the Coulomb field of the atomic nucleus can be described by the screened Rutherford scattering cross-section:

$$\frac{d\sigma}{d\Omega} = \frac{e^4}{(16\pi\epsilon_0)^2} \frac{Z^2}{E^2} \frac{1}{\left[\sin^2\left(\frac{\vartheta}{2}\right) + \sin^2\left(\frac{\vartheta_0}{2}\right)\right]^2} \quad (3.2)$$

where  $\theta$  is the scattering angle,  $\Omega$  is the solid angle and  $\theta_0$  the screening angle given by the ratio of the reduced wave length of the electrons  $\frac{\lambda}{2\pi}$  and the radius of the nucleus. The probability for a scattering at a small angle is much larger than for big angles.

SEM microscopy takes advantage of the different properties of the secondary and backscattered electrons. Since the energy of the secondary electrons is low, they are attracted with a positively charged grid on the SE-detector. The energy of the backscattered electrons is high enough to create electron-hole pairs in a semiconductor detector (the RBSD or BSE detector). They give information of the chemical composition of the target material because of the  $Z^2$  dependence of the cross-section.

It is worth noting that if the sample is insulating, the adsorbed electrons generate a high charged area on the specimen surface, which can affect the interaction of the incident electron beam with the sample surface.

During the different steps of the research, various SEM systems have been employed, namely a SEM Philips XL-30, a SEM Philips 515 and a FE-SEM LEO 1530.

A Transmission Electron Microscopy (TEM) is the equivalent of an optical microscope for an electron beam. An electron with a kinetic energy of 100 keV has a wavelength  $\lambda$  of 3.7 pm, which permits to reach sub-nanometric resolution.

Samples to be observed with TEM have to be thin enough to let part of the electron beam pass through. Some of the transmitted electrons result diffracted by the crystalline lattice of the specimen, some others traverse it without being deviated. A system of intermediate lenses can be set in order to image either a diffraction pattern or the image of the specimen on the viewing screen (Figure 3.3). The objective lens allows the imaging of the object in the corresponding image plane, by focusing of electrons starting with different directions from individual object points to the corresponding image points. The diffraction pattern can be obtained by focusing in the same point all those electrons that started in the same direction from any point in the object. Information about the correspondent lattice structure of the specimen can be derived by these diffraction patterns.

It is worth noting that TEM investigations require specifically prepared specimens, since very low thicknesses are necessary. Only some of the samples synthesized in our research were appropriate or were arranged for this purpose. The HR-TEM employed was a FEI Tecnai F20 with a FEG source.

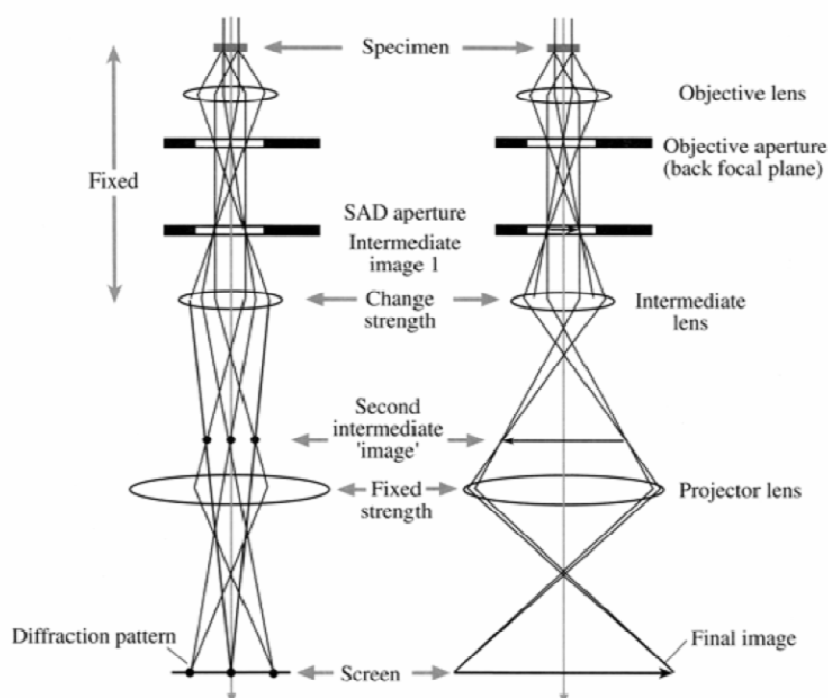


**Figure 3.3.** The two basic operations of a TEM: projecting the diffraction pattern on the viewing screen (left) or projecting the image on the screen (right). The intermediate lens selects the back focal- or the image plane of the objective lens as its objects.

The Raman spectroscopy is a commonly used non-destructive method that can give information about the crystallographic quality of a CNTs deposit. Raman scattering consists of an inelastic scattering of a high frequency radiation as a consequence of an indirect coupling of the impinging photons with the internal motions (vibrations or rotations) that occur in a molecule or crystal. A Raman scattering can be interpreted as a consequence of a perturbation of the molecular polarizability (the easy of distortion of the electron cloud of the molecule) induced by the electric field of the radiation. In a classical framework, the electron cloud of a molecule (crystal), placed in a high frequency oscillating radiation, distorts and tends to follow the oscillating electric field  $E$ , because of the coupling of the electrons with the radiation. On the other hand, because of the oscillations of the electron cloud, a subsequent rapid re-irradiation occurs in every direction, determining a scattering of the beam. Because of the internal motions (vibrations and rotations) of the molecule, the frequencies of the scattered radiation can vary of a quantity corresponding to the characteristic frequency of the vibration or rotation, with respect to the frequency of the incident beam. This is the case of an inelastic scattering or Raman scattering.

Raman spectra have been acquired by using a standard micro-Raman Renishaw 1000 spectrometer and a laser source in the visible range (He-Ne laser at 632.8 nm, maximum output power about 15 mW). The micro-Raman spectrometer is connected to a microscope, which allows the choice of the portion of sample to investigate. The microscope is equipped with a stage for the XYZ displacement of the sample. The laser spot passes through different optical elements such as spot change elements, beam splitters and deviators, filters and polarizing elements. The scattered light is then collected by a CCDs detector. Raman spectra have been collected through a 50 $\times$  objective. At the maximum laser output power, the maximum power density impinging on the sample is about  $0.25 \cdot 10^5$  W/cm<sup>2</sup> for the red laser.

When the laser beam impinges on carbon nanotubes, stimulating bonds vibrations, typical Raman signal peaks in the range 100 – 2900 cm<sup>-1</sup> are observed. Particularly, SWNTs have a clear footprint in the Raman spectrum, whose information can also be efficiently used to determine the tube diameter [92]. Regarding MWNTs, the typical spectrum exhibits two main peaks, named G and D peaks. The former one appears near 1580 cm<sup>-1</sup> wave number shift, and it is related to the vibrational modes of the C – C sp<sup>2</sup> bond in the graphene lattice (G stands for Graphite) tangential to the tube surface. The latter, between 1330 – 1360 cm<sup>-1</sup>, is related to the vibrational modes of the C – C sp<sup>3</sup> bond, which characterizes the diamond lattice (D stands for Diamond) but in CNTs is related to the presence of defects in the crystalline lattice.

The ratio of the D and G peaks intensities,  $I_D/I_G$ , is a commonly adopted mark for characterizing the quality of a CNTs sample. The smaller is the ratio, the higher is the

CNTs quality. Moreover, the width of the peak is also useful in determining the quality, since a highly graphitized CNT produces a sharp G peak.

The second-order overtone of the D peak, indicated as  $G_0$ , is also included at  $2660 - 2720 \text{ cm}^{-1}$ . This peak is another footprint of the quality of the deposit. In graphite the intensities of the G and  $G_0$  peaks are similar. Hence, low  $G_0$  peaks are related with poor graphitization of the structures. Also the ratios  $I_D/I_{G0}$  and  $I_G/I_{G0}$ , are thus quality marks.

### 3.2 Synthesis on insulating substrates

The carbon nanotubes growth process has been initially investigated in order to calibrate our CVD deposition system with respect to experimental results reported in the literature.

In the case of CNT growth on Si substrates, a barrier layer is often deposited prior to catalyst evaporation in order to prevent catalyst diffusion towards the substrate. Insulating substrates, such as  $\text{SiO}_2$  and  $\text{Si}_3\text{N}_4$  films on silicon, are common barrier layers for CNT growth [27, 93]. On  $n^+$  type,  $1 \Omega\cdot\text{cm}$ , silicon substrates,  $\text{SiO}_2$  or  $\text{Si}_3\text{N}_4$  layers were grown, by thermal oxidation and by reduced pressure CVD deposition in  $\text{SiH}_2\text{Cl}_2$  and  $\text{NH}_3$  atmosphere at  $800 \text{ }^\circ\text{C}$ , respectively.

A catalyst film is deposited by means of an electron beam evaporator in patterned or un-patterned areas. Film thicknesses can vary from very thin,  $1 - 5 \text{ nm}$  thick, to larger ones,  $30 \text{ nm}$ , depending on the sample requirements. The choice of starting from a continuous film as catalyst nanoparticles precursor has been based on two considerations. First of all, the facilities and the long, solid experience available at the CNR-IMM institute have been considered. Secondly, the deposition of a continuous film by evaporation is a feasible and cheap process for industrial production. This solution sets strict constraints on the smallest achievable dimension for the nanoparticles. Layers such as silicon oxide and silicon nitride have good barrier properties against metal diffusion through the layer, so almost all the catalyst deposited will be found as nanoparticles on the substrate. The dimension of the nanoparticles depends on catalyst film thickness, which has to be as small as possible. Our metal evaporation system allows achieving controlled thickness of  $2 \text{ nm}$ , thus adopted. Among the most common catalysts (Fe, Ni and Co) for CNT production, nickel has been chosen for the free standing configuration synthesis. Nickel is reported to produce good quality CNTs at moderately high temperature and it is more compatible with the silicon technology with respect to iron. Cobalt is commonly used where low temperature CNT syntheses and compatibility with Si technology are required, but the related CNT quality is slightly lower [49].

The usually adopted CVD process, referred to as the general process in the following, consists of many steps (Table 3.1). The deposition system is warmed up to the synthesis temperature in flowing gas. The heating profile can vary, depending on the actual investigation, among the controlled ramp, the uncontrolled ramp or the “hot-insertion”

procedure. A 20 minutes annealing process is then performed in a flowing annealing gas atmosphere in order to fragment the catalyst film into a randomly distributed population of nanoparticles. It has to be noted that this fragmentation already starts during the ramp up. The synthesis of CNTs is then carried out by flowing the carbon feedstock gas ( $C_2H_2$ ) in the furnace, together with a carrier gas, for 30 minutes. Eventually, the heating is stopped and the furnace is cooled down to room temperature in flowing inert gas. The general process is performed at atmospheric pressure.

| <b>Table 3.1</b>    |                            |                           |                          |   |                       |
|---------------------|----------------------------|---------------------------|--------------------------|---|-----------------------|
| <i>Process Step</i> | <i>Temperature</i><br>(°C) | <i>Pressure</i><br>(Torr) | <i>Time</i><br>(minutes) | <i>Process Gas</i>  |                       |
|                     |                            |                           |                          | <i>Gas Type</i>   | <i>Flow</i><br>(sccm) |
| Intro               | RT                         | 750                       | -                        | -   | -                     |
| Purge               | RT                         | 750                       | 10                       | Ar  | 1000                  |
| Ramp up             |                            | 750                       |                          |   |                       |
| Controlled          | RT→PT (650-900)            | 750                       | 100                      | Ar/NH <sub>3</sub> /H <sub>2</sub>                                | 200                   |
| Uncontrolled        | RT→PT (650-900)            | 750                       | 30 – 40                  | Ar/NH <sub>3</sub> /H <sub>2</sub>                                | 200                   |
| Hot-introduction    | PT                         | 750                       | 5                        | Ar/NH <sub>3</sub> /H <sub>2</sub>                                | 200                   |
| Annealing           | PT (650-900)               | 750                       | 20                       | Ar/NH <sub>3</sub> /H <sub>2</sub>                                | 200                   |
| Deposition          | PT (650-900)               | 750                       | 30                       | C <sub>2</sub> H <sub>2</sub> +Ar/NH <sub>3</sub> /H <sub>2</sub> | 200                   |
| Cooling down        | PT→RT                      | 750                       | -                        | Ar  | 200                   |

**Table 3.1.** Synoptic description of the general process employed in the investigation on the synthesis of CNTs on insulating substrates. Different  $C_2H_2$  percentages in the mixture with carrier gas (5 – 30 %) have been used. (RT = Room Temperature; PT = Process Temperature).

### Catalyst nanoparticles formation

All the theoretical models developed for the CNT synthesis stress the importance of the nanoparticle dimensions in controlling the CNT diameters. For this reason, the parameters influencing dimensions and site density of a catalytic nanoparticles distribution obtained by fragmentation of a continuous nickel film have been investigated. A narrow distribution of dimensions can help in understanding the synthesis process, since it reduces the differences of the growth mechanism due to different seed dimensions. Moreover, a distribution of nanoparticles in the range 1 – 5 nm allows the synthesis of single-wall carbon nanotubes, which are still one of the hot topics in the research.

A 2 nm thick nickel film was deposited on SiO<sub>2</sub> and Si<sub>3</sub>N<sub>4</sub> barrier layers, as precursor of the nickel nanoparticles. The catalyst film thickness was kept constant for all

samples. These, approximately of  $2 \times 1 \text{ cm}^2$  size, are placed inside the hot wall CVD furnace. To investigate the possibilities of the CVD system in the nanoparticles formation, the general process described before has been modified by replacing the deposition with a “pseudo-deposition” step of the same duration but without injection of carbon feedstock gas in the furnace. The 100 minutes long controlled ramp has been adopted in order to work in more reproducible conditions (Table 3.2). With this process, three different temperatures and three different process gases have been investigated to achieve the smallest nanoparticle dimensions on the two insulating substrates. Different thicknesses of these barrier layers have also been studied.

| Table 3.2         |                     |                   |                                    |                |
|-------------------|---------------------|-------------------|------------------------------------|----------------|
| Process Step      | Temperature<br>(°C) | Time<br>(minutes) | Process Gas                        |                |
|                   |                     |                   | Gas Type                           | Flow<br>(sccm) |
| Intro             | RT                  | -                 | -                                  | -              |
| Purge             | RT                  | 10                | Ar                                 | 1000           |
| Ramp up           | RT→PT (700-900)     | 100               | Ar/NH <sub>3</sub> /H <sub>2</sub> | 200            |
| Annealing         | PT (700-900)        | 20                | Ar/NH <sub>3</sub> /H <sub>2</sub> | 200            |
| Pseudo-Deposition | PT (700-900)        | 30                | Ar/NH <sub>3</sub> /H <sub>2</sub> | 200            |
| Cooling down      | PT→RT               | -                 | Ar                                 | 200            |

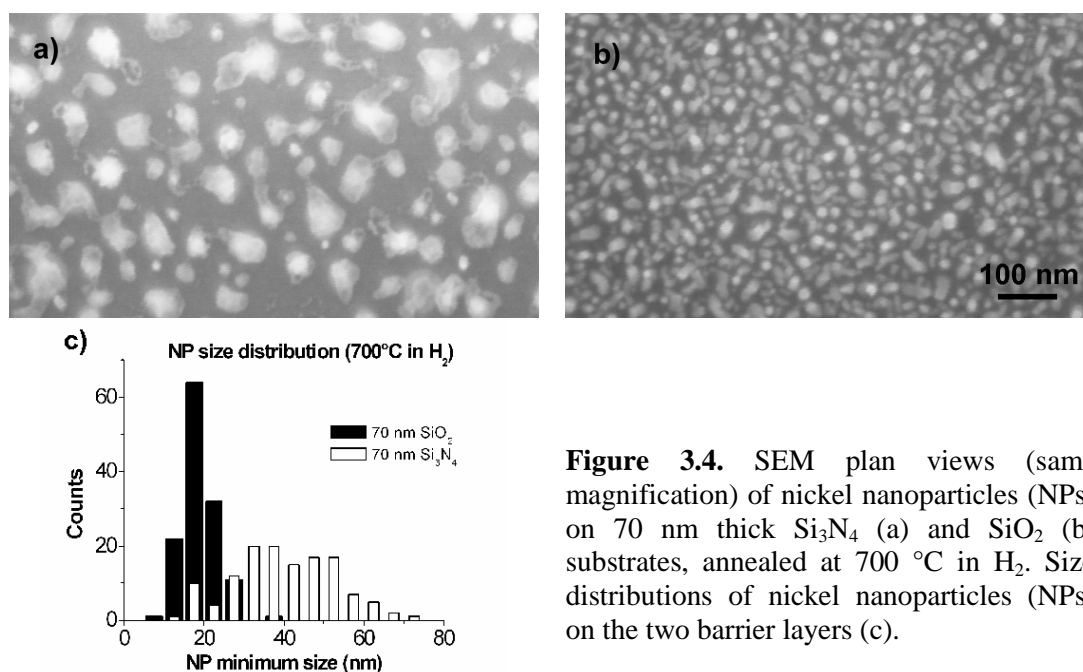
**Table 3.2.** Synoptic description of the process employed in the investigation on the nanoparticles formation. Pressure is maintained at 750 Torr during all steps (RT = Room Temperature; PT = Process Temperature).

The samples have been characterized by means of scanning electron microscopy (FE-SEM LEO 1530) at low voltage (5 kV). A set of micrographs has been taken for collecting an appropriate population of nanoparticles. A total number of 150 clusters has been taken into account for every sample. Because many nanoparticles present an oblate shape, an ideal oval shape has been assumed and the two main diameters have been measured. Since CNT oblate section has never been reported, it seems likely that only the minimum diameter can influence the nanotube dimension. Furthermore, preliminary CNT growths have indicated that, on these nanoparticles, CNTs have an average diameter close to the minimum nanoparticle size. Consequently, in case of nanoparticle with oval-shape, only the minimum diameter has been considered for statistical calculations, whereas an aspect ratio indicator has been additionally calculated as the ratio between maximum and minimum nanoparticle size.

Four kinds of sample have been initially prepared. Three layers of silicon oxide of different thicknesses (9, 70 and 350 nm) have been grown in order to control if this parameter can have some influence in the nanoparticles formation. On the fourth sample a silicon nitride barrier layer 70 nm thick have been deposited.

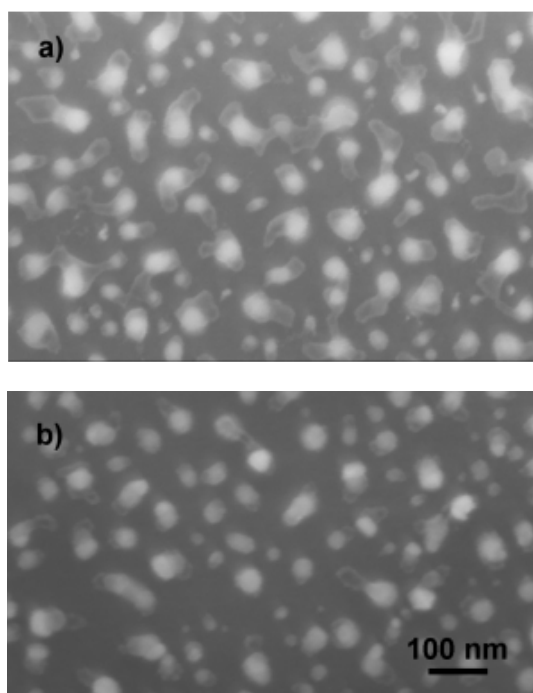
The investigation has been firstly focused on the effect of different substrates on nanoparticles formation, by comparing the populations obtained on the three SiO<sub>2</sub> substrates and on the Si<sub>3</sub>N<sub>4</sub> one. The pseudo-synthesis process has been performed at 700 °C, using H<sub>2</sub> as annealing gas. Figure 3.4 shows SEM images of the resulting nanoparticles distributions on the 70 nm Si<sub>3</sub>N<sub>4</sub> (Figure 3.4a) and on the 70 nm SiO<sub>2</sub> (Figure 3.4b) substrates. SEM results and imaging analysis of the nanoparticles on various SiO<sub>2</sub> substrates show negligible differences in morphology and distribution when varying oxide thickness. This indicates that heat dissipation of the layer is not a crucial parameter, at least in the investigated thickness range between 9 and 350 nm. Therefore, further investigations concerning the SiO<sub>2</sub> substrates have been carried out only on 70 nm thick films.

Figure 3.4 clearly indicates that on SiO<sub>2</sub> the nanoparticles are smaller than on Si<sub>3</sub>N<sub>4</sub> (about 20 nm compared with 40 nm), with a narrower distribution of their dimensions, as can be seen in Figure 3.4.c. These considerations are also supported by density analysis: on SiO<sub>2</sub>, the nanoparticles (NPs) density is an order of magnitude larger than on Si<sub>3</sub>N<sub>4</sub> (about 10<sup>11</sup> NPs/cm<sup>2</sup> and 10<sup>10</sup> NPs/cm<sup>2</sup> respectively). All the nanoparticles show a rather spherical planar section. It is also worth to note that nanoparticles on Si<sub>3</sub>N<sub>4</sub> substrate exhibit a halo surrounding a massive core, whereas this feature is not observed on the SiO<sub>2</sub> ones (Figures 3.4.a and 3.4b).



**Figure 3.4.** SEM plan views (same magnification) of nickel nanoparticles (NPs) on 70 nm thick Si<sub>3</sub>N<sub>4</sub> (a) and SiO<sub>2</sub> (b) substrates, annealed at 700 °C in H<sub>2</sub>. Size distributions of nickel nanoparticles (NPs) on the two barrier layers (c).

The effect of temperature on the nanoparticles formation has been then studied. The pseudo-synthesis process has been performed using  $H_2$  as annealing gas, in the range of temperatures commonly employed in the CVD synthesis of CNT, i.e. at 700, 800 and 900 °C. SEM plan views of nanoparticles produced at different temperatures on the 70 nm  $Si_3N_4$  substrate are shown in Figure 3.4a (700 °C) and Figure 3.5 (800 °C and 900 °C). Imaging analyses for both  $Si_3N_4$  and  $SiO_2$  substrates are summarized in Figure 3.6, where the nanoparticles minimum dimension and aspect ratio trends are reported. On  $SiO_2$ , nanoparticles minimum dimension remains almost constant as temperature increases, while the aspect ratio slightly increases. On the other hand, on  $Si_3N_4$  the nanoparticles size distribution becomes narrower and shifts towards slightly lower values with increasing temperature. As shown in Figure 3.5, the halo surrounding the nanoparticles core, previously described, gets smaller with increasing temperature. At 900 °C it completely disappears and can be reasonably considered to be absorbed in the core; correspondingly the nanoparticles shape tends to become more spherical.



**Figure 3.5.** SEM plan views of nickel nanoparticles on 70 nm  $Si_3N_4$  substrate after the standard annealing process in  $H_2$  at 800 °C (a) and 900 °C (b).

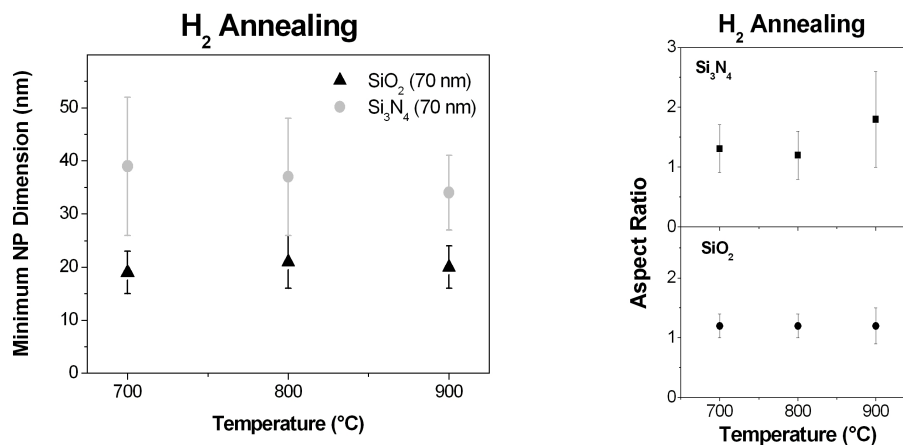


**Figure 3.6.** Ni nanoparticles minimum dimensions (left) and aspect ratios (right) on SiO<sub>2</sub> and Si<sub>3</sub>N<sub>4</sub> as a function of annealing temperature. Error bars are related to the width of the nanoparticles distributions.

Finally the dependence of nanoparticles morphology upon process atmosphere has been studied, being the pseudo-synthesis process carried out at 700 °C using Ar, NH<sub>3</sub> or H<sub>2</sub> atmospheres. H<sub>2</sub> and NH<sub>3</sub> are commonly used as reducing gas, whereas Ar has an inert nature. NH<sub>3</sub> has been reported to behave also as an etching and reactive gas, playing different roles as far as the nanoparticles formation is concerned [39, 94, 95]. It is currently under discussion in the literature if NH<sub>3</sub> is efficient or not in etching the catalyst nanoparticles [39, 94]. Furthermore, NH<sub>3</sub> is claimed to chemically react with nickel nanoparticles on SiO<sub>2</sub> forming compounds such as Ni<sub>3</sub>N, which are thought to preserve the catalytic activity during the CNT synthesis. In addition, a not significant amount of nitrogen is incorporated in SiO<sub>2</sub> substrate when nickel is not used [95]. Preliminary X-ray Photoelectron Spectroscopy (XPS) investigations on our SiO<sub>2</sub> samples confirm these results. Differently from [95], it is believed that chemical modifications strongly occur also in the substrate when nickel is used. Nickel is known to be an efficient catalyst for ammonia dissociation [96], which results in an enhanced oxinitrides formation on the SiO<sub>2</sub> substrate.

The SEM image of the H<sub>2</sub> annealed sample has been already shown in Figure 3.4b. Figure 3.7 shows the SEM images of the nickel nanoparticles formed on the 70 nm thick SiO<sub>2</sub> sample in Ar (a) and NH<sub>3</sub> (b) flow. The minimum and maximum dimensions measured for each nanoparticle, deduced from the SEM imaging analysis, are also shown in Figure 3.7c. On the SiO<sub>2</sub> substrate, the minimum diameter of the nanoparticles remains the same independently of the annealing gas, whereas the clusters morphology abruptly changes. Argon produces very elongated and curly nanoparticles, with a mean aspect ratio twice larger if compared with the nanoparticles obtained in H<sub>2</sub> and NH<sub>3</sub> atmospheres. Furthermore, in the case of NH<sub>3</sub> annealing (Figure 3.7b) nanoparticles appear flatter than in the case of H<sub>2</sub> (Figure 3.4b), as the different surface contrast in SEM observations indicates. This result seems to confirm that an NH<sub>3</sub> atmosphere can etch the nanoparticles

[39]. The same trend has been found on the  $\text{Si}_3\text{N}_4$ , but in that case the nanoparticles distributions exhibit larger dimensions and broader widths.

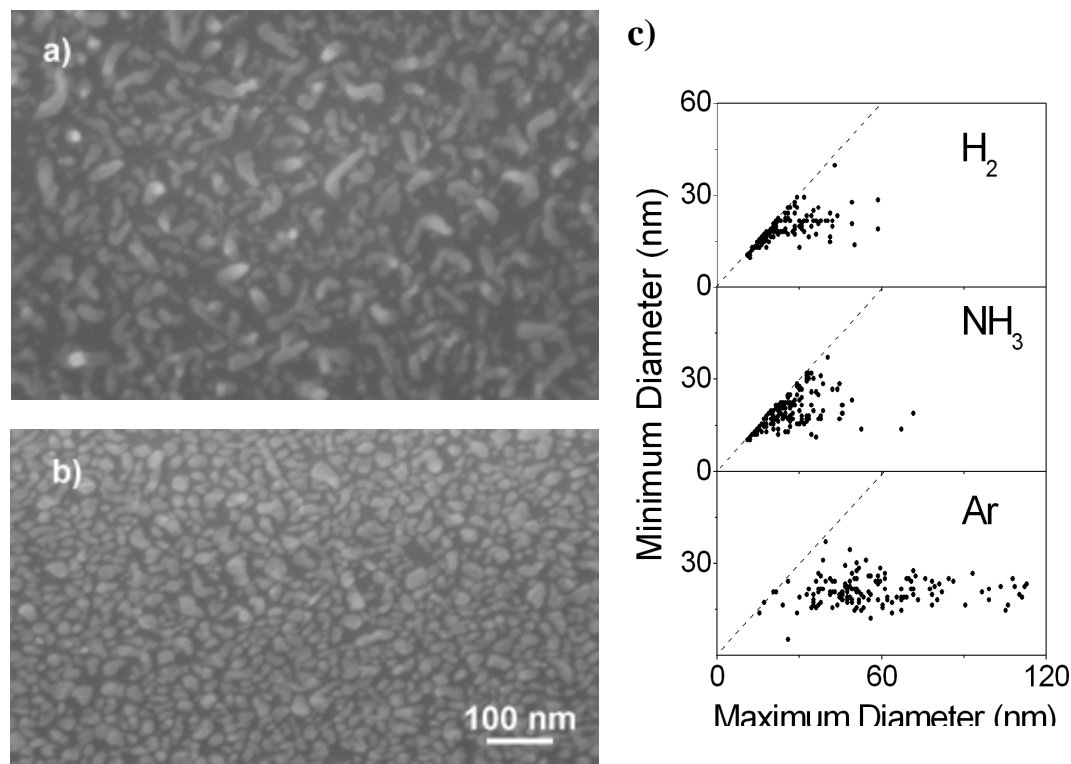


**Figure 3.7.** SEM images (same magnification) of Ni nanoparticles on  $\text{SiO}_2$  resulting from a 700 °C annealing in Ar (a) and in  $\text{NH}_3$  (b). Shape distributions (maximum and minimum diameters) of Ni nanoparticles on 70 nm  $\text{SiO}_2$  substrates resulting from 700 °C annealing in different gases ( $\text{H}_2$ ,  $\text{NH}_3$  and Ar) are summarized in (c).

Nanoparticles formation from a thin film is known to strongly depend upon catalyst-substrate wettability, coalescence of the nanoparticles and chemical reactions between the catalyst and the substrate. The experimental results we obtained show that the barrier layer placed between silicon and the catalyst film is an important factor affecting the nanoparticles formation. It plays a fundamental role not only as a diffusion barrier but also as an active element for controlling the nanoparticles. It seems reasonable that the different behaviour of  $\text{SiO}_2$  and  $\text{Si}_3\text{N}_4$  has to be ascribed to their different chemical properties. Stronger chemical bonds between nickel and the barrier layer should enlarge the flat cluster size, preventing film fragmentation, and should also enhance the nanoparticle-substrate wettability. This eventually leads to nanoparticles distributions with larger dimensions and lower site density. On the other hand, weaker chemical bonds should enhance the film cracking, resulting in higher site density and smaller dimensions of the nanoparticles. Since  $\text{Si}_3\text{N}_4$  gives nanoparticles with site density one order of magnitude smaller compared with  $\text{SiO}_2$ , and nanoparticles dimensions about a factor of

two larger, we can conclude that the interaction between nickel and the barrier layer is stronger for  $\text{Si}_3\text{N}_4$  with respect to  $\text{SiO}_2$ . Also the temperature evolution of the nanoparticle halo characterizing the silicon nitride samples confirms this interpretation: at lower temperature there is not enough thermal energy to accomplish the conglomeration of the nanoparticles, whereas at higher temperature a more compact shape of the nanoparticles can be achieved. On  $\text{SiO}_2$  the chemical binding energy is easily overcome by the thermal energy and at low temperature the conglomeration step has already been completed; at higher temperature the nanoparticles are affected by a more intense surface mobility and coalescence. Then, in the investigated temperature range, the minimum nanoparticle dimension can be obtained at low temperature on  $\text{SiO}_2$ , and at high temperature on  $\text{Si}_3\text{N}_4$  substrates respectively. The site density consequently has an opposite trend, since higher densities are related to smaller nanoparticles.

The annealing gas as well affects nanoparticles dimension and shape. The different performances of the various gases could be related to their chemical characteristics or thermal conductivity. An additional process using He as annealing gas allows a comparison between gases with comparable thermal conductivity but different chemical nature, like  $\text{H}_2$  and He. The samples annealed in He atmosphere show features more similar to those annealed in Ar rather than in  $\text{H}_2$ , so pointing out the predominant role of the gas chemical reactivity. The annealing gas should affect the Ni nanoparticles distribution by means of a change in the chemical state of either the substrate barrier layer or the nickel. If the nanoparticles oxidize, their surface valence bonds are saturated and coalescence is hampered. The free energy of the gas-metal and gas-substrate interfaces enters directly in the wettability definition, and probably a stronger effect comes from chemical transformations of the surfaces.

The most efficient annealing gases for obtaining the smallest nanoparticle dimension seem to be either  $\text{H}_2$  or  $\text{NH}_3$ . Hydrogen produces smaller nanoparticles. Ammonia effects on the nanoparticle dimensions can be ascribed both to its reducing and etching features. Fibrous nanoparticle structures form on  $\text{Si}_3\text{N}_4$  at 700 °C in  $\text{NH}_3$ . The low thermal budget, not sufficient for the nanoparticles conglomeration, combined with the gas etching effect is supposed to be the cause of this anomalous morphology. To check this hypothesis an additional pseudo-deposition has been performed at 1000 °C. Even if the etching effect is stronger, the nanoparticles are able to completely conglomerate in a well defined core. The halos observed in the case of  $\text{H}_2$  annealing are not observed at 700 °C in  $\text{NH}_3$ , probably because they are more easily etched by  $\text{NH}_3$  than the nanoparticles core.

### Carbon nanotubes deposition

Following the studies on the nanoparticles, the synthesis of CNT was investigated. In a C-CVD deposition of CNTs a carbon feedstock gas is decomposed in the presence of a catalyst. The catalyst has two functions: to enhance the carbon gas dissociation at the CVD relatively low temperatures and, mainly, to break the symmetry and hence to force the precipitation of the carbon into ordered structured, i.e. the CNTs. The reactions of dissociation at the catalyst surface, carbon precipitation and CNT synthesis have to be controlled by limiting the deposition of other by-products, such as amorphous carbon or defective structures. It is therefore important to maintain active the catalyst during the synthesis otherwise the deposit would consist only of amorphous carbon. A proper balance between carbon supply and carbon precipitation has to be obtained for the catalyst. If an excess of carbon decomposes and arrives on the catalyst, the nanoparticles can be poisoned so that no more catalytic synthesis occurs. On the contrary, if the carbon supply at the catalyst nanoparticles is not sufficient, the reaction proceeds too slowly and other unwanted reactions, such as thermal cracking of the hydrocarbon, can be favoured.

The CVD process consists of many steps, each characterized by a number of parameters, which have to be tuned in order to find the best condition for the CNT synthesis. Each process parameter is related to the others and, furthermore, the entire set is also related to the sample features, namely the substrate and the catalyst characteristics. A unique appropriate set of parameters does not exist for all the configurations and the CVD process has to be optimized for each different sample typology.

CNT deposits obtained by varying the process parameters have been characterized by SEM investigation and, on selected samples, by Raman and TEM analyses. In the following the parameters have not been changed with respect to the general process (see Table 3.1) if not explicitly stated.

The same samples analyzed in the nanoparticles investigation have been used in the CVD process, with a 2 nm thick nickel film evaporated on SiO<sub>2</sub> or Si<sub>3</sub>N<sub>4</sub> barrier layers. Also 4 nm thick nickel films has been employed, but at the deposition temperature of 750 °C such a catalyst thickness gave CNT diameters about a factor of two larger compared with the 2 nm thick Ni films. Consequently, the catalyst thickness has been maintained at the minimum reproducible value of 2 nm.

The synthesis has been initially performed using NH<sub>3</sub> during the entire process, from the heating to the deposition. A temperature of 700 °C, reached with an uncontrolled ramp, has been set. In these preliminary conditions, mainly based on the available literature, the percentage of the carbon feedstock gas, i.e. acetylene, in the ammonia carrier gas has been investigated. The total flux has been maintained at 150 sccm. The carbon feedstock dilution is fundamental in order to balance the carbon supply and the amorphous carbon etching in the synthesis reactions. Three different C<sub>2</sub>H<sub>2</sub> percentages with respect to the total flux have been used, i.e. 30 %, 10 % and 5 %.

At the end of the syntheses, the samples show a deposit on the surface, whose colour is related to the amount of deposited carbon: the darker is the sample the larger is the deposition. CNTs have on both substrates a good adherence, but the samples have to be carefully treated as carbonaceous material can be easily detached from the substrate when samples are touched with tweezers. In these experimental conditions, the typical deposit is a carpet made of multi-walls CNT bundles. If the density is high enough, the CNTs grow one parallel to each other, perpendicularly to the substrate, due to the Van der Waals interactions. Otherwise, the CNTs bend or grow parallel to the substrate.

The acetylene fraction of 30 % turns out to be too large. Catalyst seeds are quickly poisoned and therefore only thermal cracking of acetylene occurs, with the subsequent deposition of amorphous materials. On the other hand, a dense carpet of vertically aligned CNTs has grown on both substrates employing a 10 % mixture. On the  $\text{Si}_3\text{N}_4$  layer the mean height is  $1.7 \mu\text{m}$ , with some isolated CNTs grown higher than the others, up to  $4 \mu\text{m}$ . On  $\text{SiO}_2$ , the mean height is  $2.6 \mu\text{m}$ , but an amorphous carbon layer is deposited on the top of the carpet. The best condition is found with a mixture of 5 % acetylene in ammonia: on both substrates the carpet height results reduced to about  $1 \mu\text{m}$ , but with a limited amount of amorphous deposit. Also the CNT diameters become smaller. Since amorphous carbon can be deposited not only on the catalyst nanoparticles or on the top of the CNTs, but also on their walls, smaller diameters are related to a cleaner synthesis. TEM investigations of the  $\text{SiO}_2$  sample show (Figure 3.8) that the carpet consists of MWNTs, composed by 15 – 20 walls. The observed structure evidences many kink defects that made the tube bent.

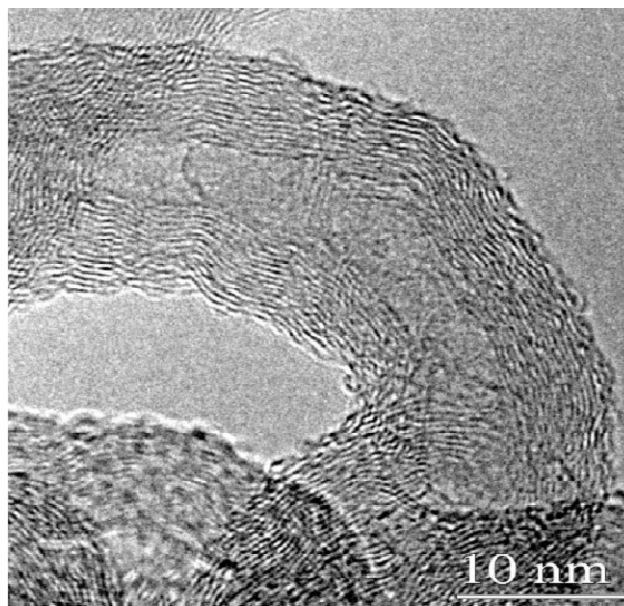


**Figure 3.8.** TEM image of a MWNT grown on  $\text{SiO}_2$  as a substrate at  $700 \text{ }^\circ\text{C}$  with a deposition mixture of 5 %  $\text{C}_2\text{H}_2$  in  $\text{NH}_3$ .

At the same temperature of 700 °C on Si<sub>3</sub>N<sub>4</sub> substrate, the total flux inside the furnace has been also varied keeping constant the carbon feedstock percentage over the total gas mixture. With a total flux of 450 sccm an increase of a factor of two in the height of the CNT carpet is obtained, but at the same time the CNT diameters also increase a factor of three, up to 70 nm. This is a value much large with respect to the starting nanoparticle diameters. Thus it is supposed that a significant amount of amorphous carbon has been deposited on the CNT walls. To achieve a total flux of 1500 sccm in the deposition system, a dilution with an inert gas has been necessary. The process has been therefore performed in a mixture composed by 5 % C<sub>2</sub>H<sub>2</sub>, 25 % NH<sub>3</sub> and 70 % Ar. The carpet of vertically aligned CNTs is 1.7 μm high, and the corresponding diameters grow up to 90 nm. The reduced percentage of the etching gas with respect to the total flux seems to result in a larger amorphous carbon deposition. This is probably due to the shorter “residence time” of the ammonia molecules on the sample. The amorphous carbon removal is thus less effective and the catalyst is more easily poisoned. The synthesis is thus stopped in advance and more amorphous deposit grows on the CNTs walls.

Even if the quality of the deposited material has been improved, at 700 °C it remains unsatisfactory. Higher energies are required for the synthesis of CNTs of better crystallinity by CVD process. The process has been then studied varying the temperature and using ammonia and hydrogen gases during the entire process. The process temperature has been investigated in the range 650 and 900 °C, with uncontrolled ramp up, using NH<sub>3</sub> as process gas. The deposition step has been performed in a mixture of 5 % acetylene on SiO<sub>2</sub> substrate.

At 650 °C, only a first evidence of CNT deposit can be seen in the SEM images: since the CNT density is very low, a great number of nanoparticles has not been active as catalysts. Otherwise, at 700 °C the typical CNT carpet starts to appear, even if the height is only approximately 1 μm. Increasing the process temperature, the height of the carpet grows up to a limit of 6 μm at 850 °C, as can be seen in Table 3.3. A similar trend can be found in the diameter of the CNTs. At 650 °C the CNT mean diameter is quite large, i.e. about 70 nm, but at 700 °C the diameter falls down to a 20 – 25 nm value, similar to the dimension of the nanoparticles formed in similar conditions (Figure 3.7b). A further increase of the temperature results in a slight increase of the diameter, up to a mean value of 30 – 35 nm.

These results on the temperature effect are in agreement with a strict correlation between the nanoparticle dimensions and the CNT ones. A temperature of 650 °C associated with a short, uncontrolled ramp, lasting only 50 minutes, is probably not enough to let the complete fragmentation of the nickel film and thus the CNT diameter is large. At 700 °C the energy budget is enough to accomplish the process and produce CNT dimensions comparable with those obtained for the nanoparticles, in the reported investigation.

| Table 3.3           |                                    |                  |
|---------------------|------------------------------------|------------------|
| Temperature<br>(°C) | CNTs                               |                  |
|                     | Carpet height<br>( $\mu\text{m}$ ) | Diameter<br>(nm) |
| 650                 | -                                  | 70               |
| 700                 | 1                                  | 20 – 25          |
| 750                 | 3.6                                | 20 – 40          |
| 800                 | 4.5                                | 35 – 40          |
| 850                 | 6                                  | 30 – 40          |
| 900                 | 6                                  | 30 – 40          |

**Table 3.3.** A minimum temperature of 700 °C is necessary to allow the complete fragmentation of the catalyst film and the formation of CNTs. Above this threshold, the mean diameter of the CNTs increases only slightly, whereas the height of the CNT carpet reaches a limit value of 6  $\mu\text{m}$ .

TEM investigations confirm the improvement of the crystallographic quality of the CNTs when raising the process temperature. The carpet grown at 750 °C show that the MWNTs consists of approximately 25 – 30 walls, whose graphitization improves when moving from the outer walls to the inner ones. At 900 °C, the MWNTs exhibit better wall graphitization (Figure 3.9). In both the cases, it is visible the nickel nanoparticles included at the tip of the MWNT.

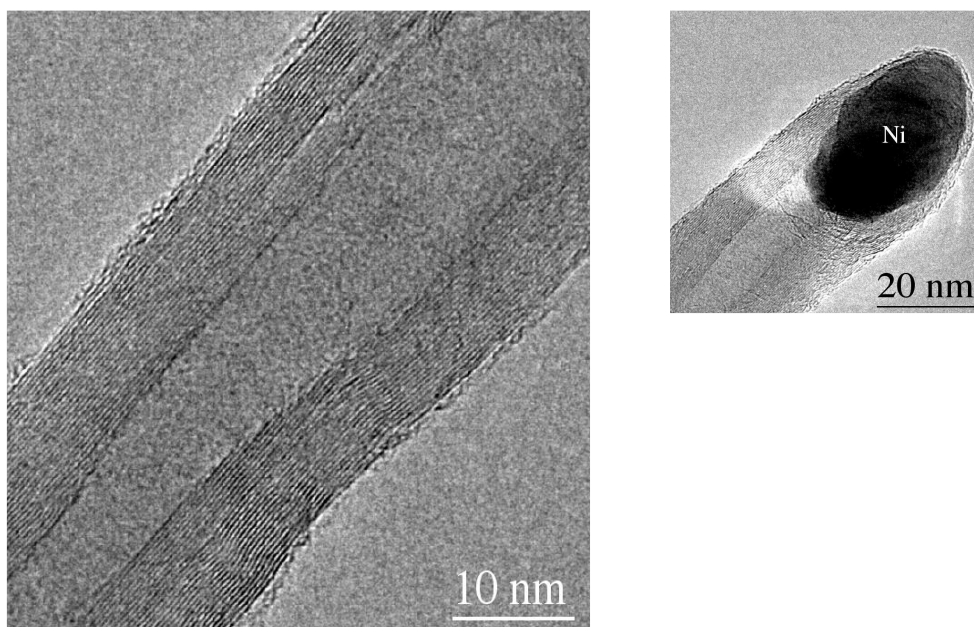


**Figure 3.9.** High resolution TEM images of a MWNT grown at 900 °C on  $\text{SiO}_2$  in a process with a mixture of 5 %  $\text{C}_2\text{H}_2$  in  $\text{NH}_3$ , with uncontrolled heating ramp. On the left, the good graphitization of the walls is evident. On the right, a Ni nanoparticle included in the CNT tip is shown.

The same investigation on the morphology of CNT carpets has been carried out using  $H_2$  as process gas. Two different temperatures, 750 °C and 900 °C, have been studied. A mixture of 1 % of acetylene in hydrogen has been determined to optimize the synthesis. On both  $Si_3N_4$  and  $SiO_2$  substrate layers, a particular edge effect is observed. The samples are not uniform over the entire area, as a black deposit grows only at the edges, extending about some millimetres from the boundaries. The effect occurs at 750 °C but it is more evident at 900 °C. At 900 °C, at the centre of the sample area only few CNTs and a population of nickel nanoparticles are observed. These nanoparticles do not show any carbon shield, as indicated by the SEM images, taken with the detector of back-scattered electrons. The few CNTs, 1  $\mu m$  high in the  $SiO_2$  case, are of good quality: they have few kink defects or amorphous deposit on their outer walls. The transition to the edge zone is quite gradual. On this zone a 20  $\mu m$  thick deposit of amorphous carbonaceous materials is observed.

Further investigations concerning the  $H_2$  effects on the CNT synthesis have been carried out at 900 °C in order to discriminate between the annealing and the deposition step which is affected by the hydrogen. A temperature profile which includes a controlled heating ramp 100 minutes long has been adopted. To make uniform the sample preparations, a process employing a mixture of 5 % acetylene in hydrogen during the synthesis step has been performed. The occurrence of the edge effect has been proven also in these conditions. As a reference, a synthesis is performed in the same conditions but employing  $NH_3$  during the whole process. Finally, two mixed processes have been carried out keeping the same acetylene dilution percentage in the carrier gas. One involves a ramp up and annealing in  $NH_3$  and deposition in  $H_2$  and  $C_2H_2$ , the other one a ramp up and annealing in  $H_2$  and deposition in  $NH_3$  and  $C_2H_2$ .

SEM observations show CNTs grown using  $NH_3$  as annealing and carrier gas (Figure 3.10). On  $SiO_2$ , the average dimension of the nickel nanoparticles (Figure 3.10a) is about 20 nm. The vertically aligned CNTs forming the 6  $\mu m$  thick dense carpet, shown in Figure 3.10b, have diameters in the 20 – 25 nm range. On  $Si_3N_4$ , the CNT carpet (Figure 3.10d) is less dense and thick. The mean thickness is approximately 3  $\mu m$ , but some isolated CNT grew up to 7  $\mu m$ . The nickel nanoparticles on this substrate (Figure 3.10c) have an average dimension of about 100 nm, while the average diameter of the corresponding CNTs is about 60 nm.

The process that employed a  $H_2$  annealing and an  $NH_3$  diluted deposition steps leads to highly non-uniform CNT deposition on the samples area. The only difference with respect to the sample entirely processed in  $H_2$  is only a slightly larger presence of CNTs in the centre.

On the other hand, as shown in Figure 3.11, the cross-section SEM micrograph of the sample grown using the process with an  $NH_3$  annealing and a  $H_2$  diluted deposition steps on  $SiO_2$  shows a 4  $\mu m$  thick carpet, made up of almost vertically aligned multi-walls CNTs, with diameters in the range 25 – 35 nm. On  $Si_3N_4$ , the CNT carpet is similar to the

one produced using only  $\text{NH}_3$ , reported in Figure 3.10d, but the mean thickness is about  $4\ \mu\text{m}$  with the extruding CNTs up to  $10\ \mu\text{m}$ . The respective nanoparticles morphologies are the same shown in Figure 3.10a and 3.10c.

By comparing these results, it turns out that the nickel nanoparticles formed by the  $\text{H}_2$  annealing produces a non-uniform CNT synthesis, independently on the carrier gas, either  $\text{H}_2$  or  $\text{NH}_3$ , used in the deposition mixture.

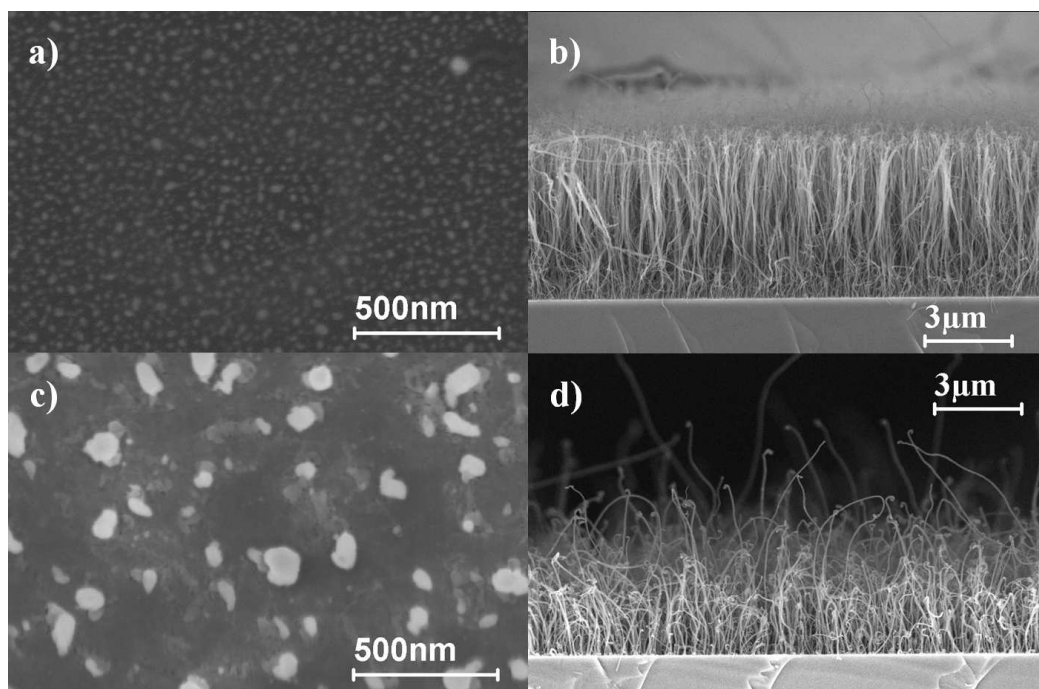


**Figure 3.10.** Cross-section SEM micrographs of Ni nanoparticles treated in  $\text{NH}_3$  at  $900\ ^\circ\text{C}$ , on  $\text{SiO}_2$  (a) and on  $\text{Si}_3\text{N}_4$  (c). CNTs grown on these nanoparticles at  $900\ ^\circ\text{C}$  in  $\text{NH}_3$  and  $\text{C}_2\text{H}_2$  on  $\text{SiO}_2$  (b) and  $\text{Si}_3\text{N}_4$  (d).

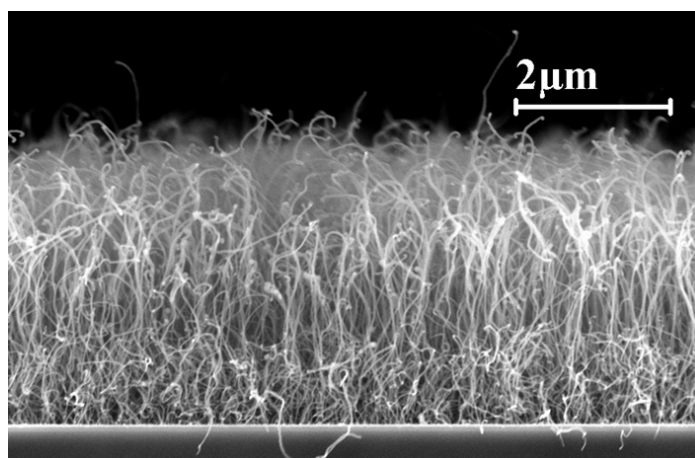


**Figure 3.11.** Cross-section SEM micrograph of CNT grown on  $\text{SiO}_2$  substrates at  $900\ ^\circ\text{C}$  in  $\text{H}_2$  and  $\text{C}_2\text{H}_2$ , following Ni nanoparticles formation in  $\text{NH}_3$  (see Figure 3.10a).

SEM investigations reveal nickel clusters inside the CNT hollows, with dimensions smaller than the starting nanoparticles. In a few samples, these clusters are located at the CNT tips. An high magnification image (Figure 3.12) of the  $\text{Si}_3\text{N}_4$  sample processed at 900 °C using  $\text{NH}_3$  as annealing and carrier gas, already shown in Figure 3.10d, reports many elongated nickel clusters (up to 300 nm long) distributed along the central CNT hollow.

This result as well can be explained according to the VLS model [41]. The carbon feedstock gas decomposes over the catalyst nanoparticle surface: carbon dissolves inside the catalyst creating a liquid metal carbide compound, which accumulates until a super-saturation is reached. The excess carbon then precipitates in an organized structure, the CNT, whose graphene sheets tensile strength can split part of the liquid nanoparticle. The CNT internal diameter is smaller than the starting nanoparticle diameter, because of the pear-shape assumed by the liquid nanoparticle. The outer diameter also depends on the amorphous carbon which can deposit on the CNT surface.

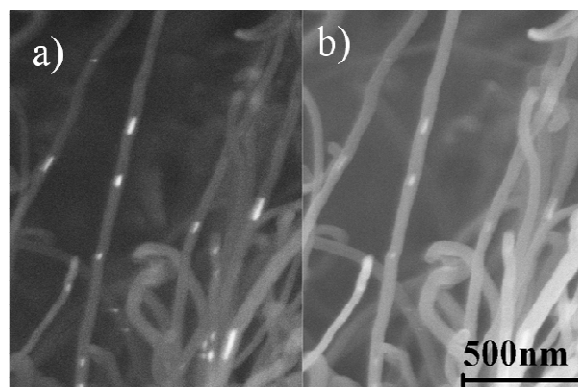


**Figure 3.12.** Back scattered electrons (a) and secondary electrons (b) SEM micrographs of the sample synthesized at 900 °C on  $\text{Si}_3\text{N}_4$  in  $\text{NH}_3$  and  $\text{C}_2\text{H}_2$  gas mixture. The Ni clusters appear brighter in the back scattered electron image.

Raman spectra of CNTs deposited at 900 °C, using either a process with  $\text{NH}_3$  as annealing and carrier gas (curve 2), or the mixed processes (curves 1 and 3) are shown in Figure 3.13. The ratios of the intensities of D and G peaks,  $I_D/I_G$ , and the normalized intensities of the D and G peaks with respect to  $G_0$  (the second-order overtone of the G peak)  $I_D/I_{G0}$ ,  $I_G/I_{G0}$ , are also reported. The trend of these ratios [97] indicates that the CNTs quality dramatically improves if nickel nanoparticles are formed in  $\text{NH}_3$ , rather than in  $\text{H}_2$ , and the deposition of CNTs is carried out in  $\text{H}_2$  and  $\text{C}_2\text{H}_2$ . However, the high D peak intensity and the presence of a shoulder in the G peak (at about  $1618\text{ cm}^{-1}$ ) in the first spectrum prove that the multi-walls CNTs (shown in Figure 3.11) are still defective.

The results agree with data reported in the literature, confirming that the  $\text{NH}_3$  treatment of the catalyst nanoparticles is important to preserve the catalytic activity of the nickel nanoparticles during the CNT growth. It has been reported that its effect is to keep the catalyst surface free of amorphous carbon, etching it away [94]. Furthermore, it has already been said that  $\text{NH}_3$  is claimed to form compounds, such as  $\text{Ni}_3\text{N}$ , that favours the detachment of the graphitic layers from the nanoparticles in the first stages of the synthesis

[95]. Both mechanisms finally resulted in a better CNT growth, by increasing the site density of the nanoparticles effectively active or by prolonging their active state during the synthesis.

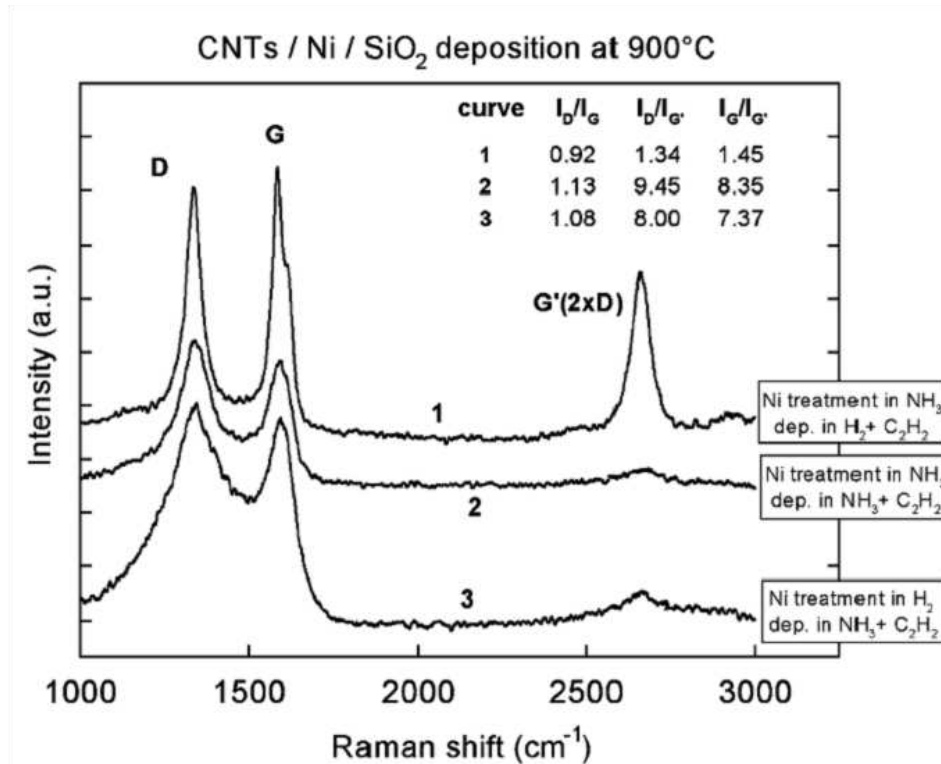


**Figure 3.13.** Raman spectra in the range 1000–3000 cm<sup>-1</sup> of various CNT samples synthesized at 900 °C, on SiO<sub>2</sub> substrates, using different gases both for the Ni nanoparticles formation and the CNT synthesis.

The origin of the edge effect related to the H<sub>2</sub> annealing is not clearly understood yet. A non-uniform annealing treatment of the catalyst nanoparticles is difficult to be supposed, since the annealing conditions are quite stable. It is more likely that the local differences arise during the deposition step, which is more critical, being enhanced by an improper preparation treatment of the catalyst. A thermal gradient along the sample holder large enough to be so effective on a 2 x 1 cm<sup>2</sup> sample area can be hardly supposed. A more realistic hypothesis could be a different gas supply between the central and the border zone. The amount of carbon feedstock can decrease moving from the borders to the centre. This affects the CNT growth differently in the two areas. On the borders too much carbon feedstock gas is available at the catalytic nanoparticles and this leads to their quick poisoning. After that, acetylene is dissociated only thermally and precipitates in amorphous carbon. This effect should be partially opposed by an NH<sub>3</sub> annealing treatment of the catalyst, but not from an H<sub>2</sub> one. In the centre, a limited amount of carbon feedstock gas arrives and the conditions for the CNT growth are rarely fulfilled. A deeper investigation

has to be performed to fully understand this behaviour, including a gas fluid-dynamic study.

The differences observed between the samples synthesized employing  $H_2$  and  $NH_3$  as carrier gas, after the annealing in  $NH_3$ , are likely due to the different equilibrium among the chemical reactions involved in the CNT growth, namely the dissociation of acetylene and the formation of ordered or disordered carbonaceous structures, the etching of the amorphous carbon and the maintenance of the catalyst chemical composition. The improvement of the CNT crystallographic quality by employing  $H_2$  rather than  $NH_3$ , as indicated by the Raman investigations, is related to different equilibrium in the dissociation of the carbon feedstock in hydrogen and carbon containing molecules. The equilibrium of the dissociation reaction  $C_2H_2 \leftrightarrow 2C + 2H$  is shifted back by the high concentration of the reaction product  $H_2$  and then the production of carbon is slowed down. In the experimental conditions, this slowing can favour the synthesis of CNTs with enhanced quality.

On the other hand,  $NH_3$  is not a product of the feedstock dissociation and so it does not slow down the reaction. Nevertheless, its role can be to preferentially etch the amorphous carbon and to maintain the nanoparticles composition rich of N. This condition can preserve the catalyst from poisoning and further prolong the synthesis. The CNT carpet synthesized using  $NH_3$  as carrier gas was in fact thicker than that obtained with  $H_2$  one. The fact that larger CNT diameters were observed in the case of  $NH_3$  carrier gas supports the hypothesis that, in the chosen experimental CVD conditions,  $NH_3$  is more efficient in removing amorphous carbon, especially from the outer walls of the CNTs.

The duration of the deposition step has been studied. On  $Si_3N_4$  substrates at  $750\text{ }^\circ\text{C}$ , deposition times of 30 and 60 minutes have been used with a mixture of 10 %  $C_2H_2$  in  $NH_3$ , whereas duration of 5 and 30 minutes have been used with a mixture of 1 %  $C_2H_2$  in  $H_2$ . In the first case, it was found that with increasing the synthesis duration the height of the CNT carpet did not change. On the contrary, the diameters vary from 20 – 40 nm to 80 nm. The CNT growth can continue until the catalyst remains active, i.e. not covered by a carbon shield that inhibits the contact between the catalyst and the carbon feedstock. For long depositions, it is likely to poison the catalyst. Thermal cracking of the carbon feedstock gas will then occur and only amorphous carbon can be deposited, also on the CNT walls. The optimal duration depends on the synthesis conditions. If the carbon feedstock is poor or the etching is enhanced, a long synthesis process can produce a high carpet of CNTs with good quality. Otherwise if the catalytic activity of the nanoparticle is quickly inhibited, the CNT growth ends and after only amorphous carbon can be deposited on the sample. In the case of  $H_2$  process, the discussed edge effect makes difficult to obtain an unambiguous characterization of the CNT deposit. However, it is clear that the amount of carbon deposited in the 5 minutes long synthesis step is similar to that of the 30 minutes step. This indicates that the time scale of the synthesis is shorter than half an hour.

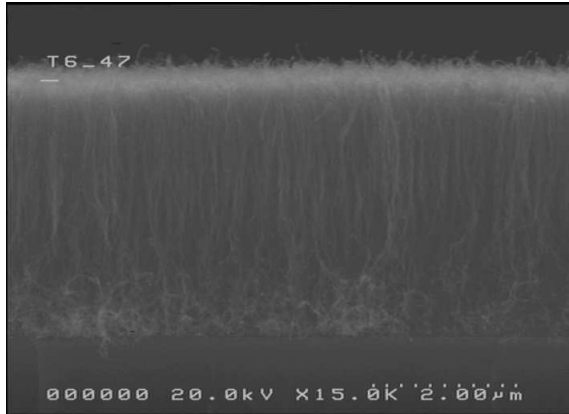


**Figure 3.14.** Cross-section SEM micrograph of a MWNT carpet grown on SiO<sub>2</sub> at 750 °C with a mixture of 5 % C<sub>2</sub>H<sub>2</sub> in NH<sub>3</sub>.

The influence of the temperature profile has been also investigated, by performing the different heating profiles available, namely the uncontrolled ramp, the controlled one and the “hot-insertion” driven by the magnet. On the SiO<sub>2</sub> substrate, the three solutions have been tested in a deposition process with CNT synthesis performed at 750 °C using a mixture of 5 % acetylene in ammonia. When the uncontrolled ramp is used, a carpet of dense vertically oriented CNTs is deposited, whose height is about of 3.6 μm and the CNT diameter varies between 20 and 40 nm (Figure 3.14). The controlled ramp process produces a 5 μm thick carpet of CNTs, whose diameters are in the range 30 – 50 nm. In the “hot-insertion” process, the annealing step duration has to be calibrated. After 5 minutes for samples introduction and temperature stabilization, the annealing step is not performed at all or lasted 10 minutes. In the former case, a 2.5 μm carpet of CNTs with 45 nm diameters has been synthesized, whereas in the latter case, the carpet is 3.3 μm high, with CNT diameters of 25 – 35 nm. The first solution is too short to allow the complete fragmentation of the catalyst film. The nickel nanoparticles result larger than those obtained in the “5 plus 10” annealing process and consequently the CNT diameters are also larger.

It is concluded that for layers such as SiO<sub>2</sub>, which exhibit good barrier layer capability against catalyst diffusion towards the silicon, a longer heating profile does not affect significantly the formation of the catalyst nanoparticles, whose dimensions only slightly increase.

Summarizing, in this first part of the work, the carbon nanotubes growth process has been studied on insulating substrates, such as SiO<sub>2</sub> and Si<sub>3</sub>N<sub>4</sub> films on silicon in order to calibrate our CVD system and to deposit carpet of long MWNTs of good crystallographic quality. Thin nickel films have been investigated as a catalyst for the growth of CNTs.

Effects of temperature, gases and heating profile have been investigated for the annealing and the deposition steps, which are both important for the CNT growth. The former determines the dimension and the chemical state of the nanoparticles of catalyst. It has been established that, in our experimental conditions, NH<sub>3</sub> is the most proper gas to be

employed, with respect to H<sub>2</sub> and Ar. The latter step determines the kinetics of the growth reaction and has to be optimized to balance the thermal cracking of the carbon feedstock gas and the etching of the amorphous carbon in order to preserve the catalytic activity of metal nanoparticles. Carbon nanotubes growth has been successfully achieved on both SiO<sub>2</sub> and Si<sub>3</sub>N<sub>4</sub> substrate.

### 3.3 Synthesis on conductive substrates

Carbon nanotubes on insulating substrates are of interest for applications such as sensors devices and for understanding the mechanisms of CNT growth, but they are not usable in applications where a direct electric contact to CNTs is required, as in the NanoChanT detector and in field emission devices. The synthesis of CNT on conductive substrates must therefore be studied and optimized.

Two different approaches have been followed. On one side, the growth of a conductive layer acting as a good barrier against catalyst diffusion towards silicon has been investigated. Based on the technical facilities available at the CNR-IMM institute and on some suggestions from the literature [98, 99], a layer of titanium nitride (TiN) has been chosen. On the other side, the nickel catalyst has been evaporated directly on the silicon substrates, in order to obtain a back ohmic contact to the CNTs. The formation of a nickel silicide layer is expected in these conditions. Depending on the phase formed at the interface this layer can be a good or a bad conductor, if a nickel rich compound is created or not, respectively.

To investigate the electrical properties of the CNTs grown on the conductive substrates, field emission measurements have been performed, since this kind of measurements do not require any direct contact to the CNT tops. These investigations will be described in the following section. To better control the field emission measurement and its effects on the CNTs, the nickel catalyst has been evaporated on the substrates through a mask which defines circular patterned area with diameters of 2.5, 0.75 and 0.5 mm.

Titanium nitride (TiN) films are commonly used in microelectronics as diffusion barriers in several multilayer metallization schemes because of their low resistivity and high thermal stability. These features perfectly fit the requirements imposed by the CVD synthesis on conductive diffusion barriers. The conductive properties and the diffusion barrier capability of TiN films are strongly dependent on their microstructural features. Hardness is reported in the range between 340 and 3000 Kgf/mm<sup>2</sup>, electrical resistivity between 18 and 10<sup>4</sup> μΩ.cm for single-phase TiN films, depending on growth conditions. Density and electrical conductivity of the film decrease if impurities, especially O<sub>2</sub>, are incorporated and if voids at the grain boundaries occur. These defects are related with deviation from stoichiometry and alteration of the lattice parameter of the film, which result in decreasing film hardness and density. Furthermore, they act as scattering centres leading to high resistivity value [100].

Three different techniques for the deposition of TiN layers are available at the CNR-IMM institute: magnetron RF sputtering from a stoichiometric TiN target; TiN formation by annealing treatment of a sputtered Ti layer in a NH<sub>3</sub> atmosphere; reactive magnetron sputtering of a Ti target in a N<sub>2</sub>/Ar atmosphere. The first solution is the cleanest one, since a stoichiometric, pure layer of TiN is deposited, without significant amount of contaminations. On the other hand, a target of such a material is very expensive and its use is not viable. The other two processes are more practicable, but they are also more affected by impurity contaminations, and so the properties of different TiN layers have to be tested for application in the particular synthesis process.

Initially, the TiN layer has been obtained by means of the NH<sub>3</sub> annealing of Ti. A 20 nm thick Ti layer has been sputtered on an n-type silicon wafer, 1 Ω.cm resistivity. Then the substrate has been annealed in an NH<sub>3</sub> atmosphere by a two-step treatment at temperatures of 400 °C and 620 °C, and finally it has been annealed at 800 °C in a N<sub>2</sub> atmosphere. On this layer a 2 nm thick nickel film evaporation followed.

A first set of processes has been made following the process described in Table 3.1, in order to compare the effect of different heating profiles. It has been observed that the TiN layer is not as efficient as SiO<sub>2</sub> or Si<sub>3</sub>N<sub>4</sub> as a barrier against the catalyst diffusion towards silicon. The best results have been achieved adopting the “hot-insertion” procedure, described in section 3.1.1. The annealing step has to be calibrated, balancing catalyst film fragmentation and the catalyst diffusion, in order to leave active nickel nanoparticles on the sample during the deposition step. Five minutes are necessary for the stabilization of the temperature after the samples introduction. Beyond that, annealing steps lasting between 0 and 20 minutes have been compared. The best results in terms of CNT quality are achieved with a 5 plus 10 minutes annealing step, giving the smallest diameters, about 60 nm. The final process is summarized in Table 3.4. Shorter annealing results in larger CNT diameters, whereas with longer annealing no evident differences are found. The CNT carpet has in every case a height of about 1 μm and a high density (Figure 3.15).

The conductive properties of the samples have been investigated by means of field emission characterization. It comes out that the Si – TiN – Ni – CNTs sandwich is not conductive. Indeed, in this configuration the TiN layer acts as a capacitor and the emission of the electrons occurs only under the applications of high voltages, which cause a breakdown in the insulating layer. This features of the titanium nitride can be explained in terms of its non-stoichiometric structure if this fabrication is adopted, which is characterized by high N and O<sub>2</sub> contaminations of the film.

| Table 3.4        |             |          |           |   |             |
|------------------|-------------|----------|-----------|---|-------------|
| Process Step     | Temperature | Pressure | Time      | Process Gas                                       |             |
|                  | (°C)        | (Torr)   | (minutes) | Gas Type  | Flow (sccm) |
| Intro            | RT          | 750      | -         | -   | -           |
| Purge            | RT          | 750      | 10        | Ar  | 1000        |
| Ramp up          | RT→750      | 750      | -         | NH <sub>3</sub>                                   |             |
| Hot-introduction | 750         | 750      | 5         | NH <sub>3</sub>                                   | 144         |
| Annealing        | 750         | 750      | 0 – 20    | NH <sub>3</sub>                                   | 144         |
| Deposition       | 750         | 750      | 30        | 5% C <sub>2</sub> H <sub>2</sub> /NH <sub>3</sub> | 8/144       |
| Cooling down     | 750→RT      | 750      | -         | Ar  | 200         |

**Table 3.4.** Synoptic description of the process employed in the investigation on the synthesis of CNTs on TiN substrates. Different annealing durations have been studied. (RT = Room Temperature; PT = Process Temperature).

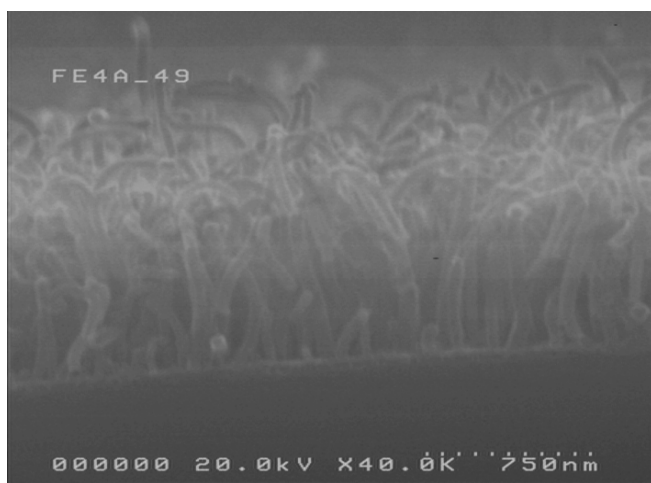


**Figure 3.15.** Cross-section SEM micrograph of a MWNT carpet grown on a TiN layer at 750 °C with a mixture of 5 % C<sub>2</sub>H<sub>2</sub> in NH<sub>3</sub> and a 10 minutes long annealing step. The TiN layer has been obtained by annealing a 20 nm thick Ti layer in NH<sub>3</sub>.

It has been consequently decided to investigate the properties of a TiN layer deposited by means of a reactive sputtering of a Ti target in a N<sub>2</sub>/Ar atmosphere. The electrical resistivity of the films deposited by means of this technique is critically influenced by the partial pressure of the N<sub>2</sub> during the TiN growth. The minimum resistivity occurs in correspondence with a N<sub>2</sub> partial pressure of about 10<sup>-4</sup> Torr [100]. The magnetron sputtering system available at the CNR-IMM institute may reach minimum N<sub>2</sub> partial pressures of 1.5 • 10<sup>-3</sup> Torr, so that an N-rich TiN is obtained.

A layer 80 nm thick has been initially deposited on a low resistivity (0.01 – 0.03 Ω.cm) silicon wafer. The resistivity of this TiN, measured by means of four points probe resistance measurements, is quite satisfactory (about 1.3 • 10<sup>3</sup> μΩ.cm). However, in the

adopted sputtering conditions, TiN conductive films having an open microcrystalline structure are deposited. Nickel diffusion through these layers turns out to be too large to allow the synthesis of CNTs, since even with the shortest annealing no active catalyst remains on the surface. A densification of the TiN crystalline structure by means of an annealing treatment in inert atmosphere of argon at 900 °C has been carried out, but the process transforms the TiN in an insulating layer. This is attributed to the high Ti reactivity to oxygen, so that the presence of some ppm of water in the Ar gas, at 900 °C, is enough to oxidize some of the Ti and form TiO<sub>2</sub> domains that degrade the conductivity.

A different solution for the densification of the TiN film has been found in the literature in terms of a sputtering deposition during which a negative voltage is applied to the substrate [98, 101]. This is expected to cause oxygen and other impurities, such as argon, to be resputtered in the atmosphere from the film. Consequently, the film exhibits a denser structure, with a less amount of voids and grain boundaries, and a larger conductivity. A slightly different solution has been adopted in the CNR-IMM magnetron sputtering system. During the Ti deposition in the reactive N<sub>2</sub>/Ar atmosphere, the substrate is heated at the temperature of 200 °C, which is the maximum temperature achievable in our magnetron sputtering system. This results in N<sub>2</sub> desorption from the N-rich TiN film, and thus in a better stoichiometry and higher density. The available magnetron sputtering system does not allow reaching temperatures above 200 °C, while the optimum density of the TiN film obtained by other authors has been achieved using temperatures of about 550 °C [100]. A 40 nm thick layer has been deposited by means of this process the film resistivity turns out to be about  $1.3 \cdot 10^3 \mu\Omega\cdot\text{cm}$ . In order to further enhance the densification of the film, an annealing process in H<sub>2</sub> atmosphere has been performed at 900 °C. The resistivity increases only slightly (up to  $1.8 \cdot 10^3 \mu\Omega\cdot\text{cm}$ ). Finally, a sample annealed in H<sub>2</sub> and a sample not annealed after the film deposition undergo a “pseudo-deposition” (with no carbon feedstock gas flow) process at 750 °C in NH<sub>3</sub> atmosphere. The sample annealed in H<sub>2</sub> has a lower resistivity with respect to the as deposited film ( $1.2 \cdot 10^3 \mu\Omega\cdot\text{cm}$  compared with  $4.6 \cdot 10^3 \mu\Omega\cdot\text{cm}$ , respectively).

On these TiN substrate samples, both the as-deposited and H<sub>2</sub> annealed ones, different thicknesses of the nickel film, ranging between 2 and 30 nm, have been evaporated in order to find the optimum thickness which allows balancing the catalyst film fragmentation and the catalyst diffusion through the barrier layer. Very thick films result in poor film fragmentation and nanoparticles formation whereas too thin layers results in lack of active catalyst on the sample surface during the deposition step.

A CVD process has been performed following the steps of Table 3.4, with a annealing of 10 minutes. The best thickness for the nickel film is 30 nm. However, the film is composed by defective CNTs, with different heights (up to 4.5 μm) and often covered by a thick layer of amorphous carbon. The CNT diameters are very large and broadly distributed, varying between 90 and 250 nm. The density is consequently low. This deposit

has been characterized by means of field emission measurements. As it will be described in detail in next section, the measurements established that the Si – TiN – Ni – CNTs sandwich is conductive. The slightly conductivity increase provided by the H<sub>2</sub> annealing is not sufficient to justify the enhanced complication of the process including this additional step, thus it has been skipped in the following investigations.

The CVD synthesis process has been modified in order to investigate the effect of low pressure conditions during the annealing and the deposition steps. Following the process of Table 3.4, a reduced pressure of 10 Torr has been maintained during these steps. The quality of the sample dramatically improves. A dense carpet of multi-walls CNTs was deposited. The mean thickness was about 5 μm, but few isolated nanotubes up to 20 μm long have been also observed (Figure 3.16). The sample exhibited CNTs with a broad diameter distribution, ranging between 20 and 100 nm. Some CNTs showed nickel clusters distributed along their length.

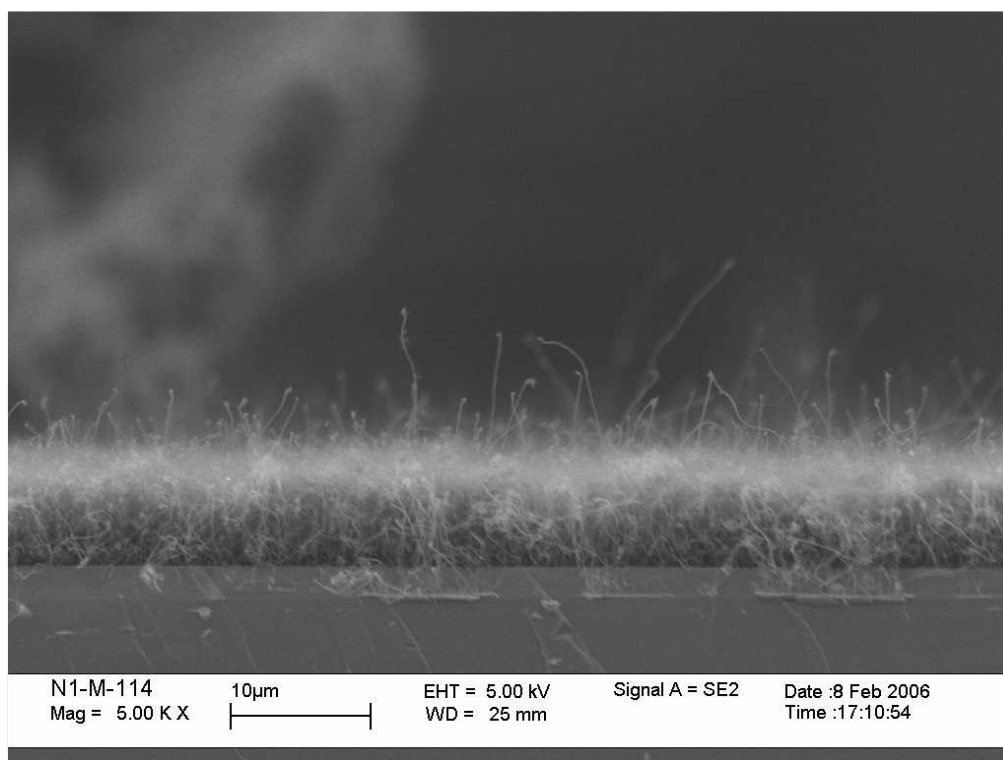


**Figure 3.16.** Cross-section SEM micrograph of a MWNT carpet grown on a TiN layer following the process defined in Table 3.4, but at low pressure (10 Torr) The TiN layer, 40 nm thick, has been obtained by RF magnetron sputtering of Ti in reactive atmosphere of N<sub>2</sub>/Ar, with the substrate hold at 200 °C.

Raman investigation confirms the enhancement of the CNT quality. In Figure 3.17, the Raman spectrum of the sample deposited at 750 Torr is compared with the spectrum of a CNT film deposited at 10 Torr. In both the spectra the D peak intensity is high, indicating that the samples contain amorphous carbon and defective nanotubes. The ratio between the defective peak and the graphite one,  $I_D/I_G$ , is about 1.3 in both spectra, in agreement with values reported in the literature for films of CNTs coated with amorphous carbon [97]. Actually, in the low pressure sample this ratio is slightly greater with respect to the atmospheric pressure sample (1.39 compared with 1.26), but the equally significant width of the peak is much smaller in the latter case. Finally, the ratios  $I_D/I_{G'}$  and  $I_G/I_{G'}$ , between the defective peak or the first resonant order peak,  $I_D$  and  $I_G$  respectively, and the second resonant peak of graphite,  $I_{G'}$ , largely decrease for the Raman spectrum of the sample deposited at 10 Torr, indicating a lower number of defects in the corresponding CNTs [97].

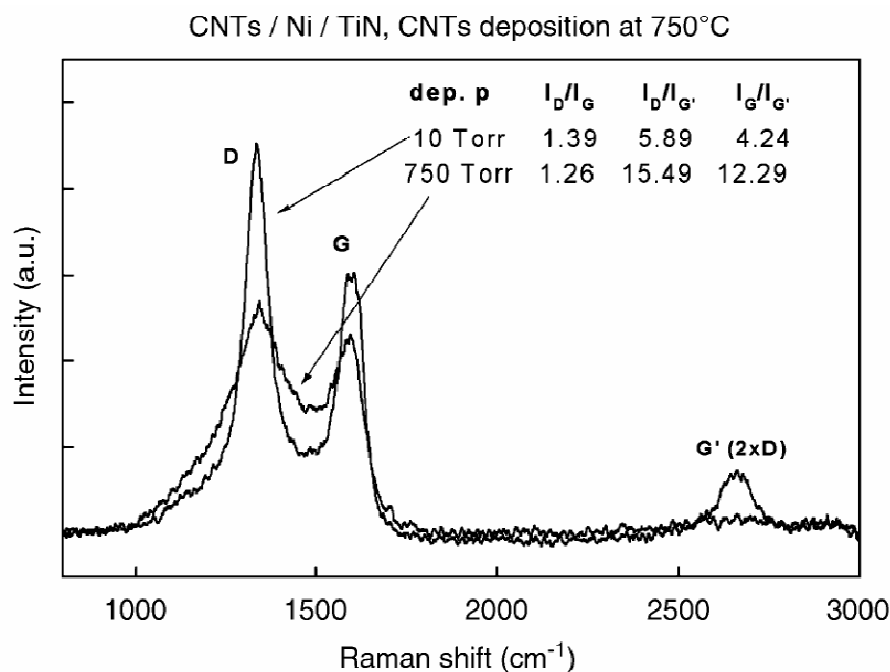


**Figure 3.17.** Raman spectra in the range 1000–3000  $\text{cm}^{-1}$  of the CNT carpets grown on the sputtered TiN, following the process of Table 3.4, at two different pressures (750 and 10 Torr). The TiN layer has been deposited holding the substrate at 200 °C.

The second approach adopted in order to investigate the CNT synthesis on conductive substrates has included an evaporation of the nickel catalyst film directly on silicon substrates. An n-type, low resistivity (0.5 – 1  $\Omega$ .cm), silicon substrate has been used. Various thicknesses, between 2 and 30 nm, of the nickel film have been evaporated. A nickel silicide is expected to form at the interface, due to the nickel diffusion inside the silicon substrate. Depending on phase created at the interface, the silicide can be conductive or not.

CVD processes performed in a mixture of 5 %  $C_2H_2$  in  $NH_3$ , at atmospheric pressure, result in unsatisfactory CNT deposits when the temperature profile causes a large diffusion of nickel inside the silicon, as in the case of long annealing steps or deposition temperatures of 900 °C. On the other hand, CNTs have been deposited adopting the process described in Table 3.4, with a 10 minutes long annealing step. The nickel film thickness of 5 nm thick produces the best CNT carpet, 10.3  $\mu$ m high (Figure 3.18). The SEM images show CNTs of high quality, with few defects, and with diameters in the range 60 and 80 nm. The resistivity of the nickel silicide has not been measured directly but only by means of the field emission technique, as in the case of CNT growths on the TiN substrates. The Si – Ni – CNTs sandwich results to be insulating, as described in the following, indicating that the  $Ni_xSi_y$  phase, formed during the CVD process, is not conductive.

Summarizing, the synthesis of CNTs has been investigated on silicon and on titanium nitride layers produced by means of different methods in order to determine the optimum solution for a conductive layer on which CNTs can be successfully grown. First, a proper deposition technique for a conductive TiN layer which acts as a barrier layer has been determined. Then, CNT carpets of satisfactory quality have been deposited on both substrates. This achievement allows to perform a field emission characterization of the different configurations for the Si – CNTs interface, and hence to determine the solution to be employed in the NanoChanT detector.

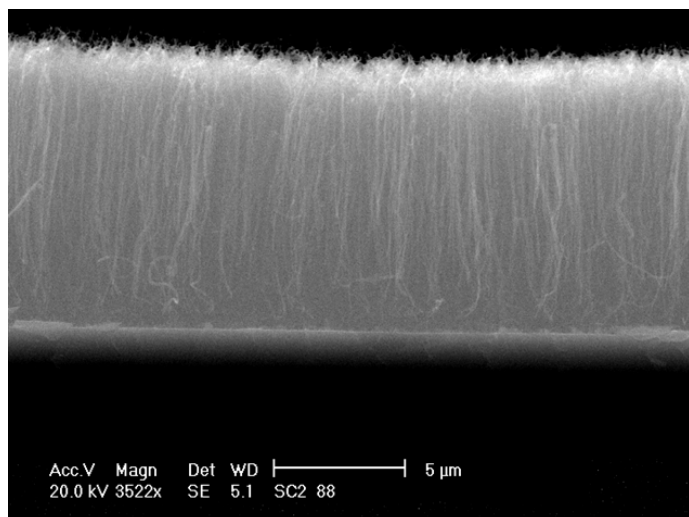


**Figure 3.18.** Cross-section SEM micrograph of a MWNT carpet grown on a 5 nm thick Ni film directly evaporated on Si. The growth process has been performed in accordance with Table 3.4

## 3.4 Field emission characterization

The conductivity of the interfaces between the barrier layers and the CNTs has been evaluated by means of field emission measurements. This approach has been chosen mainly for two reasons. Firstly, it allows the characterization of the different barrier layers with CNTs grown in a free-standing configuration and without a top contact on the CNTs, which is not trivial. Indeed, contact I–V measurements require the growth of CNTs in dedicated configurations and the definition of a proper metallization scheme for the direct contact between the top of the CNT carpet and the upper electrode. However, field emission properties are very much affected by the sample morphologies so that it is not possible to deduce quantitative values of the conductivity of the sandwich barrier layer – catalyst – CNTs, since different CNTs morphologies have been obtained on the different samples. Nevertheless, a qualitative indication can be traced and it is useful in establishing what is the proper barrier layer. Secondly, CNTs are deeply investigated as field emitters since their structural and morphological properties make them appealing for being used in cold cathode emitter devices for intense electron sources. This approach can also allow to achieve some insights on the field emission properties of the CNTs grown.

### 3.4.1 Field emission system

The field emission system is placed inside a stainless steel chamber (Figure 3.19), equipped with a pumping system. This consists of a scroll pump and a turbo-molecular pump which allow achieving a vacuum level of  $10^{-7} - 10^{-8}$  Torr.

A Keithley Source Meter 2410 is used as power supply to establish a voltage difference between the electrodes in the range 0 – 1100 V. A Keithley 619 multimeter records the emitted current. The system has been designed in order to allow the flow of a maximum current of 1  $\mu$ A and to have a very low current noise, namely of about 1 – 2 pA. The electrodes configuration is composed by a spherical anode and a flat cathode. The former consists of a gold tip, with a diameter of 520  $\mu$ m. The latter is a grounded aluminium base (Figure 3.19). The samples are attached by means of silver paste from the back side at an aluminium plate, which is then mechanically contacted with the cathode base. The cathode can move in the XY plane being driven by two independent piezoelectric motors. The minimum step is approximately 10  $\mu$ m and the maximum displacement is 25 mm.

Two additional piezoelectric motors control the anode position along the Z axis, and thus the anode–cathode distance. One motor is similar to those of the XY plane. The second motor allows a more precise displacement of the anode, nominally of approximately 10 nm. The extension range for this piezoelectric motor is limited at 90  $\mu$ m.

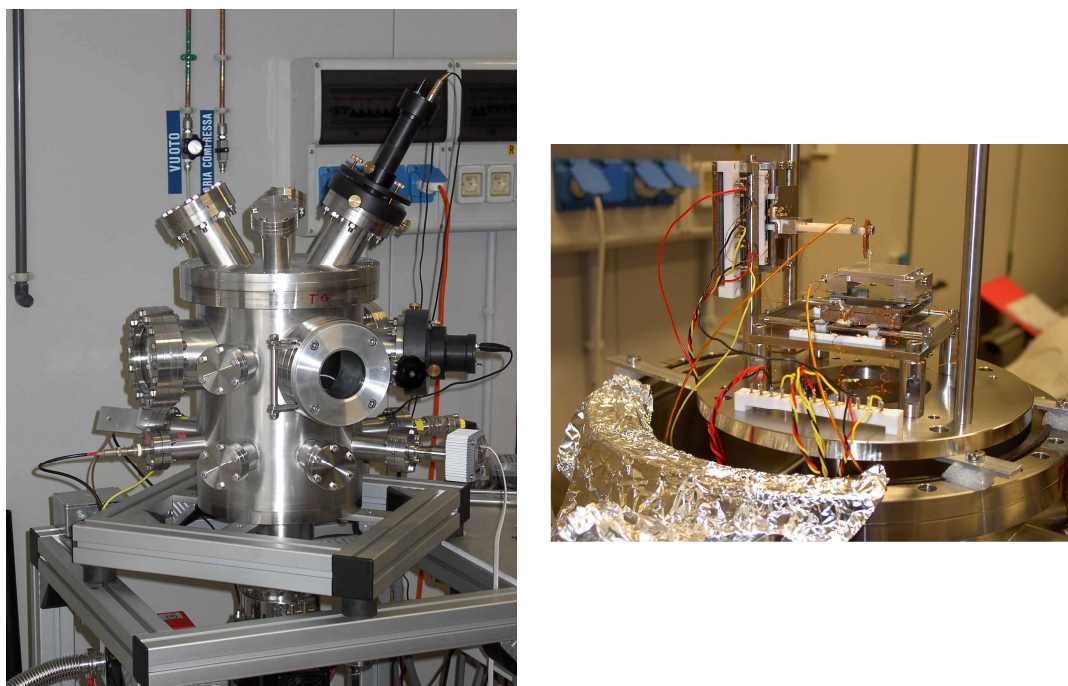


**Figure 3.19.** Picture of the Field Emission system. On the left, the stainless chamber which contains the sample to be characterized. On the right the core of the system: the anode tip is sustained by the white bar, which moves along the Z axis. The sample is attached at the base, which can move in the XY plane. Piezoelectric motors drive the system in the XYZ space.

Since an accurate knowledge of the anode–cathode separation is critical in field emission measurements, a procedure that permits to directly determine the electrodes distance has been developed. In this procedure, the anode is moved downwards to the cathode until a direct contact is found. The Keithley multimeter is set as an ohmmeter to protect the electronics of system in this configuration. A voltage of 3 V is imposed between the electrodes, and the contact between anode and cathode is established when a current is detected. Since the system can be moved only by discrete steps, cautions must be taken in order to avoid too large displacements that could result in damaging the sample surface. Both the piezoelectric motors controlling the Z axis are used to overcome this risk. Firstly, the fine piezoelectric motor is used to probe the space from the starting position of the anode to the maximum extension of the piezo. If the contact is not reached, the fine piezo is pulled back and the second piezoelectric motor, which has a minor step resolution, moves the anode. This displacement puts downwards the new starting position of the anode, but within the already probed space. The process then restarts, until the contact between the electrodes is established. This routine allows to probe new Z positions only with the small steps of the fine piezoelectric motor, which can be set down to 10 nm. It has been verified by means of SEM observations that the adopted procedure does not cause detectable damages on the surface of the measured samples. After the reference 0 position

has been set, measurements are performed at an anode–cathode separation within the residual space between the complete contraction of the finer piezo and its extension corresponding to the 0 position. The theoretical maximum working distance is thus the largest extension of the piezo, that is 90  $\mu\text{m}$ , but real maximum values can be only 70 – 80  $\mu\text{m}$ .

Field emission data are collected imposing a scanning over a voltage range after the desired anode–cathode separation has been set. All the movements and the measurements of the system are controlled via PC. The external electrical field has been approximated as the ratio between the applied voltage and the minimum distance between the spherical anode and the planar cathode.

### 3.4.2 *Field emission measurements*

#### **Field emission characterizations of reference samples**

In order to compare different samples, two reference figure-of-merits have been chosen, namely the applied electric fields required for collecting a current of 100 pA and 1  $\mu\text{A}$ . Respectively, the former value has been chosen well above the instrument current noise of 1 – 2 pA, the latter value corresponds to the maximum current allowed in the system. Two different samples were initially characterized in order to gain some references for the subsequent measurements.

Dense carpets of vertically oriented CNTs synthesized on a thin silicon dioxide layer (9 nm thick) with patterned catalyst areas, are employed as a reference for measurements on insulating barrier layer (already shown in Figure 3.14). By applying electric fields up to high values, the emitted current remains within the noise range, being about 1 pA. Suddenly, the current raises to the maximum allowed value of 1  $\mu\text{A}$ . This step in emission occurs at different values of the electric field, ranging between 45 and 70  $\text{V}/\mu\text{m}$  in different measured sites. Further measurements in the same location showed that 1  $\mu\text{A}$  is reached at much lower values, i.e. between 13 and 20  $\text{V}/\mu\text{m}$ , with a more gradual rising between the two limit values. The field required for achieving 100 pA current then varies between 10 and 15  $\text{V}/\mu\text{m}$ . Moreover, the I–V profile turns out to be quite reproducible.

For achieving the high electric fields required by this sample it has been necessary to work at small anode–cathode separation, namely 10  $\mu\text{m}$ . These small inter-electrodes separations increase the risk of damages of the cathode surface induced by arcing or short-circuits between anode and some CNT protrusions. When this arcing occurs, the sample undergoes the localized flow of the maximum current until the voltage scanning is not completed. The presence of CNTs can eventually cause local field amplification at their tips by means of their enhancement factor  $\beta$  and allow reaching the electric fields required for arcing, i.e. about some  $\text{kV}/\mu\text{m}$ . SEM investigations evidence a break in the CNT film, in all the measured sites, as it has been pushed upwards by some kind of explosion. A

silicon droplet is always found in the middle of the film cracks. The sudden current emission has been related to an arc-shocking process and a subsequent silicon substrate melting. After this, a conductive path is created and the molten silicon acts itself as field emitter.

The second reference sample consists of a 20  $\mu\text{m}$  thick dense carpet of vertically oriented CNTs on a conductive substrate. It was synthesized at 700  $^{\circ}\text{C}$  and atmospheric pressure directly on a silicon substrate, using a 2 nm thick Fe layer as catalyst and a mixture of 5 %  $\text{C}_2\text{H}_2$  in Ar. This particular process was adopted on the base of a process reported in the literature for field emission application [40]. Differently from the previous case, the collected I–V measurements are quite reproducible during the first and the subsequent voltage scanning, even if the I–V profiles are quite noisy. The fields required for achieving currents of 100 pA and 1  $\mu\text{A}$  are 6 – 8 V/ $\mu\text{m}$  and 9 – 12 V/ $\mu\text{m}$ , respectively. These values are considerably smaller with respect to those obtained on the silicon dioxide substrate, and the emission curve is smooth. These results are confirmed at different anode–cathode separations, ranging between 10 and 80  $\mu\text{m}$ . The applied fields required for extracting the reference currents decrease with larger anode–cathode separation, since the farther is the anode tip, the wider is the area on which the electric field insists on. Field emission is indeed dominated by few best emitters and at larger anode–cathode distances, the probability of including their contribution in the total emitted current the contribution is larger. Furthermore, if a larger area undergoes the application of the electric field, a more stable emission curve will be also measured, since the CNT distribution will be more homogeneous. SEM investigations of the sample after the field emission measurements reveal that CNTs rise in blocks of some micrometres, due to a poor mechanical bonding between the CNT carpet and the silicon substrate. This poor CNTs-substrate adherence is considered the cause of the noisy I-V profile.

The field emission profile of the CNT carpet grown on the thin silicon dioxide was thus adopted as a reference for the behaviour of sample on a poor conductive or insulating barrier layer substrates, whereas the field emission profile of the CNT carpet grown directly on silicon, using Fe as catalyst, was considered as a reference sample whose field emission behaviour indicates a good electrical contact between CNTs and the substrates.

### **Field emission measurements on CNTs grown on conductive barrier layer**

The field emission characterization allowed establishing the interface conductivity of the CNTs samples grown on nickel catalyst evaporated directly on silicon or on titanium nitride layers.

The best CNT carpet grown on Ni/Silicon substrate (already shown in Figure 3.18) has been measured. The results have been similar to those of the thin silicon dioxide reference sample. The first achievement of the maximum current of 1  $\mu\text{A}$  has a steep profile and occurs between 65 and 80 V/ $\mu\text{m}$ . The fields for extracting 100 pA and 1  $\mu\text{A}$

obtained in the following measurements are 8 and 12 V/ $\mu\text{m}$  respectively (Figure 3.20). The Si – Ni – CNTs structure is insulating evidencing that the  $\text{Ni}_x\text{Si}_y$  phase of the Ni silicide, formed during CNT growth process, is not conductive.

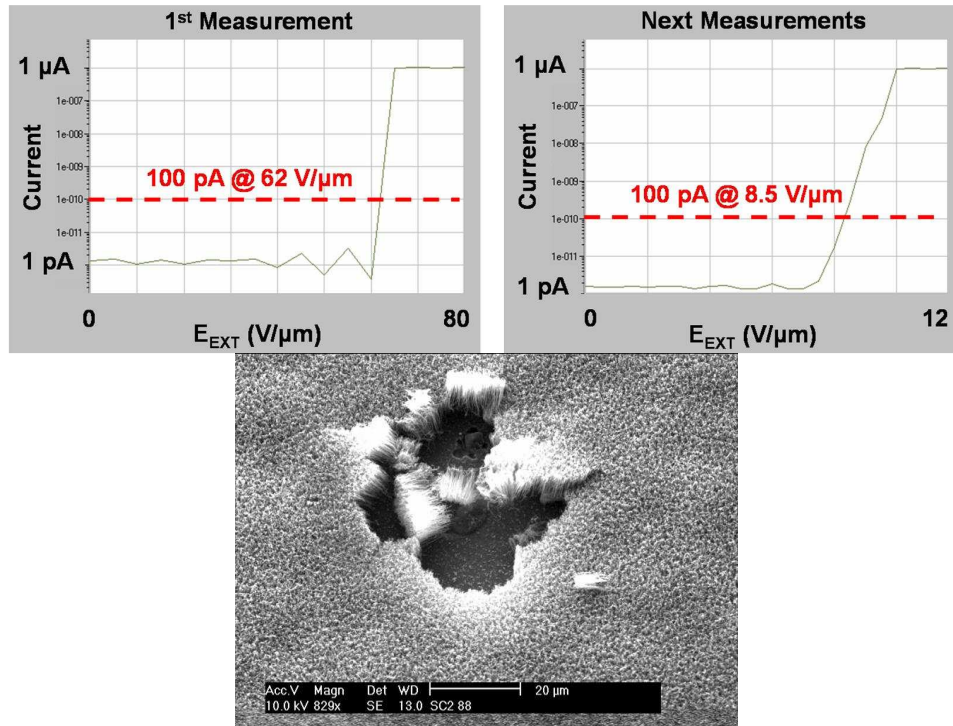


**Figure 3.20.** Field emission behaviour of the CNT carpet grown on Ni/Si at 750 °C (see Figure 18). The first emission (upper left) is abrupt and occurs at high fields (60 – 80 V/ $\mu\text{m}$ ). The subsequent ones are smoother and at lower field (8 – 12 V/ $\mu\text{m}$ ). After the emission, the CNT carpet results detached and a silicon molten droplet can be seen at the centre of the emission site.

Field emission characterizations have also supported the investigation on the different TiN layers. The TiN barrier layer prepared by means of  $\text{N}_2$  annealing of a 20 nm thick Ti layer has been discarded because the CNT carpets grown on this kind of substrate present the field emission behaviour of the reference insulating substrate.

On the other hand, conductive TiN barrier layer has been obtained by means of a Ti sputtering in reactive  $\text{N}_2/\text{Ar}$  atmosphere with the substrate heated at 200 °C. Field emission measurements allow checking if also the Si – TiN – Ni – CNTs structure maintained good electrical conductivity. The CNT film deposited at atmospheric pressure has been characterized.

The field emission properties of this sample evidence a conductive feature of the interfaces. No large difference occurs between the first and the subsequent current emission curves. The reference currents of 100 pA and 1  $\mu\text{A}$  are collected for fields of 9 – 12 V/ $\mu\text{m}$  and 13 – 16 V/ $\mu\text{m}$  respectively, when the anode–cathode separation is 50  $\mu\text{m}$ .

SEM observations do not reveal any breakdown in the film, as expected. The stability of the current emission has been demonstrated over a 20 minutes long measurement with a proper applied field set to collect approximately 300 pA.

Even better field emission performances have been found on the CNTs synthesized on the same substrate at reduced pressure (shown in Figure 3.16). This enhancement was expected since the morphology of this sample is more suitable for this kind of application. Indeed, the few isolated 20  $\mu\text{m}$  long CNTs extruding from the dense film, having a mean thickness of about 5  $\mu\text{m}$ , likely act as preferential emission site, since they do not suffer any screening effect. The electric fields applied to collect the reference currents are the lowest ones among the measured samples. For measuring a current of 100 pA a field ranging between 2.8 and 4.5  $\text{V}/\mu\text{m}$  is necessary, and for 1  $\mu\text{A}$  between 4 and 6.6  $\text{V}/\mu\text{m}$ , when collected at an anode–cathode distance of 50  $\mu\text{m}$  (Figure 3.21). Moreover, SEM observations do not reveal any breakdown in the film, as expected, nor modifications in the CNT carpet morphology.

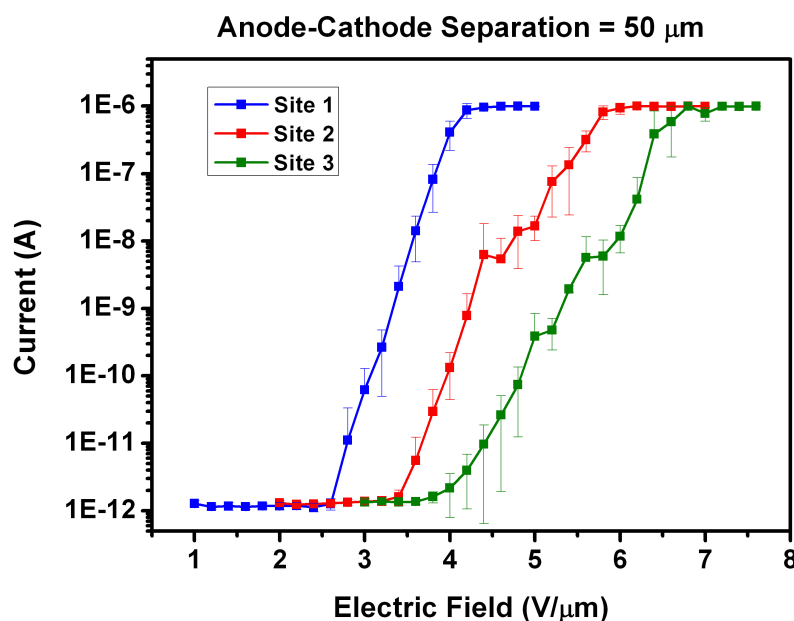


**Figure 3.21.** Field emission behaviour of the CNT carpet shown in Figure 3.16. The reference fields are the smallest obtained: 100 pA are collected at fields of 2.8 – 4.5  $\text{V}/\mu\text{m}$ , and 1  $\mu\text{A}$  at 4 – 6.6  $\text{V}/\mu\text{m}$ . The different curves are related to different emission sites on the sample, and are due to the local morphology of the sample.

The field emission measurements allow the determination of the best barrier layer to be adopted as interface between CNTs and silicon. Furthermore, it is worth noting that this sample is very interesting since it could be used to extract large electron currents by means of the application of relatively small electric fields.

However, as discussed in Chapter 2, for rating the quality of different cold cathode field emitters, it is necessary to compare the current density  $J$  achievable under the application of an electric field  $E$ . Moreover, this approach is needed when looking for physical insights of the emission phenomenon. Since the experimental curves involve an I–V relationship, it is mandatory to estimate the emission area  $S$  which provides the collected current. This problem is particularly critical when arrays or films of emitters are measured and a sphere–to–plane geometry is adopted for the anode–cathode system. In many papers the emission area is extrapolated from the Fowler–Nordheim plot, but such an “emission area” is not useful in characterizing an actual field emission device and its nature is still hardly understood. Mainly, other papers tacitly avoid or underestimate the issue of emission area calculation. As already shown (see Figure 2.12), different evaluations of this entity can result in a very wide range of  $J$  values.

### Field emission measurements interpretation

After having studied the interfaces between CNTs and silicon by means of field emission, a procedure for interpreting the I–V measurements has been developed, in order to characterize the CNT films grown on conductive TiN as cold cathode field emitters.

Since the Fowler–Nordheim (FN) equation (2.1) links the locally defined electric field  $E_{LOC}$  and current density  $J$ , a modified version of the equation, linking the applied voltage  $V$  and total current  $I$  collected at the anode has to be built. The local field  $E_{LOC}$  can be expressed as the externally applied electrical field  $E_{EXT}$  ( $E$  for sake of simplicity in the following) multiplied by the geometrical factor  $\beta$ , the field enhancement factor. That is

$$E_{LOC} = \beta \times E_{EXT} \quad (3.3)$$

The factor  $\beta$  is locally defined since it depends strongly both on the single field emitter geometry and structure (i.e. from the presence of adsorbates) and on the film density, as described in section 2.1.3. For the characterization of a device based on a field emitters film, it is not practical and neither useful to manage directly the local field enhancement factor. It is more convenient to consider the  $\beta$  factor as the average of the  $\beta(\mathbf{r})$  of the different emitters, which describes a “device feature”. This assumption is justified by the fact that the CNT samples are quite homogenous in a scale of some tens of microns, even if they are very variable on a shorter scale (see Figure 3.16).

The field emission phenomenon is very much affected by small variation of the external field  $E$ , due to the exponential dependence of  $J$  on  $E$ . In the sphere-to-plane geometry,  $E$  decreases when moving from the point of minimum electrodes distance, as illustrated in Figure 3.22. The correspondent dependence of  $J$  with respect to  $r$  is also reported.

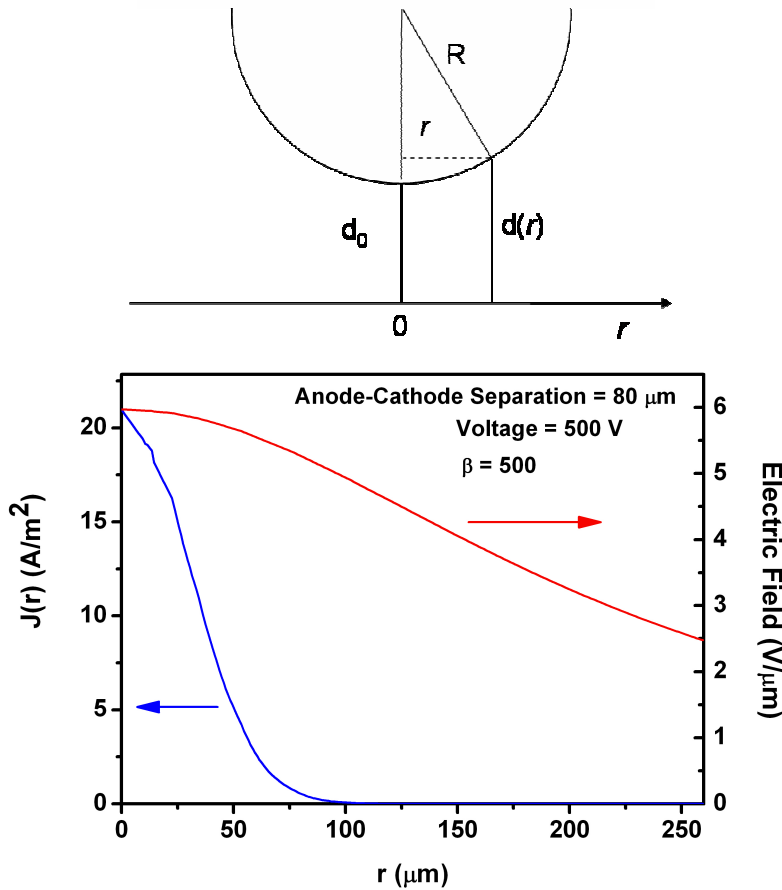


**Figure 3.22.** (Above) Scheme of the sphere-to-plane configuration for the electrodes.  $R$  is the tip radius,  $d_0$  the minimum distance,  $r$  the distance on the plane from 0. (Below) Simulation of the electrical field vs.  $r$ . The dependence of the current density  $J$  on  $r$  is also shown. The simulation has been made with an applied voltage of 500 V, an inter-electrodes separation of 80  $\mu\text{m}$ , and assuming a typical value of 500 for the enhancement factor.

In the adopted configuration, the actual electric field exerted on the cathode surface has been approximated as  $E = \frac{V}{d(\mathbf{r})}$ . Due to the cylindrical symmetry, the anode-cathode distance  $d(\mathbf{r})$  depends only on  $r$  and it can be expressed as

$$d(r) = d_0 + \Delta d(r) = d_0 + R - \sqrt{R^2 - r^2} \quad (3.4)$$

where  $R$  is the anode radius (equal to 260  $\mu\text{m}$ , in the employed system), and  $d_0$  is the minimum anode–cathode distance.

The Fowler–Nordheim equation can be thus rewritten as

$$J(E_{LOC}) = \frac{AE_{LOC}^2}{\phi} e^{-\frac{B\phi^{3/2}}{E_{LOC}}} \cong J(V) = \frac{A}{\phi} \times \left( \frac{\beta V}{d_0 + R - \sqrt{R^2 - r^2}} \right)^2 e^{-B\phi^{3/2} \times \frac{(d_0 + R - \sqrt{R^2 - r^2})}{\beta V}} \quad (3.5)$$

where  $A = 1.54 \cdot 10^{-6} \text{ A eV V}^{-2}$ ,  $B = 6.83 \cdot 10^9 \text{ eV}^{-3/2} \text{ V m}^{-1}$  and  $\phi$  is the work function of the emitter. For CNTs, a  $\phi$  value of 5 eV is commonly used. The final form of the FN equation is then

$$J(V) = J(V, r) = A' \times \left( \frac{\beta V}{d_0 + R - \sqrt{R^2 - r^2}} \right)^2 e^{-B' \times \frac{(d_0 + R - \sqrt{R^2 - r^2})}{\beta V}} \quad (3.6)$$

where  $A' = \frac{A}{\phi} = 3.08 \cdot 10^{-7} \text{ A V}^{-2}$  and  $B' = B\phi^{3/2} = 7.64 \cdot 10^{10} \text{ V m}^{-1}$ .

To make explicit the total emitted current  $I$ , the equation (3.6) has to be integrated over the cathode surface, that is

$$I(V) = \int_0^{\infty} 2\pi r J(V, r) dr \quad (3.7)$$

Because of the quick decrease of  $J = J(r)$ , as shown in Figure 3.22, it is possible to integrate up to  $R$  as an upper limit, which is also the limit of definition for the approximation of  $E = \frac{V}{d(r)}$ . The solution of this integral is

$$I(V) = c_1 e^{c_2 c_3} \left\{ c_3 \left[ \frac{e^{-c_2(c_3 - R)}}{c_3 - R} - \frac{e^{-c_2 c_3}}{c_3} \right] + (1 + c_2 c_3) [E_1(c_2 c_3) - E_1(c_2(c_3 - R))] \right\} \quad (3.8)$$

The explicit expressions of the constants used in (3.8) are

$$c_1 = 2\pi A' \beta^2 V^2 e^{-\frac{B'(d_0 + R)}{\beta V}} \quad (3.9)$$

$$c_2 = \frac{B'}{\beta V} \quad (3.10)$$

$$c_3 = d_0 + R \quad (3.11)$$

The function  $E_1(z)$  is the exponential integral function, defined as  $E_1(z) = \int_z^{+\infty} \frac{e^{-t}}{t} dt$  for  $|\arg(z)| < \pi$ . This function can be asymptotically approximated, for  $|\arg(z)| < \frac{3}{2}\pi$  [102], with

$$E_1(z) \approx \frac{e^{-z}}{z} \left\{ 1 - \frac{n}{z} + \frac{n(n+1)}{z^2} + o(z^3) \right\} \quad (3.12)$$

To accomplish the calculation an approximation at the second expansion term is needed. For  $z > 10$ , as in our case, the error for such an approximation is of less than 2 %.

The final result is thus

$$I(V) = \frac{c_1 R}{c_2 d_0^2} e^{c_2 R} = \frac{2\pi A' R \beta^3 V^3}{B' d_0^2} e^{\frac{B' d_0}{\beta V}} = C \beta^3 V^3 e^{\frac{D}{\beta V}} \quad (3.13)$$

where

$$C = \frac{2\pi A' R}{B' d_0^2} \quad (3.14)$$

$$D = B' d_0 \quad (3.15)$$

Both  $C$  and  $D$  are constant, assuming that  $R$ ,  $d_0$  and the work function  $\phi$  are fixed. By means of fitting the experimental data with equation (3.13) it is possible to calculate the field enhancement factor  $\beta$ . From equation (3.13), it would be also theoretically possible to determine the work function  $\phi$ , but this approach is only possible for single emitter configurations [63]. In fact, for a film, the influence of both close emitters and substrate results in unreliably low values of 0.5–2 eV [103].

A similar method for analyzing field emission data in a sphere-to-plane electrode configuration has been developed by other authors [104]. In their approach a different solution of the same integral (3.7) was achieved, based on a first-order Taylor expansion of the integrand function. Their final result is

$$I(V) = C'V^3 \left(1 - \frac{2V}{D'}\right) e^{-\frac{D'}{V}} \quad (3.16)$$

where  $C'$  and  $D'$  differ from (3.14) and (3.15) because they include also the parameter  $\beta$ . That is,

$$C' = \frac{2\pi A' R \beta^3}{B' d_0^2} \quad (3.17)$$

$$D' = \frac{B' d_0}{\beta} \quad (3.18)$$

The equation (3.16) is rewritten as

$$I(V) = J(0) \left( \frac{2\pi d_0 R V}{D'} \right) \left(1 - \frac{2V}{D'}\right) = J(0) A_{eff} \quad (3.19)$$

being  $J(0)$  the current density at  $r = 0$  and  $A_{eff}$  the corresponding effective emitting area. It has to be noted that being  $J(0)$  the maximum value for the current density over the sample area (as can be seen in equation (3.5)), the  $A_{eff}$  slightly underestimates the actual emission area.

It is worth noting that both approaches lead to a modified version of the FN relationship for a sphere-to-plane configuration, where the dependence of  $I$  is on  $V^3$  and no more on  $V^2$ . The two *modi operandi* differ only by a corrective factor, dependent on  $V$  and negligible for high  $D'$  values. The usually adopted FN plot, where the experimental data are shown in the  $\left(\frac{1}{V}, \ln\left(\frac{I}{V^2}\right)\right)$  plane in order to obtain a linear representation of the

field emission phenomenon, has to be replaced by a modified one, where  $\left(\frac{1}{V}, \ln\left(\frac{I}{V^3}\right)\right)$  is used.

After  $\beta$  has been estimated from fitting the experimental data with (3.13), we achieve the evaluation of the emission area with two different methods. Firstly, fixed the voltage and the anode-cathode separation, the dependence of the collected current with respect to the radial distance from the symmetry axis has been considered. The emission area has been evaluated as the cathode area contributing at a determined fraction of the total current  $I$ . Secondly, the approach reported in [104] has been applied at equation (3.13) for comparison, obtaining

$$I(V) = J(0) \left( \frac{2\pi R \beta V}{B'} \right) = J(0) A_{eff} \quad (3.20)$$

The developed framework has been applied at different emission sites of the CNT carpet shown in Figure 3.16. The fitting procedure is affected by the regularity of the I–V profile. Field emission is very much affected by local variation of the sample, due to contaminations from adsorbates, exceptionally long emitters or others, whose effects can change during the emission. The deviations from the expected trend can be related to these changes. It is thus extremely important to achieve stable emissions. Conditioning treatments, which consist in forcing for several hours a medium current emission through the sample, are commonly adopted to reach this condition. Better results have been obtained when the emission is more stable, as in Figure 3.23. The experimental fit of the I–V data with equation (3.13) has been performed by means of a nonlinear regression method based on the Leverberg-Marquardt (LM) algorithm [105].

The field enhancement factor is estimated as  $\beta = 796.6 \pm 0.5$ . The result, reported in Figure 3.24, is quite good considering that only few significant experimental points have been available for the fitting, after excluding the noise current and the current-limited zones. The effective emission area  $A_{eff}$  is evaluated for the experimental data point  $(V, I) = (200 \text{ V}, 4.095 \cdot 10^{-7} \text{ A})$ . From the equation (3.20), this results in

$$A_{eff} = \left( \frac{2\pi R \beta V}{B'} \right) \Big|_{V=200V, \beta=796.6 \pm 0.5} = (3.407 \pm 0.002) \cdot 10^{-5} \text{ cm}^2 \quad (3.21)$$

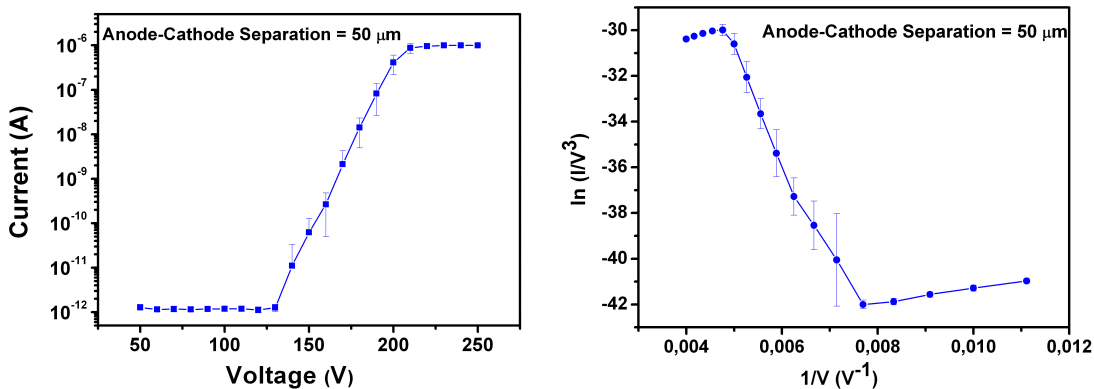


**Figure 3.23.** Field emission behaviour of the CNT carpet shown in Figure 3.16. On the left, the I–V plot is shown. On the right, the modified Fowler-Nordheim plot,  $\ln\left(\frac{I}{V^3}\right) \text{ vs } \frac{1}{V}$ , is used. In this plot the field emission behaviour is represented by a straight line. In both graphs, the experimental data points which follow a field emission behaviour are between the current noise region (1 pA) and the region where the emitted current has been limited by the protection circuitry at 1 μA.

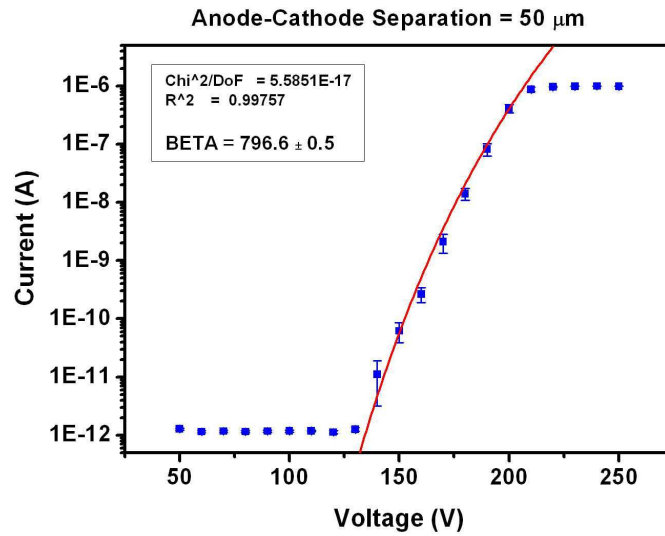


**Figure 3.24.** The result of the experimental data fitting with equation (3.3).

On the other side, by evaluating the function  $\frac{dI}{dr}(r)$ , the areas corresponding to different fractions of the total collected current can be determined (Figure 3.25). The results corresponding to the set of parameters  $(d_0, V, \beta) = (50 \mu\text{m}, 200 \text{ V}, 797)$  are reported in Table 3.5. The emission area contributing at 95 % of the total current  $I$  has been estimated as  $A_{SIM} \approx 9.5 \cdot 10^{-5} \text{ cm}^2$ . It has to be noted that the simulated total current differs only slightly from the measured one ( $I_{SIMULATED} \approx 3.833 \cdot 10^{-7} \text{ A}$  vs.  $I_{MEASURED} \approx 4.095 \cdot 10^{-7} \text{ A}$ ), validating the framework.

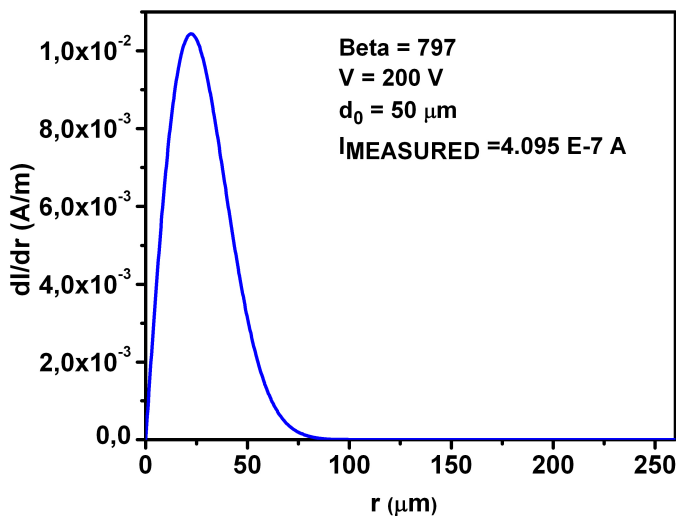


**Figure 3.25.** Simulation of the emitted current distribution with respect to the radial distance from the point of minimum anode-cathode separation. The integral of the function, calculated with the set of parameters  $(d_0, V, \beta) = (50 \mu\text{m}, 200 \text{ V}, 797)$ , gives the total emitted current.

| Table 3.5                                       |                     |                                   |
|---|---------------------|-----------------------------------|
| Total Integral Current = $3.83 \cdot 10^{-7}$ A |                     |                                   |
| Fraction of the total current (%)               | R ( $\mu\text{m}$ ) | Collecting Area ( $\text{cm}^2$ ) |
| 95  | 55                  | $9.50 \cdot 10^{-5}$              |
| 98  | 62                  | $1.21 \cdot 10^{-4}$              |
| 99  | 67                  | $1.41 \cdot 10^{-4}$              |

**Table 3.5.** Summary of the simulation on the area of the sample that contributes for a given fraction at the total emitted current.

The current density has been finally evaluated with the emitting areas calculated with the two methods, that is  $A_{SIM} \approx 9.5 \cdot 10^{-5} \text{ cm}^2$  and  $A_{eff} = 3.4 \cdot 10^{-5} \text{ cm}^2$  (from 3.21). For a collected current of  $4.095 \cdot 10^{-7}$  A,

$$\begin{cases} A_{eff} = 3.407 \cdot 10^{-5} \text{ cm}^2 \Rightarrow J_1 = 12 \text{ mA/cm}^2 \\ A_{SIM} = 9.50 \cdot 10^{-5} \text{ cm}^2 \Rightarrow J_2 = 4.3 \text{ mA/cm}^2 \end{cases}$$

The CNT carpet grown on conductive TiN at 10 Torr results able to emit a current density of some  $\text{mA/cm}^2$  (12 or  $4.3 \text{ mA/cm}^2$  depending on the evaluation used for the area) under the application of  $4 \text{ V}/\mu\text{m}$ , at a  $50 \mu\text{m}$  anode–cathode distance.

These values result to be comparable with the data found in the literature, for similar CNT-based emitter typologies. In particular, for CVD-synthesized MWNTs the threshold field (defined as the one needed to produce an integrated current density of  $10 \text{ mA/cm}^2$ ) varies between  $3$  and  $15 \text{ V}/\mu\text{m}$  approximately, primarily depending on the CNT emitter density [59]. For a medium CNTs density (between  $45$  and  $150 \text{ CNTs}/\mu\text{m}^2$ ) values between  $3.3$  and  $7.0 \text{ V}/\mu\text{m}$  are reported [59]. For low density films, between  $0.1$  and  $1 \text{ CNTs}/\mu\text{m}^2$ , the threshold field varies in the range  $10 - 14.4 \text{ V}/\mu\text{m}$ .

The field emission behaviour of our sample is dominated by the  $20 \mu\text{m}$  long CNTs extruding from the film, since they should not suffer any screening effect from the neighbours. From SEM observations, their density can be estimated to be lower than  $1 \text{ CNTs}/\mu\text{m}^2$ . Since the CNT diameters vary between  $20$  and  $100 \text{ nm}$ , using the approximation  $\beta \approx \frac{h}{r}$  [59] and taking  $h = 15 \mu\text{m}$  (the mean length of the extruding segment of the CNT), the field enhancement factor of the single emitter varies between  $300$  and  $1500$ . This large range includes the  $\beta$  value, which refers to an average  $\beta$ , estimated from our experimental data.

The interesting field emission properties of the CNT sample grown on conductive TiN layer at low pressure are appealing for many applications which require cold electron sources. For instance, the INFN project SERENA is investigating similar CNT-based field emitter devices as electron sources for electron cyclotron resonance (ECR) ion sources. ECR are widely used as injectors into linear accelerators, Van de Graaff generators or cyclotrons in nuclear and elementary particle physics. In atomic and surface physics ECR ion sources deliver intense beams of highly charged ions for collision experiments or for the investigation of surfaces.



## Chapter 4 Templated synthesis of carbon nanotubes

The configuration of the detector proposed in the NanoChanT project involves the synthesis of nanoconductors inside a highly ordered and insulating template. The enhanced space resolution will be determined by the reduced thickness of the active silicon diode layer, but a highly regular structure with submicron porosity is necessary to preserve the spatial resolution in the passage from the active layer to the read-out electronics. Nanoporous Anodic Aluminium Oxide (AAO), or alumina, exhibits a nanochannel structure that fulfils the required conditions. Therefore, its synthesis is certainly one of the milestones in the fabrication technology of the detector.

The pores of the AAO template have to be filled with nanoconductors that guarantee the electrical contact between the active silicon diode layer and the read-out electronics. Nanoconductors would be either metal nanowires or Carbon Nanotubes (CNTs). In this thesis the filling of the nanopores with CNTs has been studied.

This structure is also planned for investigations on field emission applications, since interesting emission properties of the CNTs grown inside an AAO template, despite the high density of emitters in this configuration, have been reported [52, 106].

### 4.1 Anodic aluminium oxide

#### 4.1.1 *Experimental setups*

Different investigations have been developed on alumina. A first group of experiments has been aimed at the optimization of the synthesis process and the regularity of the template. In a second block, the synthesis process has been modified in order to result faster and able to produce a larger amount of alumina samples, even if with a lower regularity. Indeed, a large number of templates has been required to face the issues of metal seeds electro-deposition and template growth of carbon nanotubes. Finally, some preliminary tests have been made on the anodization of a thick aluminium layer deposited directly on silicon. The experimental systems used in the different investigations have been adapted for the diverse scopes.

In the research of the conditions for the best alumina template quality, the growth process was performed in a class 100.000 (FED-STD-209D classification) clean room environment of the IMM–CNR Institute. To perform all processes needed for the aluminium oxide growth an anodization cell was designed and fabricated (Figure 4.1).

The cell is a Teflon cylinder with a bottom, in whose centre there is a circular hole, of 2 cm diameter. A Teflon lid is also used. The use of Teflon allows thermal insulation of the liquid, thus enhancing the temperature control. Moreover, this insulation permits to avoid fluid loss by evaporation, which can be unhealthy, and water condensation entering the cell. The sample is placed between the bottom of the cell and a stainless steel plate resting on another plate of Teflon. The way this contact is performed can critically affect the stability of the process. For a highly regular template sample, it is in fact necessary to ensure a uniform and stable electrical contact between the steel and the aluminium foil. The optimum solution has been found in using silver paste as adhesive material between the two metals, which guarantees good mechanical and electrical contact. Two different diaphragms have been used during the processes, a larger one (with a diameter of 2 cm) and a smaller one (0.85 cm diameter). The latter is used to anodize with different anodization parameters the same aluminium foils. Between the sample and the hole a Viton O-ring is put in order to ensure the closing of the system and avoid liquid leakage. A voltage is applied between the steel plate and a grid electrode. The grid is mounted in a Teflon ring and it is connected to a power supply. Voltage and current measurements are registered by means of a digital multimeter.

Usually, a volume of 0.4 l is used in the process step. The liquid is maintained at constant temperature by means of a thermostat which pumps cooling liquid (mixture of 3 l water with 1 l glycol) through a Pyrex spiral. Nitrogen is flown through a Pyrex inlet into the cell to stir the liquid. The optimum flow of 1 l/min is monitored by a flow meter. The stirring of the solution has already been reported to have a large influence in the anodization process, as it maintains uniform conditions at the pores bottom.

To fasten the production of alumina samples and thus the possibility to investigate the metal nanowires electro-deposition and the subsequent CNT growth, a different anodization system was developed in the laboratories of Physics Department of the University of Bologna. This system utilizes less strict conditions, and consequently the alumina regularity largely decreases. Moreover, the purity of the starting aluminium layer chosen for these experiments was lower (99.865 %). With this arrangement, the aluminium foils are totally immersed into the solution. In this way, both aluminium foil surfaces undergo the anodization process and the oxidizing aluminium layer remains in between the two forming aluminium oxide layers, ensuring the electrical contact.

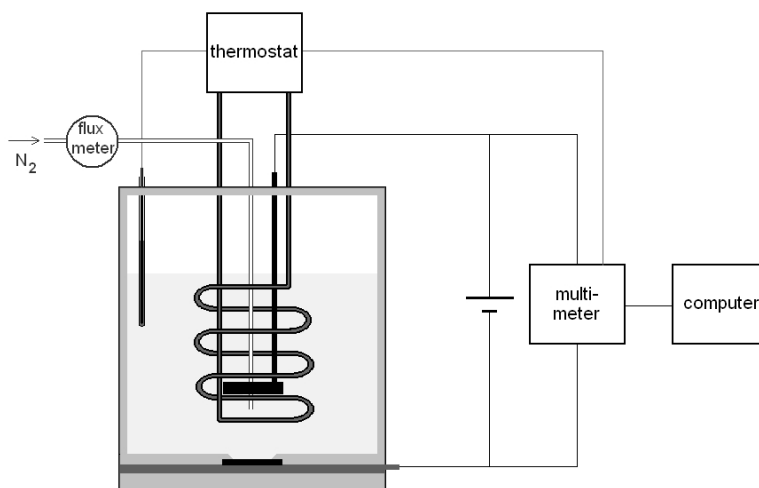


**Figure 4.1.** Schematic representation of the anodization cell. The sample is mounted in the center of the bottom supported by a stainless steel plate. A positive voltage is applied to the sample, while the platinum electrode is negatively charged. The spiral belonging to the thermostat and the temperature probe are also shown on the left. The fluid is agitated by a nitrogen flow kept constant at 1l/min.

#### 4.1.2 Syntheses and characterizations

The growth process employed Goodfellow high purity (99.999 %) aluminium foils, type AL000565/5, as rolled, light tight,  $25 \times 25 \text{ mm}^2$ ,  $100 \mu\text{m}$  thick. For the production of high ordered aluminium oxide templates, it is fundamental to start with a highly regular aluminium layer. Therefore, a procedure consisting of several steps has been adopted before the anodization in order to enhance the starting aluminium surface regularity:

- A degreasing of the aluminium foil in boiling acetone ( $56 \text{ }^\circ\text{C}$ ) for five minutes.
- A 3 hours long annealing process in a  $\text{N}_2$  atmosphere at  $400 \text{ }^\circ\text{C}$ .
- A cleaning procedure, based on literature indications [86]. After having placed the sample in the anodization cell, using silver paste for better mechanical and electrical contact, the sample is degreased in ethanol for 5 minutes at  $40 - 50 \text{ }^\circ\text{C}$ . Next it is etched with a  $1.5 \text{ M NaOH}$  solution at  $55 - 58 \text{ }^\circ\text{C}$  for 30 seconds. Without water rinse, a second cleaning with  $1.5 \text{ M HNO}_3$  solution is immediately performed for 30 seconds at room temperature. The sample is then washed thoroughly with water, filling and draining the cell many times.
- A 20 second long electropolishing treatment, with temperature set at  $10 \text{ }^\circ\text{C}$  and the applied voltage at  $40 \text{ V}$ . A solution of alcohol, perchloric acid (70 % in weight), butyl glycol and water with relative volume amounts of 350:83:50:73 is used.
- A 60 second long etching treatment with  $0.24 \text{ M Na}_2\text{CO}_3$ , performed at  $80 \text{ }^\circ\text{C}$ .

The annealing at 400 °C has the function of increasing the grain size of the aluminium, and also of reducing the number of defects inside the grains. The second etch allows the removal of the top aluminium layer to get rid of the impurities contained there.

The electrically enhanced etching process is commonly performed to even out surface irregularities. It is not possible to achieve a sufficient regularity in the pores array without electropolishing. However, it is quite difficult to exactly control this process since it involves strong reactions, with both high voltage and current. If a too aggressive process is performed, because it is too long, the electropolishing can result in damaging the sample. In fact, locally enhanced etching causes the arising of small defects, whose number increases with time. These defects, which are regular cut holes due to an effect of the orientation of the aluminium crystals, are mainly located at grain boundaries. They have a very negative influence on the subsequent anodization process, since they act as preferential sites for the process developing holes in the aluminium which bring to end the anodization process. At the end of the electropolishing process, the cell is opened and the sample carefully rinsed and dried with nitrogen. If electropolishing liquid remains on the aluminium surface, the etching reaction goes further and defects appears. The last etching removes the thin oxide layer remaining from the electropolishing reaction [86].

For the anodization step, a 0.3 M oxalic liquid solution was chosen since it achieves the most regular pore pattern at a voltage of 40 V. This voltage results in pore dimensions and pitch (about 50 and 100 nm respectively) which seem to be the most appropriate for the final detector application. Two kinds of anodization process can be carried out, depending on the regularity requirements, that is to say a single-step or a two-step anodization.

In the former case, an anodization step is performed maintaining the temperature at 5 °C and the voltage at 40 V. The liquid is stirred during the entire process. The duration of the process depends on the desired pores depth. The typical rate is 3.7 µm/h. During the process, the current vs. time curve, shown in Figure 4.2, reflects the expected behaviour described in Paragraph 2.2.2. The current starts high and quickly drops because of the oxide layer formation. When pores start to grow, the current increases again until it reaches a steady stage. If larger pores are wanted, the sample can be etched in a mixture of phosphoric acid (85 % in weight) and water with relative volume amounts of 1:19 at specific temperature and time.

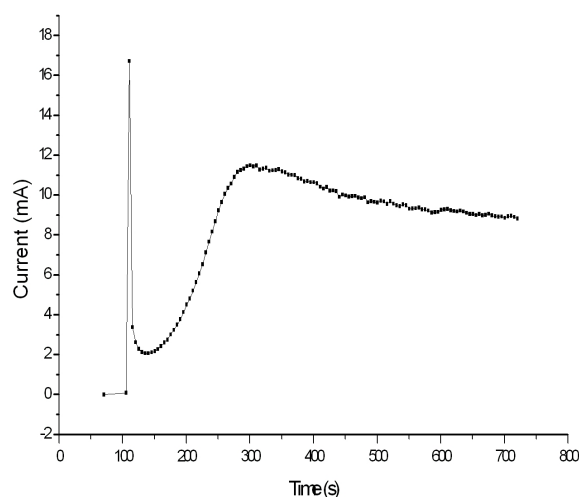


**Figure 4.2.** Typical current development during standard anodization. The highly conductive aluminium quickly oxidizes, which results in a current drop. When the pores start to form, the current rises and then becomes stable, decreasing slowly because of the growing pore depth.

If an enhanced quality is needed, the two-step anodization has to be performed. The template regularity increases as the pores grow downwards. Thus, removing the upper part of the oxide layer results in a more regular pattern and in a greater similarity between the top and the bottom part of the template. The two-step anodization achieves these conditions by means of two separate anodizations with an etching process in between.

A first anodization is carried out for 4 hours in the previously described condition, obtaining a 12  $\mu\text{m}$  thick oxide layer. The same phosphoric solution used for pore enlarging can be used for the etching step. Two different etching processes can be done. In the first approach a partial etch is made, lasting 40 minutes, which widens but not completely destroys the pores. Afterwards, the second anodization and a second etching, 20 minutes long, follow. The upper part of the oxide template is now completely dissolved, whereas the lower part has reached at the same time the desired pore widening. This approach is forced to employ the same conditions for the two anodizations, to make the pore pattern matching.

The second approach consists of a complete removal of the first aluminium oxide layer, by means of an etching process 90 minutes long at 30 °C. The remaining aluminium layer presents a regular pattern of indentation. The second anodization, made under the same process parameters, starts from these indentations and the template reaches a better regularity. A second etch using the same parameters but lasting 30 minutes is finally performed. The two approaches, illustrated in Figure 4.3, result in similar template regularity. The second one, however, has the advantage of allowing a wider range of possible pore diameters, as any etching time for the second step can be chosen, because no upper part has to be removed anymore. After these anodization steps, the cell is opened and carefully cleaned in water.

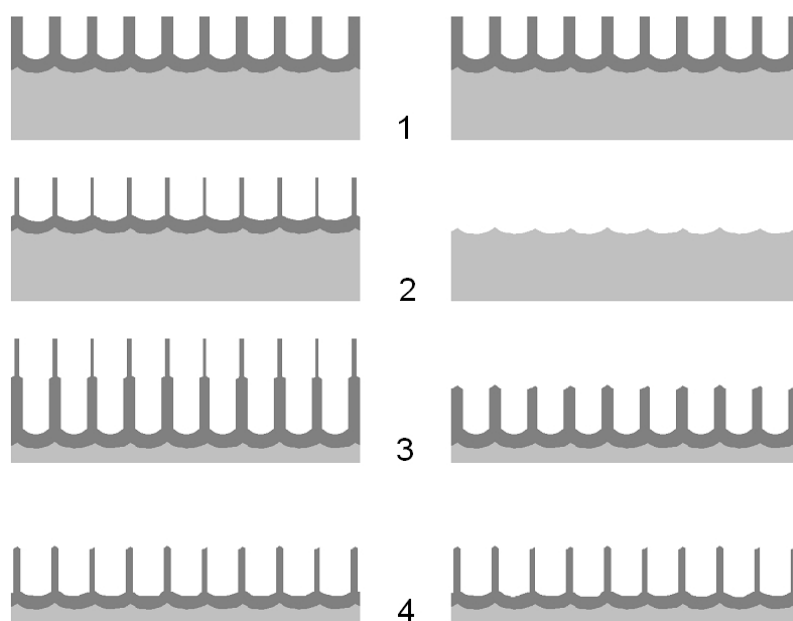


**Figure 4.3.** The two different approaches for the two-step anodization process are depicted. Both the processes start with a first anodization, 4 hours long (1). The samples are then etched by a phosphoric solution for a partial removal of the alumina layer (“sacrificial layer”) produced in step (1), on the left, and for a complete removal of the sacrificial layer on the sample on the right (2). The second anodization follows (3) and finally a second etch is performed (4). If the same acid is used in all the steps, both methods yield the same results.

Different steps can be performed after anodization, depending on the desired AAO template morphology. These differences are mainly associated to the subsequent processes, namely the catalyst electro-deposition and the CNT synthesis. The removal of the pore barrier layer depends on whether the catalyst deposition would have to be performed by means of a DC or AC process. Moreover, if the AAO template has to be used in a process at a temperature higher than 650 °C, i.e. the melting point of aluminium, it is necessary to remove the residual aluminium layer. Different procedures have been considered for these aims.

For removing the aluminium layer, the sample is generally remounted on the cell, but upside-down, so that the aluminium layer results exposed at the solution. The sample is next attacked using a mixture of H<sub>2</sub>O, HCl (37 % in weight) and 0.2 M CuCl<sub>2</sub> in relative amounts of 1:1:2 for 10 minutes at room temperature, until all aluminium is removed by the back of the oxide. The reaction is highly selective and the alumina is not attacked at all. The dissolution, whose rate is quite high (about 10 – 20 μm/h), is not continuous but it proceeds by steps. When immersed in the solution, the aluminium turns black, forming a soft layer on the metal. After some time, this upper layer detaches, exposing the underlying remaining aluminium. The aluminium is thus removed away in layers.

A different approach based on a voltage reversal [107] has also been tested. At the end of the anodization, a sudden reversal of the polarization is applied to the electrodes. This results in a H<sub>2</sub> gas formation in the electrolyte. The gas forms at the oxide/metal interface too, as can be seen by the bubbles generated under the oxide. Because of the barrier layer, however, the gas can not penetrate through the oxide and remains between the two layers. It was observed that gas formation occurs preferentially at the diaphragm border. When the pressure rises above a certain limit, the oxide detaches from the aluminium. The main drawback of this technique is the difficulty of controlling it. The reaction is violent, and oxide breaching often occurs, especially located at the border of the sample. To limit this effect, the voltage has been lowered from 40 to 20 V before the reversal, but the problem, albeit reduced, remains. Furthermore, once a breach appears, the current finds a direct path through the aluminium layer, avoiding the oxide/metal interface. Consequently, the reversal voltage technique can not be anymore effective.

The last possibility consists in extending the anodization until all the aluminium will be oxidized. The negative aspect of this approach is that, especially if an AAO thickness of 100 µm is not required in the actual investigation, the process duration is very long. At a growth rate of 3 – 4 µm/h, a complete anodization takes 25 – 35 hours. Furthermore, other problems arise when performing this method. Particular care has to be taken to protect the stainless steel on which the sample is attached. When the aluminium is breached, the steel comes in contact with the acid solution and, being the etching electrically enhanced, it is etched away. The breaching and the subsequent etching are sudden processes, so that current monitoring would not solve the problem. A possible solution, based on some hints reported in literature [108], has been investigated. A gold layer, 100 – 300 nm thick, has been evaporated on the aluminium foil. Since the gold layer can not be easily etched by the acid solution, when the aluminium anodization is finished the current evolution changes with respect to the case of the stainless steel underlying layer (Figure 4.4). In the gold layer case, the current starts to rise. Initially because the oxide barrier layer becomes thinner and later because a direct contact of gold with the electrolyte occurs. At this stage, gas starts to form and the current, after having reached its maximum, starts decreasing because of the insulating properties of the formed gas. The reaction has to be stopped at maximum current, to avoid that a too high gas pressure damages the sample. This approach presents also some drawbacks. In particular, since some pores arrive at the gold layer before the others, the current will follow these preferential paths. This results in a gold etching that exposes the stainless steel and can give the problems mentioned above. An alternative is to stop the anodization before these breaches occur, monitoring the current evolution. However, this approach leaves an aluminium layer, even if very thin.

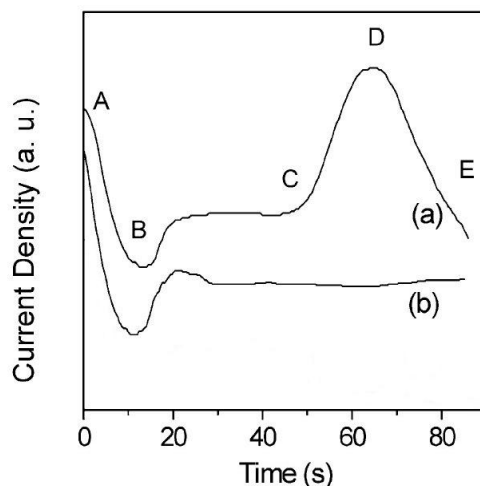


**Figure 4.4.** Current development during anodization using a sample with (a) and without (b) a gold layer between the aluminium and the stainless steel. When the gold is reached in process (a), the current rises because of the thinning of the barrier layer and the fact that gold is not oxidized by oxalic acid. In process (b) the reaction does not reach the underlying stainless steel. If it is continued until it does, the current will become unstable.

A further alumina configuration can be required if open pores are desired on both sides. This arrangement allows, for instance, a DC metal electro-deposition inside the pores. Different solutions have thus been tested for dissolving the oxide barrier layer.

One method for opening the pores on both sides consists in decreasing the anodization voltage to thin the barrier layer. As stated in Chapter 2, the barrier layer thickness is proportional to the applied voltage. When the voltage is lowered, the current instantaneously is reduced, since fewer ions can overcome the barrier layer between metal and electrolyte. Oxide growth is thus slowed down. The etching slows down too, but less than the oxide growth process, since no barrier layer has to be passed through. Immediately after each voltage reduction, the current falls down and soon after increases to a new steady value, lower than the previous one. The new equilibrium imposes a thinner barrier layer thickness than the starting one. The voltage decreasing step can not be too large, otherwise the reaction can even run out, since the ions current can overcome the barrier. This consideration becomes more critical at lower voltages, so that the voltage decreasing steps have to be reduced during the process. For example, at the beginning they can be 2 V, then become 1 V below 20 V, and 0.5 V below 10 V. Anodization voltages as low as few volts can be achieved. The residual thin barrier layer can be etched away by means of a phosphoric solution. A disadvantage of this method is caused by the fact that not only the barrier layer, but also the radius of the pores depends on voltage. A network of small pores then grows at the pore bottom, making the oxide template irregular at its bottom.

If a final AAO template without aluminium layer is needed, a simpler method can be followed to remove the barrier layer. After the anodization and the removal of the aluminium layer by means of the  $\text{H}_2\text{O} - \text{HCl} - \text{CuCl}_2$  mixture, the sample can be etched by a 0.7 M phosphoric acid solution. The best conditions to open the pores without enlarging their diameters have been found in correspondence to a 20 minutes long process, at a temperature of 40 °C.

All the steps of the fabrication process of the aluminium oxide are summarized in Table 4.1.

| <b>Table 4.1</b>   |  |  |
|--|--|--|
| <b>Fabrication process of Anodic Aluminium Oxide.</b>  |  |  |
|  | Step                                       | Description  |
| 1  | Degreasing                                 | Degreasing in boiling acetone (56 °C) for 5 minutes  |
| 2  | Annealing                                  | Annealing process in a $\text{N}_2$ atmosphere at 400 °C   |
| 3  | Cleaning                                   | Degreased in ethanol for 5 minutes at 40 – 50 °C<br>Etching in 1.5 M NaOH solution at 55 – 58 °C for 30 seconds<br>Cleaning in 1.5 M $\text{HNO}_3$ solution at room temperature for 30 seconds  |
| 4  | Electropolishing                           | Electropolishing at 10 °C, 40 V, in a solution of alcohol, perchloric acid (70 % in weight), butyl glycol and water (350:83:50:73), for 20 second long.<br>Etching in 0.24 M $\text{Na}_2\text{CO}_3$ , at 80 °C, for 60 seconds   |
| 5  | Anodization                                | <i>Single-Step process</i><br>0.3 M oxalic solution, voltage of 40 V, at 5 °C<br><i>Two-step process</i><br>0.3 M oxalic solution, voltage of 40 V, at 5 °C (4 h)<br>Partial (I method) or complete (II method) etching process (40 or 90 minutes, 30 °C)<br>0.3 M oxalic solution, voltage of 40 V, at 5 °C<br>Final etching in 0.7 M phosphoric solution |
| <i>Extra treatments for specific applications</i>  |  |  |
| 6  | Removal of Al layer                        | <i>First method (Sample place upside-down in the cell)</i><br>Etching in $\text{H}_2\text{O}$ , HCl (37 % in weight) and 0.2 M $\text{CuCl}_2$ (1:1:2), at room temperature (10 minutes)<br><i>Second Method:</i> Complete anodization of the Al foil  |
| 7  | Pore widening/<br>Removal of barrier layer | Voltage decreasing during final anodization (if the Al layer is present)<br>Etching in 0.7 M phosphoric solution (from the pore bottom if the Al layer has been removed with the first method, otherwise from the pore top)  |
| <b>Notes:</b> The duration of the step can be varied according to the specific requirements of the desired alumina. The durations reported in the table refer to the production of the alumina shown in Figure 4.5 and subsequent. Optional post-anodization steps are also reported (step 6 and 7). |  |  |

The alumina template obtained by the entire anodization process (described in Table 4.1) followed by the aluminium removal and pores opening, shows pore diameters and pitches of about 40 nm and 100 nm, respectively (Figure 4.5). It is worth noting the different regularity at the front and at the back surfaces of the template, better visible at lower magnifications. As expected, the regularity is better at the back than at the front surface. Nevertheless, the upper surface is quite regular having been obtained by means of the two-step anodization. Some defects still exist in the hexagonal pattern (Figure 4.6). It is interesting to note that, when a pore is missing, the adjacent pores are elongated towards the defective centre. This is an indication that pores are formed by a symmetrical equilibrium of forces, whether mechanical or electrical ones. In lower magnification images (Figure 4.7), it can clearly be seen the existence of highly regular areas, of micrometric dimension, with a pore pattern heading in different directions, separated each other by borders with many defective sites. The pores are very regular and parallel to each other over large distances. The thickness of this template can be freely chosen by tuning the process time. In the reported conditions, the rate is 3.7  $\mu\text{m}/\text{h}$ . Pores 95  $\mu\text{m}$  long are obtained with a 25 hours long process. The related aspect ratio is  $3.2 \cdot 10^3$  (Figure 4.8). If the pores barrier layer is not removed, the scalloped shape of the pores bottom can be seen (Figure 4.9).

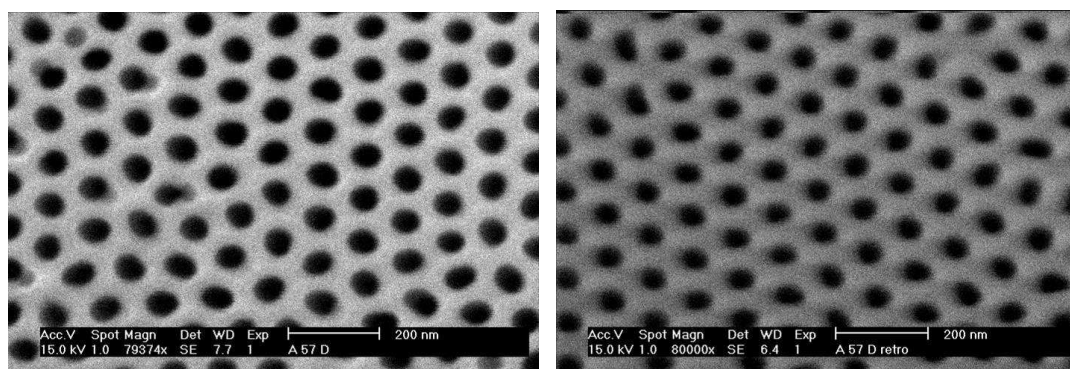


**Figure 4.5.** SEM micrographs of the pore patterns at the front (left) and at the back (right) surface of the aluminium oxide sample.

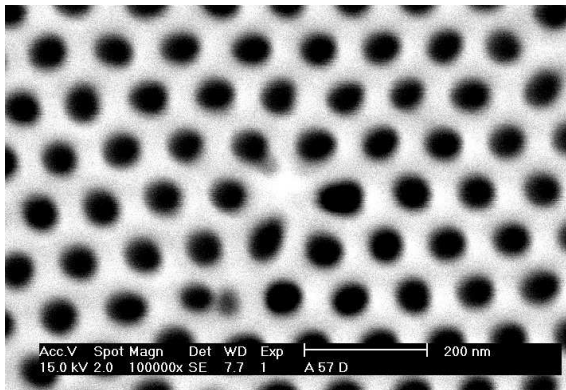


**Figure 4.6.** SEM micrograph showing a missing pore in the AAO honeycomb structure. As a result, the surrounding pores have a slightly different form, showing the need of symmetry in regard to the forces responsible for the pore creation.

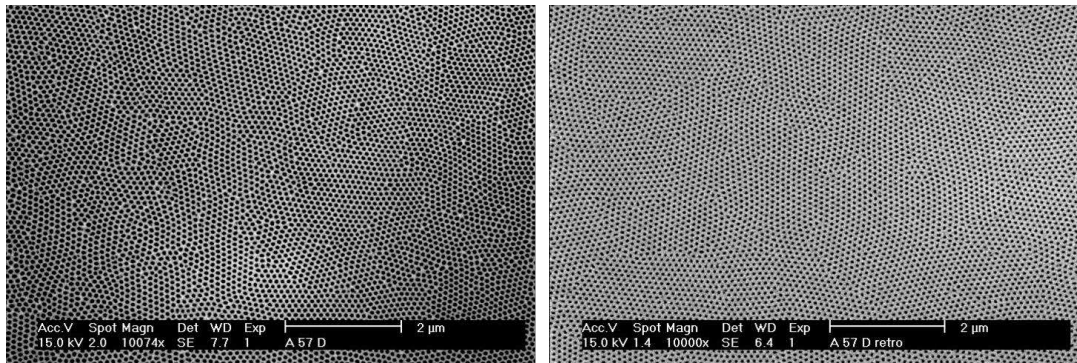


**Figure 4.7.** SEM micrographs of the same sample shown in Figure 4.5, but at lower magnification. Differences in large-scale regularity can be seen. At the front surface more defects are visible as white dots. The back surface has fewer defects, although the size of the defect-free regions has not grown significantly.

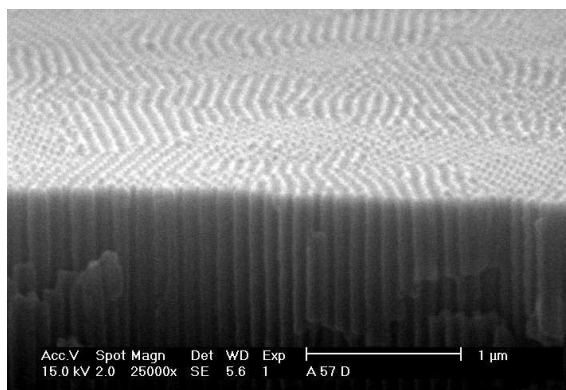


**Figure 4.8.** Tilted SEM micrograph of the same sample shown before. The sample has been cleaved so that both the cross-section and the surface can be seen.

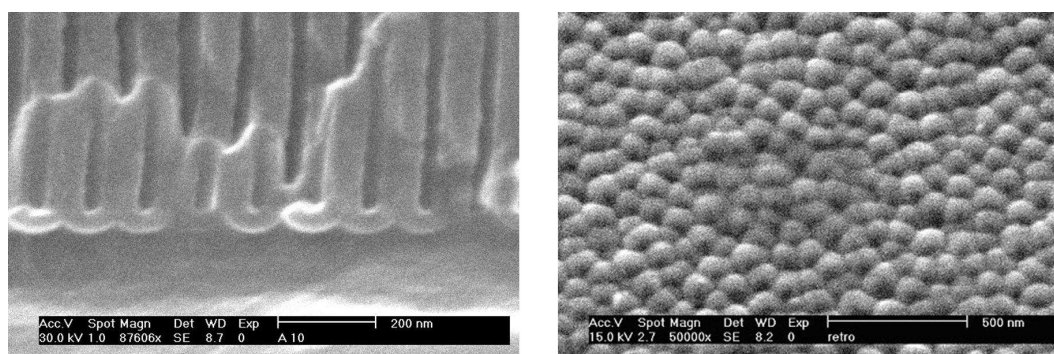


**Figure 4.9.** SEM micrographs of the aluminium oxide barrier layer. In the cross-section (left) the semi-circular shape of the barrier layer is evident. A top-down view is shown (right), after that the aluminium has been removed. The scalloped shape can be seen.

To fasten the production of alumina samples used in investigations on the metal nanowires electro-deposition and on the subsequent CNT growth, a different anodization process has been established. To define this “quick method” of anodization, summarized in Table 3.2, we based on the literature and on the experience of a guest professor collaborating in this research [86, 109].

Low purity aluminium foils (99.865 %), 75  $\mu\text{m}$  thick, have been employed, cut to obtain flag-shape samples, i.e. square samples,  $20 \times 20 \text{ mm}^2$  size, with an extra tag. This extension has been used to clip the sample to the electrode. The anodization solution is contained in a quartz cell, where the sample is immersed. Only few steps of the preparatory procedure for the formation of the regular AAO, summarized previously in Table 3.1, have been maintained. That is, the etching in NaOH solution, in order to remove the top layer of the aluminium, and the cleaning in  $\text{HNO}_3$ . After each step the sample is carefully washed in water. The anodization process has been then performed at 17  $^\circ\text{C}$ , in a 0.3 M oxalic solution at 40 V [109]. The higher temperature with respect to the previously used 5  $^\circ\text{C}$  results in a faster process. Indeed, the growth rate in the new conditions has been estimated to be approximately 6.5  $\mu\text{m}/\text{h}$ . The process duration has been calibrated in order to obtain the desired sample thickness. After the anodization, other steps have been performed in order to reduce the barrier layer thickness. The anodization process in oxalic has been ended with a controlled voltage decreasing down to 20 V, in order to thin the barrier layer down to 20 nm, and then a pore widening has been performed. A thinner barrier layer allows performing the metal deposition at lower voltages. More homogeneous conditions can thus be utilized and the metal deposit turns out to be more uniform. Otherwise, if high voltages are required for the deposition, long durations can bring to local breakdown of the barrier and hence inhomogeneous conditions for the subsequent electro-deposition [88], which brings localized deposits of metal.

| Table 4.2  |  |   |
|--|--|---|
| “Quick method” for the fabrication process of two-sides Anodic Aluminium Oxide                                     |  |   |
|  | Step   | Description   |
| 1  | Cleaning   | Etching in 1.5 M NaOH solution at 50 – 60 °C for 20 seconds<br>Cleaning in 1.5 M HNO <sub>3</sub> solution at room temperature for 60 seconds |
| 2  | Anodization  | 0.3 M oxalic solution, voltage of 40 V, at 17 °C  |
| 3  | Pore widening/<br>Thinning of the<br>barrier layer | Voltage decreasing during final anodization<br>Etching in 0.7 M phosphoric solution, at 30 °C, for 20 minutes                                 |
| <b>Note:</b> The duration of the anodization step can be varied according to the desired thickness of the alumina. |  |   |

A different approach, in which the AAO template is grown starting from an aluminium layer deposited on a silicon substrate, offers better capabilities with respect the fabrication of an anodic aluminium template starting from an aluminium foil. This arrangement would be more suitable for CMOS applications in general, because of its larger compatibility, and for the NanoChanT project in particular, where the alumina template has to be inserted between two silicon layers, that is to say the active detector and the read-out electronics. In fact, if the fabrication of the three layers is independently performed, a solution for their bonding is needed. Furthermore, although the alumina film would have the mechanical stiffness required for fulfilling the NanoChanT project, it is very brittle to be used for the most common characterization techniques. Aluminium oxide samples grown on silicon could be more easily manipulated.

This deposition of aluminium on flat substrates is widely used in mirror glass fabrication, but in that case the thickness of the aluminium layer is kept at some nanometres, to maximize reflectivity. If the aluminium deposited on silicon has to be used in an anodization process, thicker layers are demanded. To obtain good regularity in the honeycomb structure some processes have to be performed, as already described in the previous section. In particular, the electropolishing of the starting aluminium film and a two-step anodization process critically reduce the thickness of the final nanoporous template. Thicknesses about 50 µm are necessary.

Recently, some researches have focused on the deposition of thicker aluminium layers on silicon [110], which can be useful for the alumina template growth on silicon. In order to obtain a highly ordered AAO template, it is necessary to anodize a very smooth and regular aluminium layer. Moreover, it is important that the deposited layer has large grain sizes. In fact, many of the defects in the final template occur at grain boundaries, and the pore pattern regularity is obtained inside each original crystalline grain. Many papers refer about the synthesis of CNTs inside AAO templates directly grown on silicon

substrates [106, 111, 114], using electron beam evaporation and magnetron sputtering methods for the aluminium deposition. However, the thickness of the starting aluminium layers is very small for both deposition techniques (about 300 nm and 150 nm for the sputtering and for the evaporation method, respectively [111]) and does not allow performing neither a two-step anodization nor a single-step anodization over long duration. Consequently, the resulting template regularity is very poor [111], or its thickness is limited. Thicknesses above 12  $\mu\text{m}$  have not been reported so far, to our knowledge [106]. Some investigations have thus been focused on the deposition of aluminium films thicker than those reported in the literature.

Aluminium films have been deposited on a silicon substrate, coated with a 20 nm thick gold layer by electron beam evaporation. The gold layer allows a better control of the anodization current evolution so that the anodization process can be stopped before etching of the silicon substrate. Aluminium thicknesses in the 2 – 6  $\mu\text{m}$  range have been evaporated. A 4 hours long annealing follows at 400 °C in  $\text{N}_2$ , in order to enhance the crystalline regularity. However, layers thicker than 3  $\mu\text{m}$  are more irregular since the sample is kept closer to the aluminium source, where the irregularity of the emitted atoms distribution is higher. The first attempts of processing this kind of samples have failed. During pre-anodizing steps too much aluminium dissolves and nothing of the starting 3  $\mu\text{m}$  thick aluminium remains. On the contrary, if no pre-anodization steps are performed, the quality of the final sample is very low in term of regularity.

To achieve thicker aluminium layers deposition, the magnetron sputtering technique has been used. Firstly, a niobium layer, 100 nm thick, is sputtered on the silicon substrate. This additional layer is required to avoid the alumina cracks due to the difference in thermal expansion coefficients of the alumina and aluminium, since the Nb thermal expansion coefficient is intermediate between the two. It has been reported that alumina on aluminium layer cracks at about 300 – 400 °C, whereas alumina on Nb is not damaged at 1100 °C in He atmosphere [112]. Afterwards, aluminium has been deposited. Some particular conditions have been implemented for this process in order to enhance the control over the growth of the aluminium layer. The silicon substrate has been heated up to a temperature of 400 °C during the deposition. The heating of the substrate enhances the formation of larger grains [110], which is desired, as it minimizes the grain boundary defects and the presence of independently oriented pore pattern. A disadvantage of higher substrate temperature is that the larger are the grains, the larger is the roughness [106]. Moreover, in order to achieve a smooth surface, the substrate has been kept rotating at 10 rpm, the maximum speed allowed to the facility.

The as-deposited samples have a whitish colour. The corresponding aluminium layer morphology can be seen in Figure 4.10. Thicknesses up to 7  $\mu\text{m}$  have been sputtered, at a rate of approximately 1  $\mu\text{m}/\text{h}$ . The deposit consists of many grains, some microns in size, and the surface is very irregular.

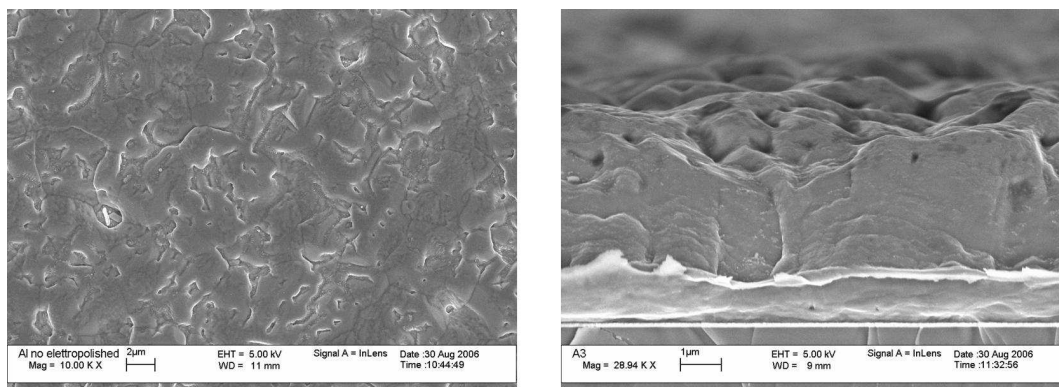


**Figure 4.10.** SEM micrographs of planar (left) and cross-section (right) views of the aluminium layer deposited on the heated Nb/Si substrate by means of the magnetron sputtering technique. On the right, the base of the aluminium layer is lifted due to the cleavage process, necessary for the cross-section observation.

The Si – Nb – Al samples have been processed in two different ways. One sample directly undergoes an anodization process, without being electropolished. On a second sample, a brief electropolishing, 3 second long, has been performed in the conditions reported in Table 3.1. The resulting sample turns out to be reflective, since the process evens out most of the starting roughness. Both samples have been then processed in the anodization cell by means of the single-step process, performed at 17  $^{\circ}\text{C}$ , with a pore widening treatment following.

Without electropolishing, the alumina template is very irregular (Figure 4.11). Pores have grown perpendicularly to the local upper surface and the global configuration consists of separate blocks, with pores grown along a locally defined orientation. Many defects occur, especially at grain boundaries. Moreover, the anodization process turns out to be incomplete, as an irregular aluminium layer, with a mean thickness of 1.4  $\mu\text{m}$ , still remained between the Nb layer and the alumina, whose thickness is approximately 4.5  $\mu\text{m}$ . Such a configuration can cause problems during the CVD synthesis, since the aluminium can suffer thermal stress resulting in sample damage.

Regularity is strongly enhanced in the electropolished sample. Large alumina islands with highly ordered channels, extending up to lateral dimensions of 40  $\mu\text{m}$ , are obtained. After the electropolishing, the alumina thickness is 2.5  $\mu\text{m}$ , constant over the entire island surfaces (Figure 4.12). A preliminary CVD process has established that the Si – Nb – AAO can withstand temperatures up to 620  $^{\circ}\text{C}$ . However, some cracks occur on the

sample. The related thermal stresses that cause these breakdowns are supposed to be due to local presence of residual metallic aluminium under the anodized layer.

Depositions of larger thicknesses and the subsequent processing are currently under investigation.

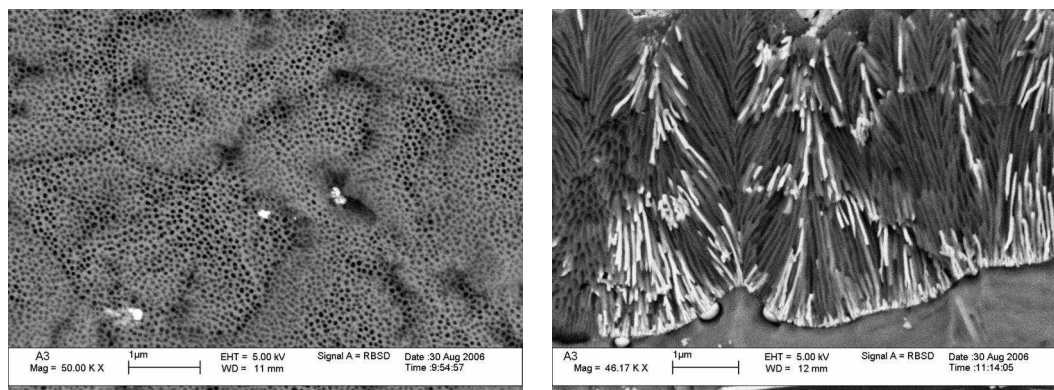


**Figure 4.11.** The Al/Nb/Si sample shown in Figure 4.10 has been anodized without any electropolishing treatment. SEM micrographs, taken with the back-scattered electron detector, show that the resulting morphology is very irregular: the roughness of the upper surface is high (left). During anodization, the pores grow perpendicularly to the upper surface and so inherit the irregularity from the surface (right). An electro-deposition of cobalt has been attempted as indicated by the partial filling of the pores with metal nanowires.

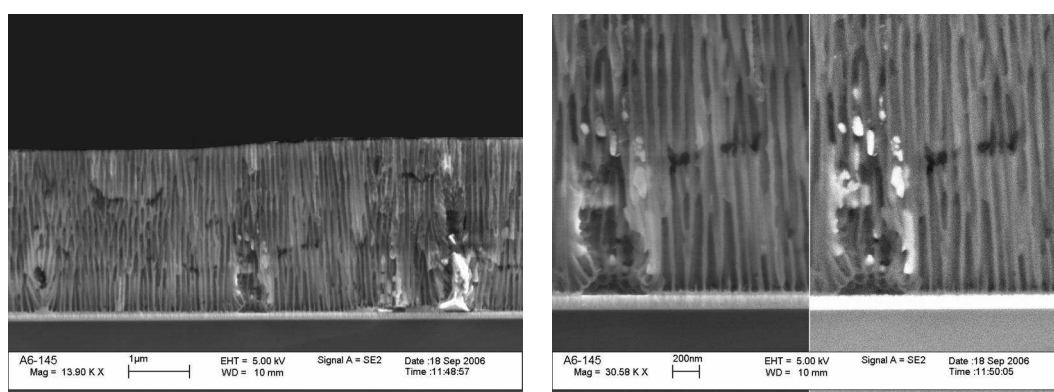


**Figure 4.12.** SEM micrographs of the same sample shown in Figure 4.10. A brief electropolishing has been performed before the anodization. The regularity of the pores is enhanced, even if some defects are still present. On the right, a higher magnification SEM micrograph clearly shows the niobium layer. On the sample, an electro-deposition of cobalt has been also carried out, as indicated by the few metal nanowires.

### 4.1.3 Catalyst seeds deposition

Nanoconductors have to be grown in the template pores to allow electrical contact between the active silicon layer and the read-out electronics. Either the nanoconductors will be metal nanowires or carbon nanotubes, the deposition of metal inside the alumina pores is an obligatory step to be performed. In fact, in the former case the nanowires themselves act as charge collectors, whereas in the latter case they are necessary as a catalyst seed for the subsequent CNT growth.

In this thesis, the viability of the CNT-based solution has been investigated. With this purpose, the metal deposition of the metallic seeds inside the alumina pores requires a limited nanowires length. However, it is important that the deposition results uniformly distributed inside the sample, because of two reasons. Firstly, the final device requires a regular distribution of CNTs inside the alumina template. Secondly, to properly characterize the seeds deposit cross-section SEM observations have been employed, which can give information about the seeds density of the sample only along one dimension. This requirement is closely associated with achieving uniform conditions in the barrier layer of the alumina pores. In case some barriers have been opened before the others, the current concentrates in these preferential paths, leading to thicker deposit of metal.

The most frequently used catalysts for the CNT growth are the transition metals (Ni, Fe, Co) [36, 49]. In particular, cobalt is commonly employed as a catalyst for the alumina-templated synthesis of CNTs. The electro-depositions have been performed in a cell similar to the one used in the anodization process. The design, depicted in Figure 4.13, is less complex since the process is less affected by instabilities. The voltage during the process is provided by a power supply, which allows the generation of different wave functions. Both AC and DC depositions have been attempted. The processes have been performed at room temperature, employing a liquid mixture of 0.42 M CoSO<sub>4</sub> and 0.7 M H<sub>3</sub>BO<sub>3</sub> dissolved in water. Boric acid is used because it is useful for steadying the pH of the solution, in the 5.5 – 6 range. In fact, especially at the pore bottom, where the Co reduces and precipitates, the acidity of the solution tends to get higher. It is important to counterbalance this increase in order to avoid the formation of crystalline cobalt salt.

A sinusoidal voltage waveform has been adopted during the AC deposition, with 16 V<sub>RMS</sub> and a frequency of 200 Hz. Duration between 1 minute and 4 hours have been attempted. Cobalt has been successfully deposited inside the pores, from the bottom upwards (Figure 4.14). The samples change colour after the deposition, becoming blacker and blacker as the deposition goes on. The deposition rate decreases with time, as reported in literature [86]. The dependence of Co nanowires length on time is also shown in Figure 4.14. This is considered to be mainly due to the Co ion depletion of the electrolyte inside the pores. A mechanical stirrer has been in fact necessary for depositions longer than one hour.

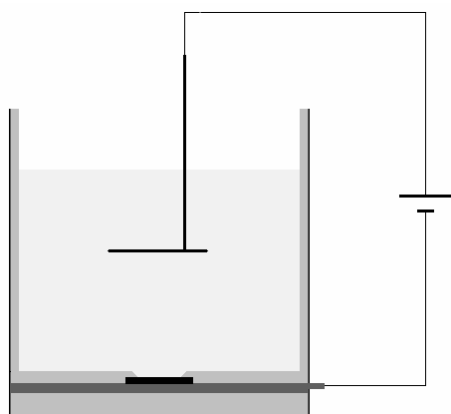


**Figure 4.13.** Synoptic setup of the cobalt deposition process. The cell is similar to the one used for anodization. A cobalt counter-electrode is placed in the liquid.

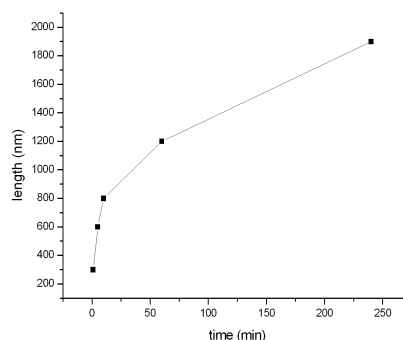
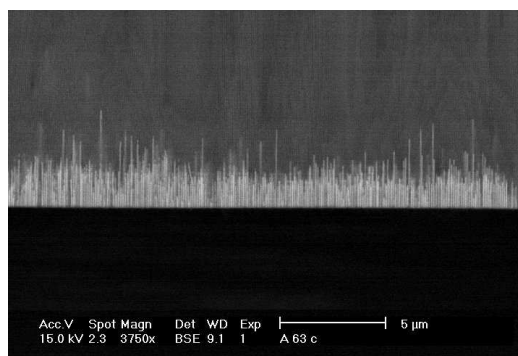


**Figure 4.14.** On the left, a back-scattered electrons SEM micrograph of the cobalt deposit after 4 hours. On the right, the dependence of cobalt nanowires length on time is reported.

It has to be noted that the continuous voltage reversal can result in oxide detaching from the aluminium layer, by means of the same process described on Paragraph 4.1.2 when the reversion of the voltage was specifically performed in order to obtain such detachment. This circumstance has to be avoided in order to achieve a regular sample.

On the alumina samples anodized on both sides by means of the “quick method”, the deposition of the catalyst has been performed only by means of an AC process, since the anodization leaves the aluminium layer between the two oxidized faces. A new solution has been employed, consisting of 0.42 M  $\text{CoSO}_4 \cdot 7 \text{H}_2\text{O}$ , 0.7 M  $\text{H}_3\text{BO}_3$  and 0.05 M  $\text{MgSO}_4$ . Differently from the previous ones, magnesium sulphate has been added in order to prevent the breakdown of the barrier layer [90].

Further investigations have been focused on establishing the proper ranges of values for obtaining a controlled electrochemical deposition of metal catalyst seeds (Co or Ni). Different parameters have been thus investigated, both for DC and AC depositions, until a uniform deposition has been achieved. When this is the case, the samples turn out to

be uniformly coloured. This colouring is correlated to the attainment of a particular current density during the electro-deposition, which differs in DC and AC depositions. In the former case, current densities of about  $1.5 \text{ mA/cm}^2$  have been experimentally associated to a satisfactory metal deposition, whereas in the latter case, the optimum value has been established to be approximately  $10 \text{ mA/cm}^2$ .

Voltage, waveform and frequency parameters which force these current densities across the pores have been determined. Sometimes, these settings have to be slightly adjusted during the deposition to maintain a proper current, depending on the employed alumina sample. This is thought to be due to non uniform conditions in the barrier layers of the different samples. For AC deposition, the best conditions for the samples with alumina on both sides are a sinusoidal waveform with a frequency of 50 Hz and a root-mean-square voltage between 9 and 12 V.

DC depositions have been performed on samples with alumina on only one side. After the removal of the residual aluminium layer by means of the chemical etching treatment (Table 3.1), on the back-side a 100 nm thick layer of Cr has been evaporated in order to act as counter electrode during the electro-deposition of the catalyst. A 150 nm thick Au layer has been also evaporated to strengthen the contact. For these samples, the best conditions correspond to a voltage in the 3 – 3.5 V range.

The templates employed for the confined CNT growth, described in the next section, belong to the set of samples prepared for this investigation and hence they have been produced by means of processes involving current densities smaller than the optimal ones, subsequently established.

## 4.2 Carbon nanotubes synthesis in anodic aluminium oxide templates

The growth of carbon nanotubes (CNTs) inside the highly ordered nanochannels of the anodic aluminium oxide (AAO) has been investigated for the realization of the detector proposed in NanoChanT project. Different process parameters have been varied. Alumina samples have been produced with both systems described in section 4.1.

The first investigations have been mainly devoted to an initial set up of the CVD growth of CNTs in the AAO template. At this aim the alumina samples produced by anodization on both sides of the aluminium foil have been used. These samples conserved their residual aluminium back-layer between two alumina layers, which imposes some constraints on the CVD process. Even approaching the Al melting temperature at  $660 \text{ }^\circ\text{C}$ , thermal stresses, due to the difference in thermal expansion coefficient between aluminium and alumina, induce mechanical deformations in the samples, which frequently turned out in cracks. Therefore, an upper limit temperature has been established at  $620 \text{ }^\circ\text{C}$  and the controlled heating ramp has been adopted in order to avoid thermal overshoots. In case the

residual aluminium back layer has been removed, on the AAO samples prepared with one side aluminium anodization, syntheses at 700 °C were performed.

Also water incorporations can result in enhanced thermal stresses at high temperatures. Alumina, as a porous material, tends indeed towards adsorbing humidity from the atmosphere and, in addition, residual humidity comes from the aqueous solution used for the anodization process. Therefore, it is necessary to dehydrate the sample before it undergoes the CVD process. A pre-process in vacuum has been performed, so to remove water molecules from the pores. The CNT growth processes have been all performed in the CVD furnace.

A first CNT growth process, based on the conditions used in the literature [52], has been performed on a double-faced alumina sample prepared by means of the “quick method” (Table 3.2). The duration of the process has been set in order to obtain a thickness of 5 µm. A 15 minutes long AC electro-deposition of cobalt follows. The current densities measured during catalyst deposition has been low (about 3.8 mA/cm<sup>2</sup>) with respect to the optimum value of 10 mA/cm<sup>2</sup>. The deposition was quite uniform, with a mean thickness of the metal seeds of 800 nm. Then the sample has been processed, at atmospheric pressure, in the CVD system. The furnace has been warmed up to 620 °C in flowing H<sub>2</sub>, with a controlled 100 minutes long ramp. An annealing of 3 hours in the same conditions follows. Finally, the synthesis has been carried out for 2 hours using a mixture of 10 % C<sub>2</sub>H<sub>2</sub> in N<sub>2</sub>. A post-annealing treatment, 15 hours long, in flowing nitrogen atmosphere has been performed at the same temperature.

SEM investigation reveals that the sample is covered by deposits of defective carbon structures, probably due to thermal cracking of the carbon feedstock. Only some CNTs extrude from the template pores. To characterize the CNTs, it is necessary to remove the amorphous carbon from the sample surface, so that the AAO surface results exposed at the acid solution and the template can be further etched away setting free the CNTs. This allows controlling the growth of CNTs inside the pores.

For the removal of amorphous carbon, an ion-milling treatment has been adopted. It consists of a bombardment of the sample with a beam of ions of an inert gas, usually Ar, which mechanically mills the sample. The beam can be focused on selected areas with diameters of 4 mm. In the employed ion-milling system the total beam current has been set at 0.8 mA while the pressure has been maintained at 10<sup>-4</sup> Torr. After a 4 hours long ion-milling treatment, a chemical etching in a 5 % phosphoric solution has been performed at 25 °C for 5 hours. The template turns out to be etched only where the amorphous carbon layer has been removed. SEM observations reveal a matrix of pores filled with either tubular or cylindrical carbon structures, which inherit shape and dimensions from the pores (Figure 4.15). Locally, the dissolution of the alumina template results larger, so that the 1-dimensional carbon structures are freed and collapse in bundles (Figure 4.16). The diameter of the carbon structures varies between 65 and 90 nm.

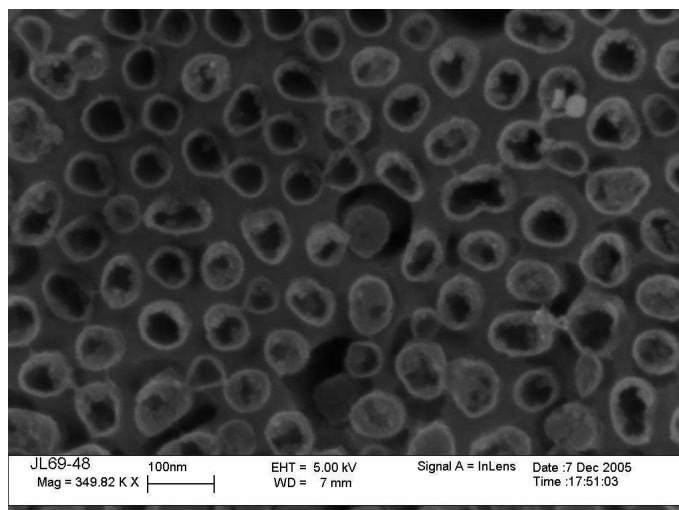


**Figure 4.15.** SEM micrographs showing the CNTs grown inside the AAO template. The CNTs have inherited shape and dimensions of the pores. Sample has been freed by the amorphous carbon coverage and the alumina has been chemically etched. Some carbon fibres are also present.

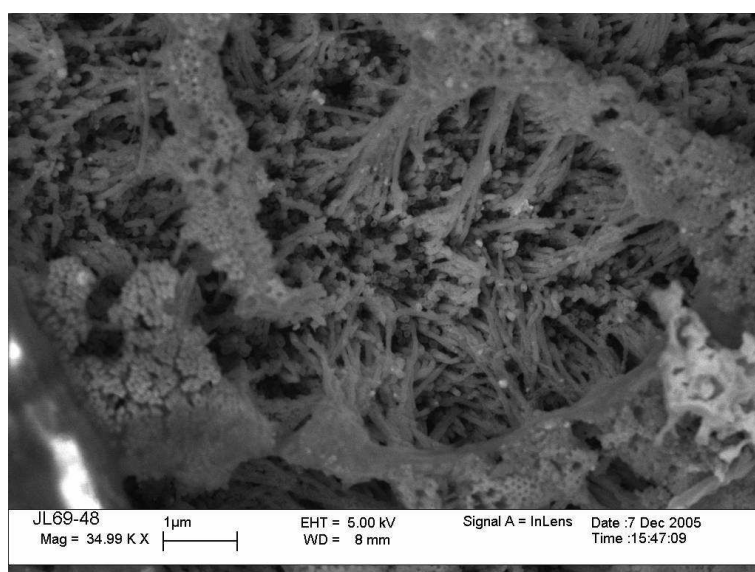


**Figure 4.16.** SEM micrographs of the same sample shown in Figure 4.15, taken in a sample area where the etching has been more effective. The enhanced dissolution of the template has freed longer section of the CNTs, which collapse in bundles.

Since the described CVD process is very time-consuming, alternative solutions have been tested in order to establish shorter growth conditions that result in less amorphous carbon deposition. The previous CVD process has been shortened, reducing the annealing step to 60 minutes and the deposition step to 20 minutes. No post annealing treatments have been performed. The process is summarized in Table 4.3. Two double-faces samples have been prepared with the “quick method”, tuning the anodization

duration in order to obtain thicknesses of 10 and 5  $\mu\text{m}$ . The AC electrochemical deposition of cobalt has been performed in conditions similar to those of the previous process, with duration of 10 minutes. A cobalt nanowires thickness of 0.5  $\mu\text{m}$  is thus expected.

| Table 4.3    |                                       |                    |                   |   |                |
|--------------|---------------------------------------|--------------------|-------------------|---|----------------|
| Process Step | Temperature<br>( $^{\circ}\text{C}$ ) | Pressure<br>(Torr) | Time<br>(minutes) | Process Gas                                       |                |
|              |                                       |                    |                   | Gas Type  | Flow<br>(sccm) |
| Intro        | RT                                    | 750                | -                 | -   | -              |
| Purge        | RT                                    | 750                | 10                | Ar  | 1000           |
| Ramp up      | RT $\rightarrow$ 620                  | 750                | 100               | H <sub>2</sub>                                    | 150            |
| Annealing    | 620                                   | 750                | 60                | H <sub>2</sub>                                    | 150            |
| Deposition   | 620                                   | 750                | 20                | 10% C <sub>2</sub> H <sub>2</sub> /N <sub>2</sub> | 17/150         |
| Cooling down | 620 $\rightarrow$ RT                  | 750                | -                 | N <sub>2</sub>                                    | 200            |

**Table 4.3.** Synoptic description of the process employed in the investigation on the synthesis of CNTs on AAO template (RT = Room Temperature).

The samples surface shows an amorphous carbon coverage like the one obtained with the long process. Two different treatments have been employed for removing this layer, namely an Ar<sup>+</sup> ion-milling and an O<sub>2</sub> plasma treatment. Differently from the former, the latter treatment allows a selective etching of the carbonaceous deposit and does not affect the AAO template.

After the ion-milling procedure, performed for 6 hours in the same conditions as before, the 10  $\mu\text{m}$  thick sample has been etched in a 5 % phosphoric solution for 2 hours at 25  $^{\circ}\text{C}$ . SEM observations show some spots, about 30  $\mu\text{m}$  in diameter, where the pores are filled by cylindrical deposits of carbon. Outside these spots, the AAO pores are empty. The effect of the chemical etching is here enhanced because of the larger surface exposed to the solution. The distribution of these spots of carbon deposit over the sample area indicates that the previous cobalt deposition was not uniform. The same morphology is found on the portion of the sample released by the amorphous carbon layer by means of a plasma treatment performed at a power of 100 W, in an O<sub>2</sub> flux of 1.8 sccm for 45 minutes. In this case, the carbon structures thickness results smaller, probably because the plasma treatment has been too aggressive.

On the 5  $\mu\text{m}$  thick sample, after the ion-milling treatment, a stronger etching of the alumina follows: the temperature has been raised up to 30  $^{\circ}\text{C}$  and the duration has been prolonged to 19 hours. As shown is the SEM images, the AAO is almost completely dissolved and pillars of collapsed carbon nanotubes appear (Figure 4.17). These structures,

whose height is approximately 5  $\mu\text{m}$ , are attached at a common basement, likely composed by the residual layer of alumina. Having lost the mechanical support of the template, on the top of the pillars the CNTs stick together by means of Van der Waals forces. Compositional analyses have been performed on the top and on the bottom of the pillars with a SEM provided with the EDX detector, which allows the identification of the atomic composition of the observed objects, but does not allow the detection of carbon. On the top, aluminium, oxygen and cobalt are not detected. On the bottom, only cobalt is found, since the residual alumina basement is too thin to be detected. Furthermore, an X-ray diffraction analysis (XRD) evidences a carbon crystalline structure, with an inter-planar distance of about 3.18  $\text{\AA}$ , to be compared with the 3.45  $\text{\AA}$  value reported for CNTs. This confirms that the tubes consisted of carbon.

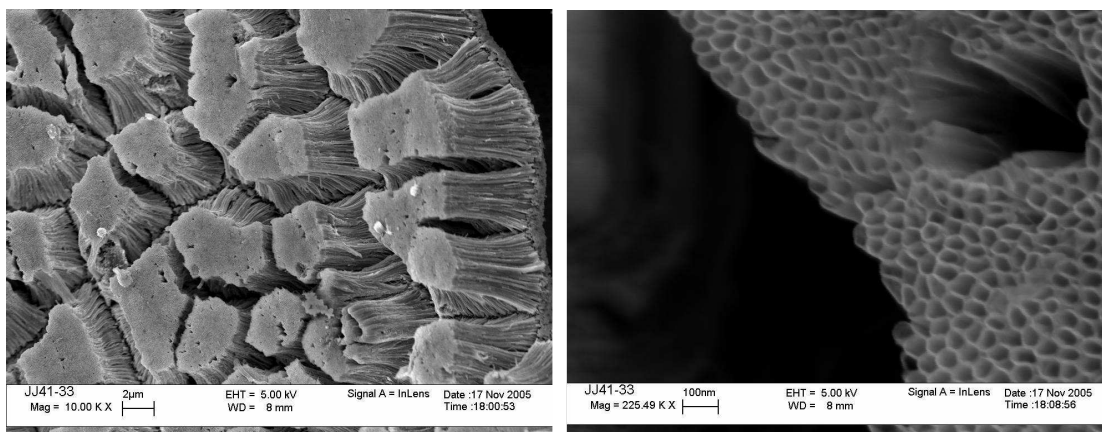


**Figure 4.17.** SEM micrographs of the CNT grown inside a 5  $\mu\text{m}$  thick AAO template with the process described in Table 4.3. On the left, carbon nanotubes collapse in pillars after the dissolution of the AAO template. On the right, a higher magnification micrograph of the top of a pillar, where the sticking of CNTs is evident.

The quality of the carbon deposits synthesized in the alumina template with the previously described methods results quite poor. Not only carbon nanotubes but also carbon nanofibres grow inside of pores. The low graphitization of carbon nanostructures grown inside an alumina template has been frequently reported in literature [52, 53, 113]. Nevertheless, they gather wide interest in different fields, also in applications, such as in the fabrication of electronics devices, where a good crystallographic quality is usually demanded [16, 106].

The low quality can be attributed to two principal reasons. Firstly, an alumina templated synthesis generally involves relatively low temperatures because of the limit imposed by the thermal stability of the template. Secondly, the alumina itself exhibits a catalytic activity [115]. Templated synthesis of CNTs has also been performed without any catalyst except the template itself [113]. Although cobalt is a much more active catalyst for

acetylene decomposition, the AAO catalytic activity can give rise to significant carbon deposit on the pore walls of the template. This process does not favour the formation of ordered structures like CNTs but mainly the deposition of graphene layer pieces on the template walls without long range scale crystalline order. If the deposition is prolonged too much or no etching gas counterbalances the carbon precipitation, these carbon planes can completely fill the pores.

Further investigations have been then developed in order to enhance the quality of the carbon deposits. Two different approaches have been adopted. On one side, synthesis temperatures higher than 620 °C have been applied for favouring a better crystallization. On the other side, the synthesis process has been modified to poison the catalytic activity of the alumina template so that the carbon decomposition and precipitation result to be driven by the metal catalyst.

Following the first approach, some alumina samples have been fabricated without the aluminium layer by means of the two-step anodization process in the anodization cell (see Table 3.1), starting from high purity (99.999 %), 100 µm thick, aluminium foils. The first anodization lasted about 1 h and an etching of the sacrificial layer has been performed at 23 °C for 30 minutes. The second anodization step has been prolonged for 15 hours in order to reach a final aluminium oxide thickness approximately of 50 µm. The subsequent DC voltage electrochemical deposition of cobalt has been performed after the evaporation on the back-side of the template of the Cr-Au counter electrode. Voltage has been set at 2.2 V in order to measure a current density of about 1 mA/cm<sup>2</sup>. The deposition lasted approximately 10 minutes, in order to deposit only some hundreds of nanometres. The CVD process has been performed following the steps indicated in Table 4.3, but at a temperature of 700 °C and with a deposition step 30 minutes long. Finally, an oxidation annealing in O<sub>2</sub> atmosphere has been performed for 1 hour at 400 °C.

The template surface does not show any amorphous carbon coverage at this stage. Few CNTs, with a cobalt cap at their tip, extrude from the template for several hundreds of nanometres. In some areas, a layer of alumina, approximately 6 – 8 µm thick, is lifted from the rest of the template, and fragmented in blocks with CNTs grown inside. CNTs have similar diameters of 100 nm, confirming that the template drives the CNT growth.

A partial dissolution of the upper layer of the template has been obtained by means of a 6 hours long chemical etching process in a 5 % phosphoric solution. The blocks described above are partially dissolved and CNTs extruding from the template can be clearly seen (Figure 4.18). In other zones the template is more deeply dissolved, releasing further on some CNTs. As can be seen in the SEM micrograph of Figure 4.19, these CNTs lie on a porous layer, composed by a dense population of CNTs having smaller diameters with respect to the previous ones (between 60 and 80 nm). Because the template support is missing, these smaller CNTs collapse one on the other, remaining stuck under the effects of Van der Waals forces, and some cracks appear on the surface.

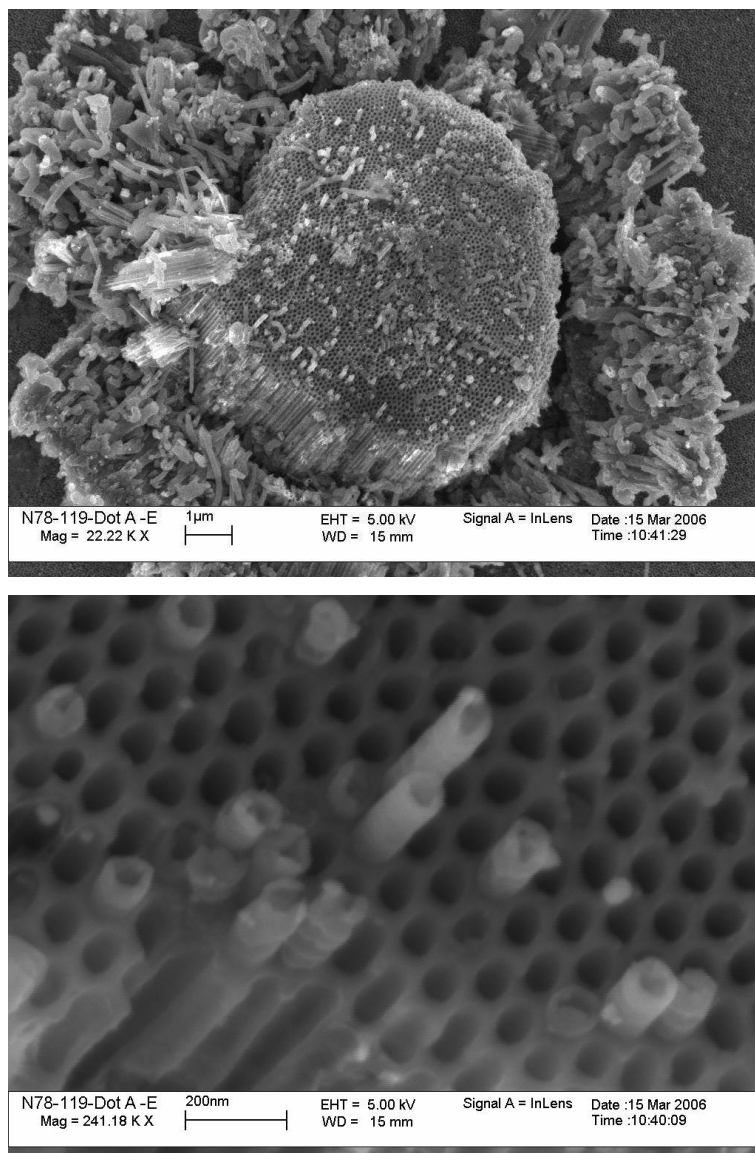


**Figure 4.18.** SEM micrographs of CNTs grown inside the AAO template in the process at 700 °C. The alumina has been produced by the two-step anodization. Above, an alumina block which is lifted from the rest of the template is shown. Below, a higher magnification image shows some CNTs, with diameter of 100 nm, extruding from the alumina template pore.

The two different populations of CNTs on the sample and the presence of detached layers of AAO indicate that two different layers of alumina have been produced by the two-step anodization process. The AAO template produced during the first anodization has not been completely removed by the first chemical etching. The second anodization reduces the thickness of the sacrificial layer of alumina, but does not dissolve it completely, resulting in a further enlarging of the template pores. The subsequent CVD process results in a growth of CNTs with two different mean diameters. The short carbon structures with the Co nanoparticle cap grow from Co clusters deposited at the step between the two alumina layers and not at the pore bottom.

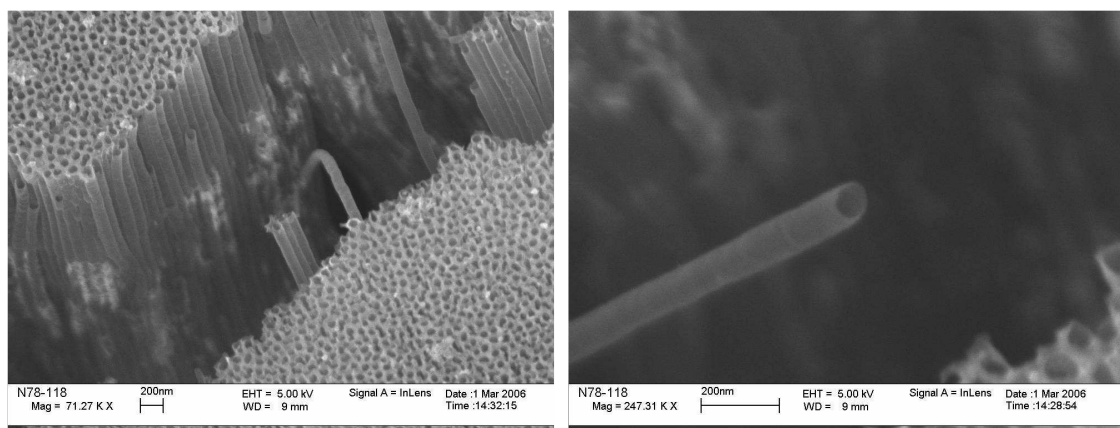


**Figure 4.19.** SEM micrographs of the CNTs grown at 700 °C in the AAO template. The CNTs have been freed and collapse one on the other after the dissolution of the alumina template. With respect to the CNTs shown in Figure 4.18, these CNTs have smaller diameters (60 – 80 nm). This indicates that different CNTs are grown in a template with different features.

A new sample has been prepared raising the temperature of the dissolution process between the two anodizations from 23 °C to 30 °C. This increase corresponds approximately to an enhancement of the reaction speed by a factor two. The duration of the first anodization and of the sacrificial layer removal steps have been doubled, in order to further enhance the template regularity. The other fabrication steps remain unchanged. The DC electrochemical deposition of cobalt has been performed imposing the same voltage of the previous process, but the measured current density results lower, namely 0.15 mA/cm<sup>2</sup>. The same process conditions applied for the previous samples have been adopted both for the CNTs synthesis and the oxidation annealing at 400 °C.

The resulting sample has a clean surface. Only few 1-D carbon structures, a few hundreds of nanometres long, are found on the surface. Few cobalt nanowires are found inside the pores, as expected from the low current density measured during the electro-deposition of cobalt. The chemical etching in phosphoric solution has been performed. However, a carbon layer has covered the entire alumina surface, shielding the oxide from the solution. Only locally, where some defects in the coverage occur and the shield is partially removed, some alumina is dissolved. This dissolution proceeds slowly as the CNTs grown in the pores shielded themselves the inner walls of the template, so that only the surface between the pores results exposed. The CNTs partially freed by the template can be observed by SEM (Figure 4.20).

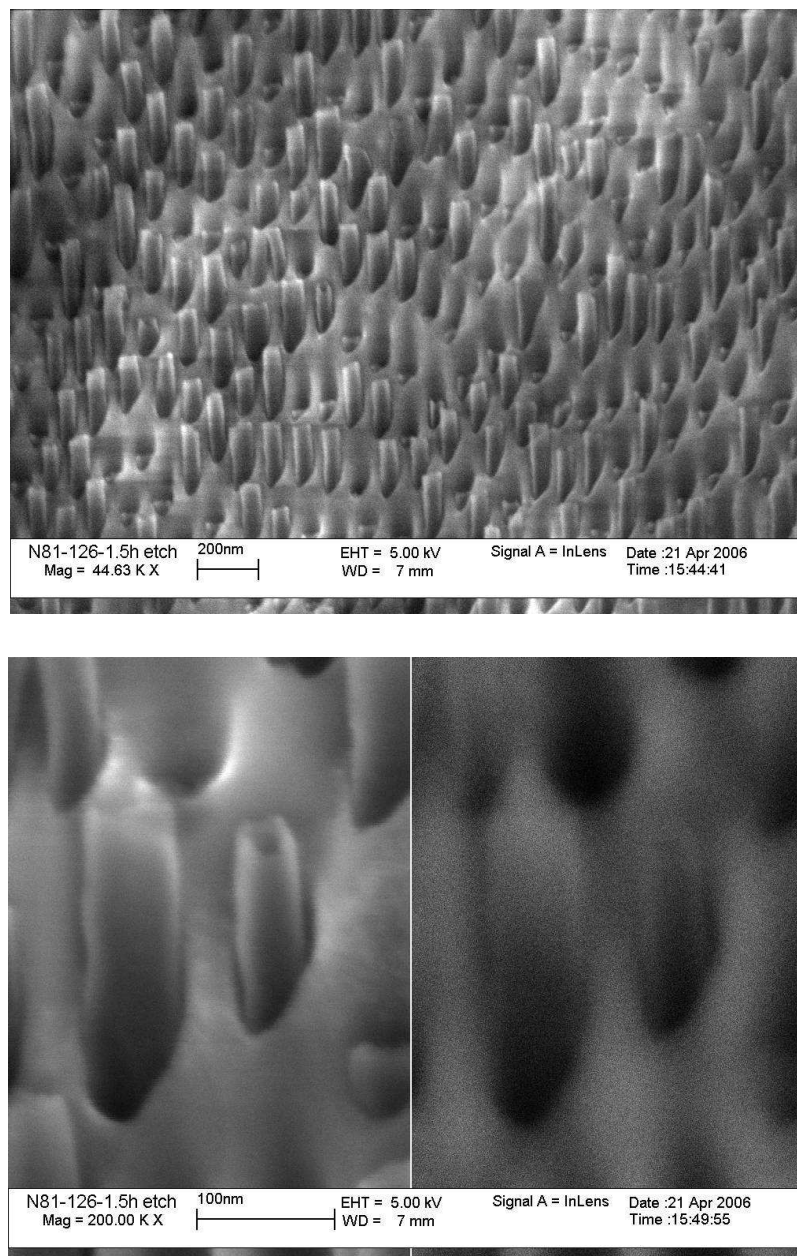


**Figure 4.20.** SEM micrographs of the CNTs grown at 700 °C inside the AAO template fabricated by means of the two-step anodization process, without the formation of the two different AAO layers. Above, the dissolution of the template partially frees CNTs. Below, a higher magnification of the same sample area shows clearly the filling of the AAO pores with CNTs.

To fasten the elimination of the template, a further oxidation process at a higher temperature (420 °C) and a prolonged duration (2 hours) has been performed. A prolonged etching step of 21 hours has been needed to remove almost completely the AAO template. The SEM investigation demonstrates that the alumina dissolution proceeds from the bottom of the template and not from the upper surface. The Au – Cr back layer has been

removed by the prolonged etching process, whereas the carbon coverage that has shielded the upper surface has been not removed yet by the oxidation process. In some areas of the top of the sample the CNTs are still entrapped in residual template. Moving downwards to the bottom, the carbon structures start to be released (Figure 4.21) and at the bottom they stick together.

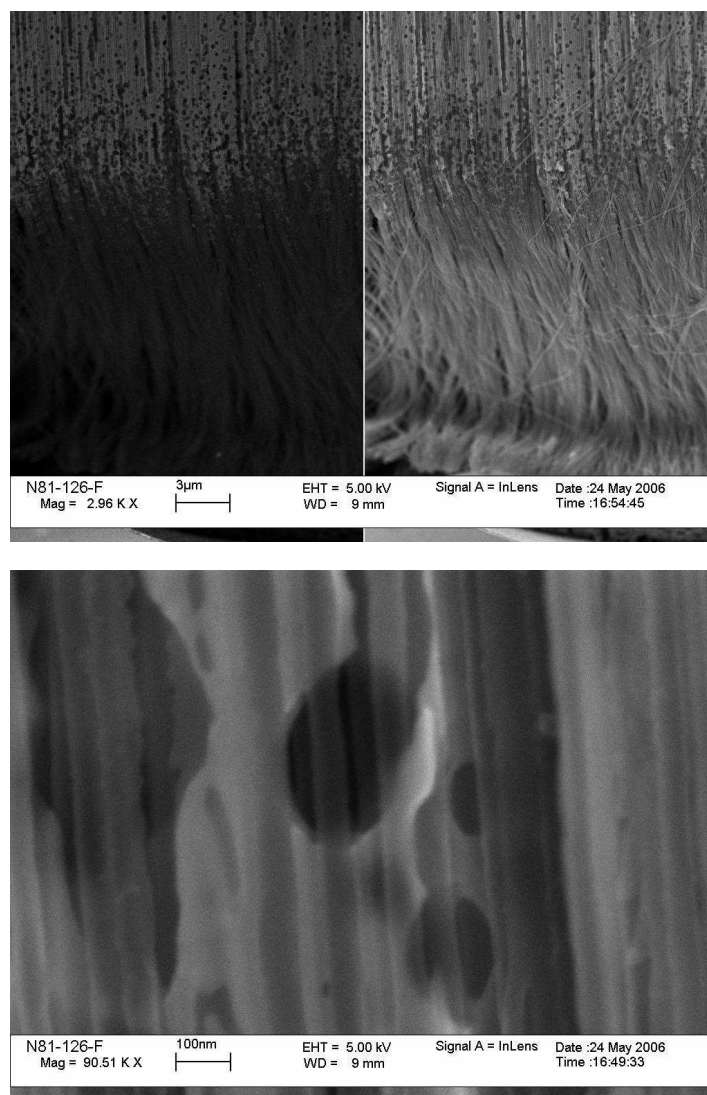
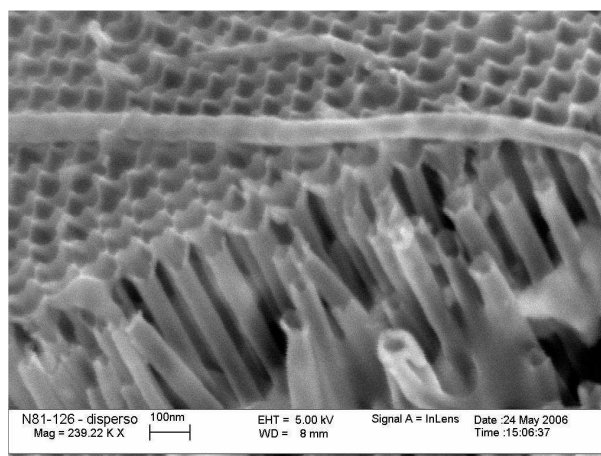


**Figure 4.21.** Prolonging the etching treatment, the alumina template is dissolved from the bottom of the sample, namely from the Cr/Au side. Above, SEM micrographs of the boundary of the etched template. A comparison of the back-scattered electrons (on the left) and the InLens images (on the right) is reported. The brighter area on the left image indicates the higher-Z alumina, whereas the darker area is composed by low-Z carbon structure. The sticking of the CNTs at the base, where the dissolution of the alumina is accomplished, is also observed. Below, a higher magnification of the same area shows CNTs partially freed by the alumina template.

It is worth noting that CNTs have diameters narrowly spread around the mean value of 60 nm. CNT diameters enlarge at the top so that they result linked together in blocks (Figure 4.22). This observation and the fact that all the CNTs have grown inside the template to almost the same height clearly indicate that the synthesis has been mainly driven by the catalytic activity of the template.

**Figure 4.22.** Locally, the dissolution of the alumina template has been completed and the CNTs have been freed up to their tip. In this area, CNTs diameter widens and result linked together. This connection has shielded the alumina template preventing the etching from the upper surface of the sample.



To further investigate the quality of the CNTs, Raman and TEM analyses have been performed. A Raman investigation on the CNTs embedded in the alumina template shows the D and G peaks but an additional background signal arises from the vibrations of the alumina. Another Raman spectrum has been collected on a sample consisting of CNTs completely released by the template (Figure 4.23). It shows a D peak with high intensity, indicating that the crystalline structure of the carbon walls is still defective. In fact, the  $I_D/I_G$  ratio, i.e. the ratio between the intensities of the defective and of the graphite peak, turns out to be approximately 1.4. Also the ratios  $I_D/I_{G'}$  and  $I_G/I_{G'}$  between the second resonant peak of graphite,  $I_{G'}$ , and respectively the defective,  $I_D$ , and the first resonant order peak of graphite,  $I_G$ , are high.

The crystallinity of the CNT walls has been observed by means of TEM. The preparation of the sample for the observation involves a dispersion of the CNTs in a solution that is then spilt over a thin grid support. The graphitization of the CNTs walls is quite poor, since it does not extend over a long scale range. The walls are indeed formed by a sequence of graphene sections, randomly arranged. These graphitic segments produce the diffraction patterns which, although the signal is low, are compatible with the reflection of the graphenic planes, having an inter-plane distance of 3.4 Å.

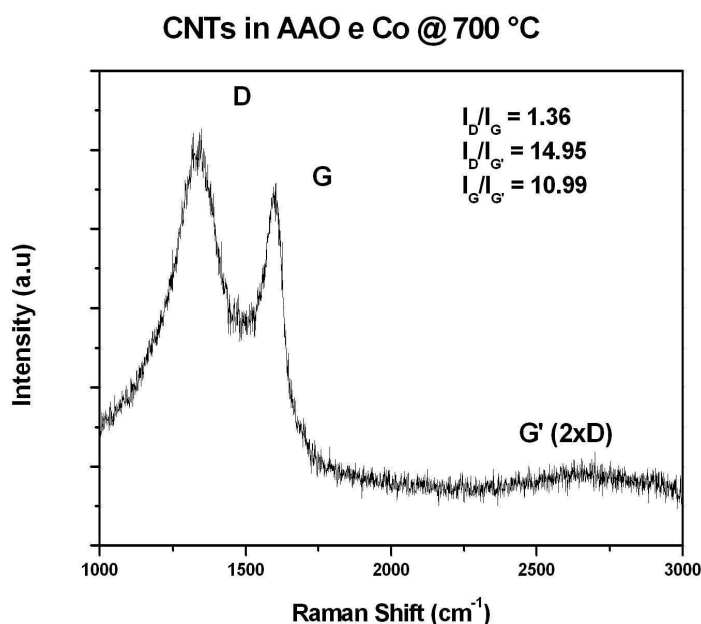


**Figure 4.23.** Raman spectrum of the CNTs grown at 700 °C inside the AAO, already shown in the previous figures, taken after the complete dissolution of the template. The ratios of the D, G and G' peaks are also reported.

The CNTs synthesized inside the AAO template have a low graphitization quality, but still comparable with those reported in the literature [113, 116]. This poor graphitization has been still related to the catalytic activity of the AAO. Not driven by a metal nanoparticle, carbon precipitates in short-range ordered structure directly on the template walls, without achieving good crystallinity over a long-range scale. Nevertheless, this template approach can be useful in synthesizing carbon tubules with the same dimensions, i.e. diameter and length. Different post-annealing treatments have been proposed in literature in order to enhance the graphitization of carbon structures deposited in similar conditions [117, 118]. High temperatures (above 1400 °C) annealing in inert atmosphere have been proven to give good results. The necessity of preserving the aluminium template in the detector proposed in the NanoChanT project, will force us under these temperatures and so different approaches will have to be defined.

The second approach followed for enhancing the CNT quality has been aimed at modify the CVD process in order to inhibit the catalytic sites of the aluminium oxide, reducing the hydrocarbon cracking. By this way, the CNT growth would only be driven by the catalytic activity of the metal seeds inside the pores. It is thus equally important to search the proper process conditions in order to maximize the catalytic activity of the metal. The optimum balance between these two requirements will have to be found.

Firstly, the most favourable conditions to inhibit the catalytic activity of the AAO have been studied. CVD processes have been performed on AAO samples without cobalt catalyst in its pores. The process described in Table 4.3 has been modified by using a 30 minutes long deposition and employing different gases. The same gas has been used in the entire process, with a mixture of 5 % C<sub>2</sub>H<sub>2</sub> in carrier gas during the deposition step. Argon, ammonia and hydrogen have been studied. A sample of alumina, 10 μm thick, has been anodized on both faces by means of the single step process and then divided to undergo the different processes.

After the CVD process, the colour of the three samples turns out to be significantly different. When Ar or H<sub>2</sub> are used, the samples result completely black, whereas the NH<sub>3</sub> processed AAO is only slightly coloured. SEM investigations confirm that the difference is related with the amount of carbon deposited over the template surface. In the former cases the catalytic activity of the alumina is not inhibited at all and the dissociated hydrocarbon precipitates homogeneously on the surface. On the other hand, only a small amount of carbon layers is deposited on the alumina surface when NH<sub>3</sub> is employed. At low temperatures, around 100 °C, ammonia saturates the acid centres of the AAO surface that are the active catalytic sites for the dissociation of the hydrocarbon. The effects of the annealing in NH<sub>3</sub> atmosphere at higher temperatures have not been established so far. The bonding between the basic groups of NH<sub>3</sub> and the acid groups of the alumina is reversible so it is expected that at higher temperatures this poisoning will be more difficult since the bond could be broken. The dynamic equilibrium between the adsorption and the desorption of NH<sub>3</sub> at the process temperature will establish whether the annealing process in NH<sub>3</sub> can be useful or not in preventing the deposits of not well ordered carbon layers on the alumina surface. Our results demonstrate that it is possible to inhibit these acid centres also at 620 °C.

The effect of H<sub>2</sub> and NH<sub>3</sub> on AAO samples have been investigated also in the presence of cobalt catalyst. The process described in Table 4.3 has been modified using a 10 % and 5 % mixture of C<sub>2</sub>H<sub>2</sub> in H<sub>2</sub> and NH<sub>3</sub>, respectively.

An alumina template, 18 μm thick, has been produced in the anodization cell by means of the single-step process (see Table 3.1), performed at a temperature of 27 °C to fasten the process. Voltage decreasing and pore widening have also been performed for the removal of the barrier layer and the DC cobalt deposition (at 2.5 V in order to achieve a current density of 1.2 mA/cm<sup>2</sup>). To have some insights on the distribution of the cobalt inside the pores, a piece of the alumina sample has been almost completely dissolved by means of a phosphoric etching (at 25 °C, 3 hours long). Some cobalt pillars, 10 μm thick, are observed by SEM. The sample was divided in two pieces that underwent the two different CVD processes.

Both the processed samples exhibit a surface almost completely free from carbon deposits. This indicates that the amount of carbon deposited over the template surface has been limited by using both H<sub>2</sub> and NH<sub>3</sub> as carrier gases. In the presence of the cobalt

catalyst, the reaction involved in the synthesis change and also with H<sub>2</sub> the deposit of amorphous carbon is hampered. The chemical etch for alumina dissolution has been thus directly performed without any treatments for the removal of carbon. Many pillars made up of cylindrical structures are found on both the samples. The morphology is quite similar to the Co deposit, but these structures are composed by alternated carbon and cobalt segments. In the H<sub>2</sub> processed sample the pillars are about 15 μm thick, whereas in the NH<sub>3</sub> processed one the thickness grows up to 20 μm. Raman investigations do not reveal significant differences between the two samples. Their Raman spectra evidence a high D peak and the absence of the second resonant peak of graphite, I<sub>G</sub>, indicating the crystallographic quality of the carbon structures is still defective. Nevertheless, in this processes the CNTs have grown only catalyzed by the cobalt and not by the template. Even if further investigations are necessary for optimize the deposition step, some indications about the possibility of poisoning the template have been achieved. These can address the research towards a CNTs synthesis in AAO template which yields higher quality with respect to those commonly achieved.

## Conclusions

The work described in this thesis is part of the NanoChanT project, whose goal is the fabrication of a novel radiation detector with submicron spatial resolution.

The design of the detector is based on some innovative nanotechnologies that have to be finalized to the specific demands of the device. A highly regular insulating nanoporous template of Anodic Aluminium Oxide (AAO) is fabricated, with nanochannels uniformly filled by conductive Carbon Nanotubes (CNTs). This array of nanoconductors is coupled with a thin silicon layer that works as the sensing element of the detector.

The synthesis of CNTs performed by means of the Catalyst-assisted Chemical Vapour Deposition (C-CVD) method has been studied. The growth process has been investigated in two configurations, namely a free-standing growth and a confined growth.

The former configuration has been used in order to optimize the deposition process and to define the proper interface between CNTs and the silicon substrate. The growth process parameters (such as temperature, annealing and carrier gases and fraction of carbon feedstock gas in the deposition mixture) are critical in determining the structural and electrical properties of the CNTs. Moreover, also the formation of the catalyst nanoparticles, which act as seeds for the CNT growth, strongly affects the features of the resulting CNTs.

The work performed during this thesis has been particularly devoted to the optimization of the C-CVD process, in order to synthesize CNTs, both in the free standing and confined configuration, with the most proper features for the different applications, and to their structural and electrical characterization by means of scanning electron microscopy investigations and field emission measurements.

Free standing, vertically aligned multi-walls CNTs of good crystallographic quality, with length varying between 4 and 20  $\mu\text{m}$  and diameter between 20 and 100 nm, have been successfully grown on silicon, both directly and by using intermediate coupling layers, such as silicon dioxide, silicon nitride and titanium nitride. In particular, the formation of the catalyst nanoparticles, prior to the synthesis process, has been investigated on the silicon dioxide and silicon nitride layers. Nanoparticles annealing treatment in ammonia atmosphere is found to be fundamental in order to effectively catalyze the CNT growth. Also layers of titanium nitride, with different deposition techniques and appropriate features for the CNT growth, have been investigated.

The conductivity of different coupling layers has been studied by means of a field emission characterization of the grown CNTs. The best solution is found to be a titanium nitride layer deposited by magnetron sputtering technique on a heated silicon substrate. In particular, the CNTs, grown at low pressure on this conductive titanium nitride, exhibit remarkable field emission properties. For the proper handling of the experimental data, a model of the measurement method has been proposed in this thesis. The model defines how to calculate the effective emitting area when a sphere-to-plane configuration is used for the electrodes. Under the application of an electric field of 4 V/ $\mu\text{m}$ , CNTs on conductive titanium nitride reach current densities of several mA/cm<sup>2</sup>.

Finally, CNTs growth has been finally investigated in a confined configuration, by using the AAO matrix as a template. The investigation on the different process parameters allows to optimize the CNTs growth also for this arrangement and to obtain high uniformity, both in length and in diameters, inside the pores of the AAO template. Carbon nanotubes lengths up to 50  $\mu\text{m}$  have been reached, with diameter of 60 nm.

To conclude, the experimental results obtained in this thesis have allowed to achieve some of the technological steps fundamental to the NanoChanT project. Moreover, some of these outcomes encourage new applications of the investigated nanostructures. For instance, CNTs confined within the AAO nano-channels could be used for the fabrication of a cold cathode emitter device, as cold electron sources for many possible applications.

Part of this thesis results, on the growth of CNTs, have been recently accepted for publication on journal (G. P. Veronese et al., *Physica E*, *in press, corrected proof*, available on-line 16 October 2006).





## Bibliography

- [1] S.M. Sze, *Semiconductor Devices: Physics and Technology*. New York. Edited by John Wiley and Sons, 1985.
- [2] H. Bichsel, *Nucl. Instr. Meth. Phys. Res. A* 562 (2006) 154.
- [3] W.R. Leo, *Techniques for Nuclear and Particle Physics Experiments*. Edited by Springer-Verlag, 1987.
- [4] H. Bichsel, *Rev. Mod. Phys.* 60 (1988) 663.
- [5] C.J.S. Damerell, *Vertex Detectors: The state of the art and future prospects*, Edited by C.J.S. Damerell, Rutherford Appleton Laboratory, 1995.
- [6] C.J.S. Damerell, *Rev. Sci. Instr.* 69 (1998) 1549.
- [7] CMS Tracker Technical Design Report 5 1998.
- [8] ATLAS Inner Detector Technical Design Report v.1 and 2, CERN/LHCC 97-16 and 97-17, 1997.
- [9] B. Aubert, *Nucl. Instr. Meth. Phys. Res. A* 479 (2002) 1.
- [10] W.J. Burges, *Nucl. Phys. B* 113 (2002) 139.
- [11] A. Bergamaschi, *Nucl. Instr. Meth. Phys. Res. A* 549 (2005) 199.
- [12] R. Angelucci, *Nucl. Phys. B. (Proc. Suppl.)* 150 (2006), 140.
- [13] V. Derycke, *Nano Letters*. 1 (2001) 453.
- [14] B.C. Satishkumar, *J. Mater. Chem.* 10 (2000) 339.
- [15] Y.M. Choi, *Nano Letters* 3 (2003) 839.
- [16] W.B. Choi, *Appl. Phys. Lett.* 79 (2001) 3696.
- [17] G. De Geromino, *Nucl. Instr. Meth. Phys. Res. A* 471 (2001) 192.
- [18] C. Kapnitis, *Nucl. Instr. Meth. Phys. Res. A* 458 (2001) 729.
- [19] P. O'Connor, *Nucl. Instr. Meth. Phys. Res. A* 480 (2002) 713.
- [20] G. Lutz, *Semiconductor Radiation Detectors*. Edited by Springer-Verlag Berlin, Heidelberg 1999.
- [21] Y. Xia, *Adv. Mater.* 15 (2003) 353.
- [22] Y. Li, *Mater. Today* 9 (2006) 18.
- [23] A. Oberlin, *J. Crys. Growth* 32 (1976) 335.

- [24] S. Iijima, *Nature* 254 (1991) 96.
- [25] M.S. Dresselhaus, G. Dresselhaus, Ph. Avouris (Eds.), *Carbon Nanotubes. Synthesis, Structure, Properties and Applications*, Springer-Verlag. Berlin 2001.
- [26] *Materials Today* 10 (2004).
- [27] M. Terrones, *Annu. Rev. Mater. Res.* 33 (2003) 419.
- [28] J. Robertson, *Mater. Today* 7 (2004) 46.
- [29] H. Dai, *Surf. Sci.* 500 (2002) 218.
- [30] H. Dai, *Acc. Chem. Res.* 35 (2002), 1035.
- [31] S. Frank, *Science* 280 (1998), 1744.
- [32] H. Soh, *Appl. Phys. Lett.* 75 (1999), 627.
- [33] A. P. Graham, *Diam. Rel. Mater.* 13 (2004) 1296.
- [34] M. Bockrath, *Phys. Rev. B* 61 (2000) R10606.
- [35] P. Avouris, *Acc. Chem. Res.* 35 (2002) 1026.
- [36] A.C. Dupuis, *Prog. in Mater. Sci.* 50 (2005) 929.
- [37] E.F. Kukovitsky, *Appl. Surf. Sci.* 215 (2000) 201.
- [38] Y. Li, *J. Phys. Chem. B.* 105 (2001) 11424.
- [39] C.J. Lee, *Chem. Phys. Lett.* 341 (2001) 245.
- [40] S. Fan, *Science* 283 (1999) 512.
- [41] R.S. Wagner, *Appl. Phys. Lett.* 4 (1964) 89.
- [42] R.T.K. Baker, *J. Catal.* 26 (1972) 51.
- [43] C. Ducati, *J. Appl. Phys.* 95 (2004) 6387.
- [44] Y. Homma, *J. Phys. Chem B.* 107 (2003) 12161.
- [45] S. Hofmann, *Phys. Rev. Lett.* 95 (2005), 036101.
- [46] S. Helveg, *Nature* 427 (2004) 426.
- [47] Y. Ando, *Mater. Today* 7 (2004), 22.
- [48] N. Nagaraju, *J. Mol. Catal. A* 181 (2002) 57.
- [49] C.J. Lee, *Chem. Phys. Lett.* 360 (2002) 250.
- [50] M. Chhowalla, *J. Appl. Phys.* 90 (2001) 5308.
- [51] M. Cantoro, *Diam. Rel. Mater.* 15 (2006) 1029.
- [52] J. Li, *Appl. Phys. Lett.* 75 (1999), 367.
- [53] D.N. Davydov, *J. Appl. Phys.* 86 (1999), 3983.
- [54] W.B. Choi, *Appl. Phys. Lett.* 75 (1999) 3129.
- [55] Y. Saito, *Jpn. J. Appl. Phys.* 39 (2000) L271.
- [56] Y. Saito, *Carbon* 38 (2000) 169.
- [57] G. Yue, *Appl. Phys. Lett.* 81 (2002) 355.
- [58] N. de Jonge, *Phil. Trans. R. Soc. Lond. A* 362 (2004) 2239.
- [59] J.M. Bonard, *Adv. Mater.* 13 (2001), 184.
- [60] R.H. Fowler, *Proc. R. Soc. Lond. A* 119 (1928) 173.
- [61] J.M. Bonard, *Phys. Rev. Lett.* 89 (2002) 197602.
- [62] L. Nilsson, *Appl. Phys. Lett.* 76 (2000) 2071.
- [63] J.M. Bonard, *Solid-State Electr.* 45 (2001) 893.

- 
- [64] J.M. Bonard, *Ultramicroscopy* 73 (1998) 9.
- [65] K.A. Dean, *J. Appl. Phys.* 85 (1999) 3832.
- [66] S.T. Purcell, *Phys. Rev. Lett.* 89 (2002) 276103.
- [67] V.V. Zhirnov, *J. Vac. Sci. Technol. B* 19 (2001) 87.
- [68] J.M. Bonard, *Phys. Rev. B* 67 (2003) 115406.
- [69] O. Groening, *J. Vac. Sci. Technol. B* 18 (1996) 665.
- [70] C.A. Huber, *Science* 263 (1994), 800.
- [71] R. L. Fleisher, *Nuclear Tracks in Solids*, University of California Press, Berkeley, CA 1975.
- [72] F. Keller, *J. Electrochem. Soc.* 100 (1953) 411.
- [73] O. Jessensky, *Appl. Phys. Lett.* 72 (1998) 1173.
- [74] V. P. Parkhutik, *J. Phys. D. Appl. Phys.* 25 (1992) 1258.
- [75] J.P. O'Sullivan, *Proc. Roy. Soc. Lond. A* 317 (1970) 511.
- [76] O. Jessensky, *J. Electrochem. Soc.* 145 (1998) 3735.
- [77] K. Shimizu, *Phil. Mag. A* 66 (1992) 643.
- [78] G.E. Thompson *Nature* 290 (1981) 230.
- [79] A.P. Li, *J. Appl. Phys.* 84 (1998) 6023.
- [80] H. Masuda, *Science* 268 (1995) 146.
- [81] H. Masuda, *J. Electrochem. Soc.* 144 (1997) L127.
- [82] H. Masuda, *J. Jpn. Appl. Phys.* 37 (1998) L1340.
- [83] H. Masuda, *Appl. Phys. Lett.* 71 (1997), 2770.
- [84] H. Masuda, *Jpn. J. Appl. Phys.* 35 (1996), L126.
- [85] E. Herrmann, *Galvanotechnik* 63 (1972), 110.
- [86] A. Jagminas, *Appl. Surf. Sci.* 201 (2002) 129.
- [87] D.J. Sellmeyer, *Jou. Phys. Condensed Matter* 13 (2001) R433.
- [88] A. Saedi, *Mater. Chem. Phys* 91 (2005), 417.
- [89] A. Jagminas, *Jou. Appl. ElectroChem.* 32 (2002), 1201.
- [90] J. Gruberger, *Electrochim. Acta* 31 (1986), 1531.
- [91] H. Bethge, *Electron Microscopy in Solid State Physics*, Elsevier, Amsterdam, Oxford, New York, 1987.
- [92] A.M. Keszler, *J. Optoelectr. and Adv. Mater.* 6, (2004), 1269.
- [93] J. I. Sohn, *Appl. Surf. Sci.* 197-198 (2002), 568.
- [94] G.S. Choi, *J. Appl. Phys.* 91 (2002) 3847.
- [95] M. Jung, *Diam. Rel. Mater.* 10 (2001) 1235.
- [96] K.K. Al-Shammeri, *J. Phys. Chem* 90 (1986) 2906.
- [97] J. Maultzsch, *Appl. Phys. Lett.* 81 (2002) 2647.
- [98] T. De los Arcos, *Appl. Phys. Lett.* 80 (2002) 2383.
- [99] G. Pirio *Nanotechnology* 13 (2002) 1.
- [100] J.E. Sundgren, *Thin Solid Films* 128 (1985), 21.
- [101] J. Geng, *J. Appl. Phys.* 86 (1999) 3460.

## Bibliography

---

- [102] M. Abramowitz, *Handbook of Mathematical functions*. Dover Publications, Inc. New York, 1968.
- [103] A.N. Obraztov, *JETP Lett* 69 (1999) 411.
- [104] I. Boscolo, *Accepted to be published in J. Vac. Sci. Technol. B*.
- [105] *Numerical Recipes in C: The art of scientific computing*. Cambridge University Press 1992, pg 683.
- [106] S-K. Hwang, *Nanotechnology* 16 (2005) 850.
- [107] M. Mikhaylova, *Mat. Res. Soc. Symp. Proc.* 704 (2002), W6.34.1 – W6.34.6.
- [108] Y. Yang, *Sol. State Comm.* 123 (2002), 279.
- [109] A. Jagminas, *Appl. Surf. Scie.* 252 (2006), 2360.
- [110] A. Jankowski, *Thin Solid Films* 491 (2005), 61.
- [111] R. Gras, *Microelectr. Eng.* 83 (2006), 2432
- [112] T. Iwasaki, *Appl. Phys. Lett.* 75 (1999) 2044
- [113] T. Kyotani, *Bull. Chem. Soc. Jpn.* 72 (1999) 1957.
- [114] J.M. Xu, *Infra. Phys. Tech.* 42 (2001) 485.
- [115] A. Thess, *Science* 273 (1996) 483.
- [116] H. Gao, *J. Appl. Phys.* 93 (2003) 5602
- [117] L. Ci, *J. Crys. Growth* 233 (2001) 823.
- [118] H. Yokomichi, *Vacuum*, 74 (2004), 677.